AMIGA muon counters and shower universality reconstruction

Zur Erlangung des akademischen Grades eines
DOKTORS DER NATURWISSENSCHAFTEN
von der KIT-Fakultät für Physik des

Karlsruher Instituts für Technologie (KIT)
und der
Universidad Nacional de San Martín (UNSAM)

genehmigte
DISSERTATION

von

Lic. Mariela Josebachuili
aus Buenos Aires

Tag der mündlichen Prüfung: 2 Februar 2018

Referent: Prof. Dr. A. Etchegoyen, Instituto de Tecnologías en Detección y Astropartículas, CNEA - CONICET - UNSAM
Koreferent: Prof. Dr. J. Blümer, Bereich V, Karlsruher Institut für Technologie
Betreuer: Dr. D. Melo, Instituto de Tecnologías en Detección y Astropartículas, CNEA - CONICET - UNSAM
Betreuer: Dr. M. A. Roth, Institut für Kernphysik, Karlsruher Institut für Technologie

Dedicated to the honor of my beloved grandma Pilar . . .

Acknowledgements

Firstly, I would like to express my sincere gratitude to my advisors Prof. Alberto Etchegoyen and Prof. Johannes Bluemer for the continuous support of my Ph.D research and studies, for their motivation, stimulating discussions and patient to finally complete this important stage in my life. The guidance and advice helped me during all the research time and writing of this thesis. You both really encourage me to finish my PhD with a complete and diverse knowledge and I am very grateful because of that.

My sincere thanks also goes to Dr. Diego Melo and Dr. Markus Roth, who provided me an opportunity to join their team, you both work a lot with me and I learned a lot from you both, not only about science but also about organizing and show my research. Without they precious support it would not be possible to conduct this research.

I thank my labmates and colleges (from Argentina, Germany, Italy, Spain, France, States...) for the stimulating discussions, for the sleepless nights and weekends we were working together before deadlines, and for all the fun we have had in the last years. You all teach me how to work as a team, to improve my communication in different languages, to understand different cultures. I am really happy to have the opportunity of doing my research close to you all.

Last but not the least, I would like to thank my family and my friends for supporting me spiritually throughout the developing of this research and writing this thesis and my life in general. Do a PhD is not an easy task, and you need your loved ones as close as possible to achieve it.

Abstract

Cosmic rays impact the earth atmosphere as a continuous flux with an energy spectrum over a wide energy range. Their flux decreases with increasing energy following a power law. High energy cosmic rays are of relevance since they can help us improving our knowledge about the universe.

The main high-energy features of the spectrum are the knee, second-knee, ankle, and spectrum suppression, each of which arises from a particular scientific reason to be unraveled and which are all linked to the primary CR mass. Therefore, Pierre Auger Observatory is upgrading its detection system to include the second-knee region and to improve the mass identification up to the highest energies. In particular one of these upgrades is called AMIGA ("*Auger Muons and Infill for the Ground Array*") which is the main detector system to be addressed in this thesis work.

AMIGA is based on a direct measurement of the muonic content (N_μ) and of X^{μ}_{max} via detailed muon arriving times. Their goals are to measure composition/hadronic models related observables in conjunction with other Auger detectors at LHC energies and above, studying the transition from galactic to extra-galactic cosmic-ray sources. These objectives encompass the general Auger objectives and also enrich cosmic-ray research allowing the whole spectrum region from the second-knee onwards to be studied with a single and unique Observatory.

Several efforts were done to get a detector with the high resolution in measuring the muonic component as AMIGA. Two different works were developed during this thesis work. The first one is related to the detector opto-electronics system upgrade and the second one related to including the direct measurement of the muonic component of the cosmic ray shower in the universality reconstruction.

After the conclusion of this work a full operating and calibrated new opto-electronics system was installed in 8 modules of AMIGA in the Pierre Auger Observatory site. The upgrade of the detector consist of SiPM detection system. The main motivations for this upgrade are the advantages these devices have

compared to current MaPMTs: lower cost per channel, longer life-time, better sturdiness, lower high-voltage, higher photon detection efficiency at the optical fiber emission wavelength, no optical cross-talk between channels, and negligible after pulses. The main disadvantages of SiPMs are its higher noise rate and temperature dependence. This higher noise was employed as an advantage to set the calibration method, and the high PDE helped modifying the discrimination level of the detector signal to higher values to avoid accidental counting. The counting strategy proposed is therefore based on an amplitude criteria. As a result of the calibration developed in this work, a high detector efficiency, i.e. 98 % efficiency for the highest tested overvoltage, combined with a low probability of accidental counting ($\sim 2\%$), was achieved.

Also a new model was developed to include AMIGA detector signals in the signal model of the universality reconstruction. Universality method propose a novel technique based on the universal shape that can describe the particle shower produced by a cosmic ray primary particle. Direct muon-content of the shower measurements, by including the AMIGA signals in universality reconstruction procedure, will significantly reduce systematic uncertainties on the cosmic ray main parameters (E, X_{max}, and R_{μ}). Therefore knowledge of these three parameters from a hybrid detection followed by reconstruction within the universality model will permit to pursue a significantly better identification of both hadronic model and primary particle mass composition. On this identification lies the proposed scientific goals of the Pierre Auger Project. The strength of the proposed universality MD model is that it does not depend on neither the shower primary particle nor on the hadronic model. During this work, the signal model for the muon detectors of AMIGA is described and then tested with different hadronic models and primaries, showing and accurate prediction of the parameters (less than 10% bias in both R_{μ} and E). Furthermore, a high energy real event was reconstructed with the standard reconstruction procedure and then compared to the results obtained with universality. The results in energy and mass composition obtained with the universality reconstruction are compatible to the results obtained with the FD detector for this event.

Resumen

Los rayos cósmicos impactan la atmósfera terrestre con un flujo constante que cubre varios órdenes de magnitud en energía. Su flujo decrece con el aumento de la energía de la partícula primaria siguiendo una ley de potencia. Los rayos cósmicos de las más altas energías son de especial interés pues nos permiten incrementar el conocimiento que tenemos del universo.

Las características principales del espectro de energía son la rodilla, la segunda rodilla, el tobillo y la supresión del espectro, todas ellas relevantes desde el punto de vista científico y todas ellas también relacionadas con la composición de masa de la partícula primaria. Consecuentemente, el Observatorio Pierre Auger está actualizando su sistema de detección para poder extender su espectro en energía de interés hasta la energía de la segunda rodilla y mejorando sus capacidades para poder identificar la composición en masa de la partícula primaria hasta las energías más altas del espectro. En particular, una de esas actualización es la inclusión del detector de AMIGA ("*Auger Muons and Infill for the Ground Array*"), que resulta ser el detector en el que se centra este trabajo doctoral.

AMIGA centra su detección en la medición directa del contenido muónico de la cascada atmosférica del rayo cósmico primario (N_μ) y su desarrollo temporal en la atmósfera (X^{μ}_{max}) midiendo directamente el arribo temporal de los muones. Sus objetivos son, entre otros, medir observables representativos de la composición (o los evaluar los modelos hadrónicos) combinado con otros detectores del Observatorio, estudiando la transición de fuentes galácticas a extragalácticas. Estos objetivos acompañan los objetivos generales del Observatorio P. Auger, así como enriquecen el estudio de rayos cósmicos, permitiendo estudiar todo el espectro de energía desde la segunda rodilla en adelante en un único Observatorio.

Differentes tipos de esfuerzos se han invertido en obtener un detector que pueda medir la componente muónica con una resolución elevada como pudo lograrse con AMIGA. Dos trabajos diferentes han sido desarrollados durante esta tesis. El primero está relacionado con la actualización del sistema opto-electrónico

del detector de AMIGA. El segundo se relaciona con la incorporación de la medición directa de la componente muónica de la lluvia producida por un rayo cósmico, en la reconstrucción de universalidad.

Tras la conclusión de este trabajo se instaló el nuevo sistema de opto-electrónico completamente operativo y calibrado en 8 módulos de AMIGA en el sitio del Observatorio Pierre Auger. La actualización del detector consiste en un sistema de detección basado en SiPMs. Las principales motivaciones para esta actualización son las ventajas que estos dispositivos tienen en comparación con los MaPMT actuales: menor costo por canal, mayor vida útil, mejor robustez, menor voltaje de alta tensión de alimentación, mayor eficiencia de detección de fotones en la longitud de onda de emisión de fibra óptica, no hay interferencia óptica entre canales e insignificante presencia de señales posteriores a los pulsos. Las principales desventajas de los SiPM son su mayor tasa de ruido y su dependencia de la temperatura. Este ruido más alto fue utilizado como una ventaja para ajustar el método de calibración, y el PDE alto ayudó a modificar el nivel de discriminación de la señal del detector a valores más altos para evitar conteo accidental. Por lo tanto, la estrategia de conteo propuesta se basa en un criterio de discriminación por amplitud. Como resultado de la calibración desarrollada en este trabajo, se logró una alta eficiencia del detector, es decir, 98 % de eficiencia para la máxima polarización probada, combinada con una baja probabilidad de conteo accidental ($\sim 2\,\%$).

También se desarrolló un nuevo modelo para incluir las señales detectoras AMIGA en el modelo de señales de la reconstrucción con universalidad. El método de la universalidad propone una técnica novedosa basada en la forma universal que puede describir la lluvia de partículas producida por una partícula primaria de rayos cósmicos. La medición directa del contenido muónico de la lluvia, al incluir las señales AMIGA en el procedimiento de reconstrucción de la universalidad, reducirá significativamente las incertidumbres sistemáticas en la estimación de los parámetros principales que describen al rayo cósmico (E, X_{max}, y R_{μ}). Por lo tanto, el conocimiento de estos tres parámetros desde una detección híbrida seguida por la reconstrucción dentro del modelo de universalidad permitirá una identificación significativamente mejorada tanto del modelo hadrónico como de la composición en masa de partículas primarias. En esta identificación se encuentran los objetivos científicos propuestos del Proyecto Pierre Auger. La fuerza del modelo de señales de AMIGA de universalidad propuesto es que no depende ni de la partícula primaria de la lluvia ni del modelo hadrónico. Durante este trabajo, el modelo de señal para los detectores de muones de AMIGA es descrito y luego probado con diferentes modelos hadrónicos y primarios, mostrando una predicción precisa de los parámetros (menos de 10 % de sesgo en R_μ y E). Además, se reconstruyó un evento real de alta energía con el procedimiento de reconstrucción estándar y luego se comparó con los resultados obtenidos con la universalidad. Los resultados en energía y composición de masa obtenidos con la reconstrucción de la universalidad son compatibles con los resultados obtenidos con el detector FD para este evento.

Zusammenfassung

Kosmische Strahlung trifft die Erdatmosphäre als kontinuierlicher Fluss mit einem Energiespektrum über einen weiten Energiebereich. Ihr Fluss nimmt mit zunehmender Energie nach einem Potenzgesetz ab. Hochenergetische kosmische Strahlen sind von Bedeutung, da sie uns helfen können, unser Wissen über das Universum zu verbessern.

Die wichtigsten hochenergetischen Merkmale des Spektrums sind: Knie, zweites Knie, Knöchel und Spektrumunterdrückung, die jeweils aus einem bestimmten wissenschaftlichen Grund entstehen und mit der primären Masse verknüpft sind. Deshalb erweitert das Pierre-Auger-Observatorium sein Detektionssystem um die Region des zweiten Knies und verbessert die Massenidentifikation bis zu den höchsten Energien. Insbesondere wird eines dieser Upgrades AMIGA ("*Auger Muons and Infill for the Ground Array*") genannt, was das wichtigste Detektorsystem ist, das in dieser Promotionsarbeit angesprochen werden soll.

AMIGA basiert auf einer direkten Messung des Myongehalts (N_μ) und von X^μ_{max} mittels detaillierter Myon-Ankunftszeiten. Ihre Ziele sind die Messung von Beobachtungsobjekten in Verbindung mit anderen Auger-Detektoren bei LHC-Energien und darüber, die den Übergang von galaktischen zu extra-galaktischen kosmischen Strahlenquellen untersuchen. Diese Ziele umfassen die allgemeinen Auger-Ziele und Verbesserung der Suche nach Photonen, so dass die gesamte Spektralregion ab dem zweiten Knie mit einem einzigen und einzigartigen Observatorium untersucht werden kann.

Nach Abschluss dieser Arbeit wurde ein voll funktionsfähiges und kalibriertes neues optoelektronisches System in 8 Modulen von AMIGA in der im Pierre-Auger-Observatorium installiert. Das Upgrade des Detektors besteht aus einem SiPM-Detektionssystem. Die Hauptmotivationen für dieses Upgrade sind die Vorteile, die diese Geräte im Vergleich zu aktuellen MaPMTs haben: niedrigere Kosten pro Kanal, längere Lebensdauer, bessere Robustheit, niedrigere Hochspannung, höhere Photonen-Detektionseffizienz bei der Wellenlänge der Lichtwellenleiteremission, kein optisches Übersprechen zwischen den Kanälen

und vernachlässigbare Nachimpulse. Die Hauptnachteile von SiPMs sind die höhere Rauschrate und die Temperaturabhängigkeit. Dieses höhere Rauschen wurde als Vorteil genutzt, um die Kalibriermethode einzustellen, und die hohe PDE half dabei, den Diskriminierungsgrad des Detektorsignals auf höhere Werte zu ändern, um ein versehentliches Zählen zu vermeiden. Die vorgeschlagene Zählstrategie basiert daher auf einem Amplitudenkriterium. Als Ergebnis der in dieser Arbeit entwickelten Kalibrierung wurde eine hohe Detektoreffizienz erreicht, d.h. 98 % Effizienz für den höchsten getesteten Polarisationsspannungswert, kombiniert mit einer geringen Wahrscheinlichkeit des zufälligen Zählens ($\sim 2\%$).

Auch ein neues Modell wurde entwickelt, um AMIGA-Detektorsignale in das Signalmodell der Universalität der Rekonstruktion einzubeziehen. Schauerunivsalität ist eine Methode, die es erlaubt mittels weniger makroskopischer Größen, wie Energie, X_{max}, R_{mu} universelle Parametrisierungen der Signal- und Ankunftsverteilung der detektierten Sekundärprodukte zu erstellen. Direkte Myonenbestimmung, durch die Einbeziehung der AMIGA-Signale in das universelle Rekonstruktionsverfahren, werden die systematischen Unsicherheiten bei den Hauptparametern der kosmischen Strahlung (E, X_{max} und R_{μ}) signifikant reduzieren. Die Kenntnis dieser drei Parameter aus einer hybriden Detektion mit anschließender Rekonstruktion innerhalb des Universalitätsmodells wird es daher ermöglichen, eine wesentlich bessere Identifizierung sowohl des hadronischen Modells als auch der primären Massenzusammensetzung zu verfolgen. Auf dieser Identifizierung beruhen die vorgeschlagenen wissenschaftlichen Ziele des Pierre-Auger-Projekts. Die Stärke des vorgeschlagenen universellen MD-Modells liegt darin, dass es weder vom Primärteilchen der Kaskade noch vom hadronischen Modell abhängt. In dieser Arbeit wird das Signalmodell für die Myon-Detektoren von AMIGA beschrieben und dann mit verschiedenen hadronischen Modellen und Primärenteilchen getestet, wobei die Parameter gezeigt und präzise vorhergesagt werden (weniger als 10% Bias in beiden Fällen, R_{μ} und E). Weiterhin wurde ein energiereiches Realereignis mit dem Standardrekonstruktionsverfahren rekonstruiert und mit den Ergebnissen der Universalität verglichen. Die Ergebnisse in Energie und Masse Zusammensetzung, die mit der Universalität Rekonstruktion sind kompatibel mit den Ergebnissen, die mit dem FD-Detektor für dieses Ereignis.

Contents

Chapter 1

Cosmic Rays

Cosmic rays (CR) impact the earth atmosphere as a non-stopping flux with an energy spectrum over a wide energy range. Their flux decreases with increasing energy following a power law. In this thesis work, high energy cosmic rays (HECR) will be considered as those with $E \geq 10^{17}$ eV.

Victor F. Hess was awarded in 1936 the Nobel Prize due to his work related to the discovery cosmic rays radiation [77]. During his balloon flights in 1911-1912, he concluded that the ionization observed with his electroscopes, come from outside Earth, since it did not necessarily decrease with increasing altitude. R. Millikan confirmed the existence in 1925 and named the radiation "cosmic rays" [52]. Many years after it was demonstrated that most of the radiation was due to charged particles and only a small portion was due to gamma rays, as Millikan thought. Still, the name "cosmic rays" was kept for historical reasons.

Pierre Auger in 1938 discovered that particles arrived on ground in time coincidence to detectors placed far away to each other [8]. He claimed that those particles came from an unique origin. This was the discovery of extensive air showers (EAS) produced by cosmic-ray primaries. Following his hypothesis, he predicted that thousands of particles were produced during the shower development in the atmosphere and that primary particles must have energies higher than 10^{15} eV. This discovery was of high importance since cosmic rays became the source of the highest energy particles in nature. As a consequence, cosmic rays were employed as the source of high-energy particles during several decades and particles, such as the positron, were discovered.

1.1 Cosmic rays

From the wide energy spectrum of cosmic rays coming from different sources over the universe, HECR are a very interesting goal since they are the highest energy particles. Man-

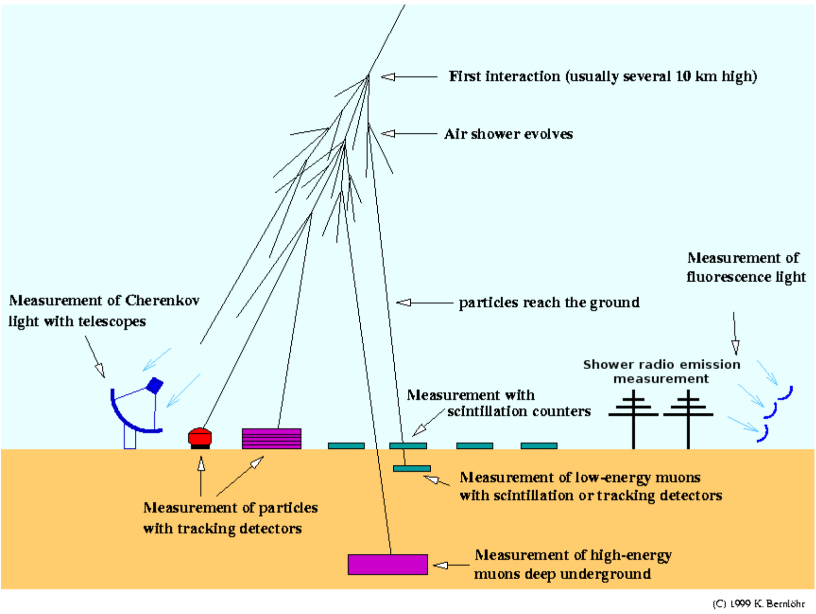

Figure 1.1 Different air shower detection techniques.

made accelerators on Earth do not reach these energies, proton beam at CERN reach an energy of 6.5 TeV. HECR low fluxes prevent a direct observation of the primary particle, therefore Observatories rather concentrate on the detection of their EAS produced while traversing the Earth atmosphere. Large acceptance detector systems are placed on the Earth surface. Noteworthy to mention, as a pioneer of large detector arrays, is the Volcano Ranch Observatory (New Mexico) deployed in the sixties by the MIT group. It covered an area of 12 km^2 with 20 stations in a triangular grid, and it showed the existence of ultra-HECRs by observing the highest energy primary particle up to that moment: 10^{20} eV particle [34].

There are several types of air shower detectors (see Figure 1.1).

Many experiments use one or several of these techniques.

- Shower arrays that study the shower size and the lateral distribution on the ground: tracking detectors, calorimeters or scintillation counters on ground or underground.
- Cherenkov detectors that detect the Cherenkov radiation emitted by the charged particles of the shower.
- Fluorescence detectors that study the nitrogen fluorescence excited by the charged particles in the shower. The fluorescence light is emitted isotropically so the showers can be observed from the side.
- Radio antennas that measures the radio emission of the air shower.

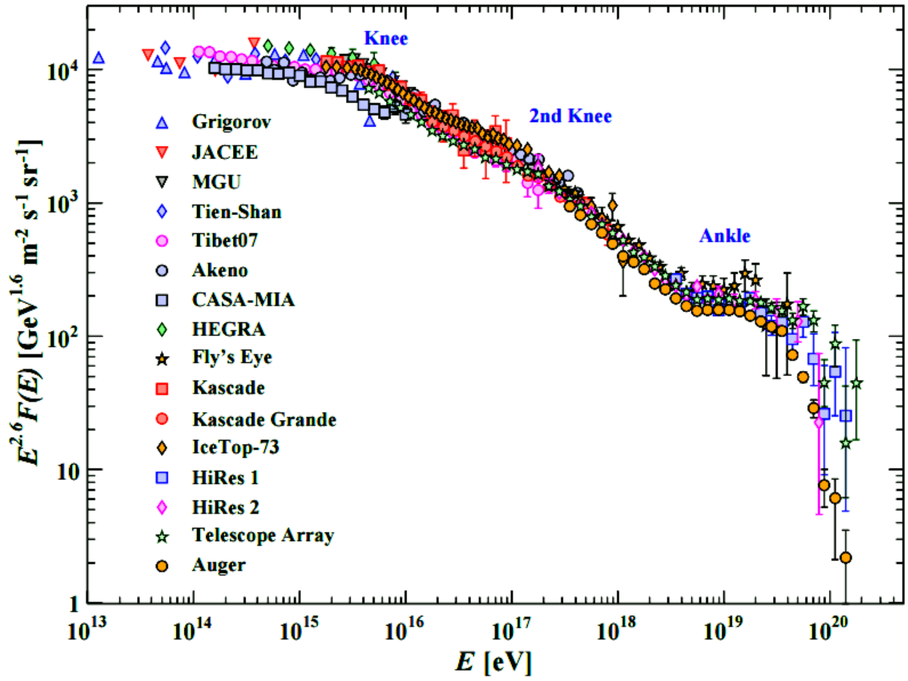

Figure 1.2 Cosmic ray spectrum detected from different experiments. Extracted from [55]

Detailed simulations and cross-calibrations between different types of detectors are convenient to control systematic uncertainties and particularly to establish the primary energy spectrum from air-shower experiments. Decades after their discovery, the measurement of the energy spectrum of HECRs remains as one of the main topics within the field, being fundamental to understand the origin of these particles, their propagationin space, chemical composition, and hadronic models governing their interactions.

In most of the cases, the change in the arrival rate of CRs with primary energy, is described by the differential flux $J(E) = dN/dE$, considered as the observed number N of CRs with energy between E and $(E + dE)$ per unit area, solid angle, and time interval. The CR spectrum flux is spread over a very wide rage of energies that goes from 10^9 eV to 10^{20} eV. A combined cosmic-ray flux from different experiments is depicted in Figure 1.2 as a function of the primary CR energy. This spectrum is the result of the combination of the production spectrum of the particles in their sources with the energy losses produced during their propagation through the cosmos.

The flux spectrum can be approximately described by a power law $dN/dE = E^{\gamma}$. The steepening that occurs between 10^{15} and 10^{16} eV is known as the *knee* of the spectrum. In this region, the spectrum index γ, changes from ~2.7 to ~3.1. Around $\sim 10^{17}$ eV there is another change in the spectral index, the *second knee*. The other remarkable feature around

$10^{18.5}$ eV [63] is called the *ankle* of the spectrum. Finally the cutoff at the end of the spectrum is an abrupt flux suppression of ultra-HECRs at $\sim 4 \times 10^{19}$ eV [63].

In the second knee region is more uncertain and it is not consistently observed by different Observatories at the same energy. AGASA Collaboration reported the second knee at $\sim 4 \times 10^{17}$ eV [45], in contrast to KASCADE Grande that did it at $\sim 1 \times 10^{16,9 \pm 0,1}$ [6] and an Auger PhD thesis [15]. In the energy range starting in the ankle, the flux is extremely low (1 particle per km^2 per year), producing a growth in detection area requirements to get enough statistic.

The change in the spectral index at the knee and second-knee would reflect the fact that most cosmic accelerators in the galaxy have reached their maximum energy as explained by the KASCADE (Karlsruhe Shower Core and Array Detector) [76] and KASCADE-Grande Observatories. There are consecutive cut-offs of individual spectra for different primaries proportional to their charge Z [6] [7] starting with proton primaries at the knee. The second-knee under this scenario would correspond to the heaviest element, the iron cut-off energy.

The second knee-ankle region is of paramount importance to understand the transition from galactic to extra-galactic CR sources, i.e., where the extra-galactic flux component dominates over the galactic component [45]. A possible explanation of the ankle is that the spectrum dip corresponds to this transition region.

The reduction in the CR flux at $\sim 4 \times 10^{19}$ can be differently explained depending on the primary mass. The current state-of-the-art [73] suggests two possible explanations: the maximum energy attained by cosmic accelerators or the GZK cutoff.

Under the first scenario, cosmic accelerators will reach a maximum energy with the heaviest primaries. This is then a similar explanation to the already made for the second-knee but for galactic sources. Still, there would be a difference in composition since disintegration will be lesser significant for galactic sources than for extra-galactic sources due to the difference in transportation distances: heavier elements loose energy during propagation in the intergalactic medium by disintegration and electron-positron production.

Under the second scenario the highest energy CRs would be protons. Protons will loose energy via pion production during their propagation. This latter process is named the GZK cut-off named after their proposers Greisen [25], and independently by Zatsepin and Kuzmin [78]. The HiRes fluorescence experiment [53] detected some evidence of the GZK suppression. The Pierre Auger Observatory reports the spectrum suppression at 4×10^{19} eV [4]. On the other hand, observations of the Auger Observatory are more consistent with heavier masses rather than protons and therefore with the first scenario [71], but a proton component is not negated.

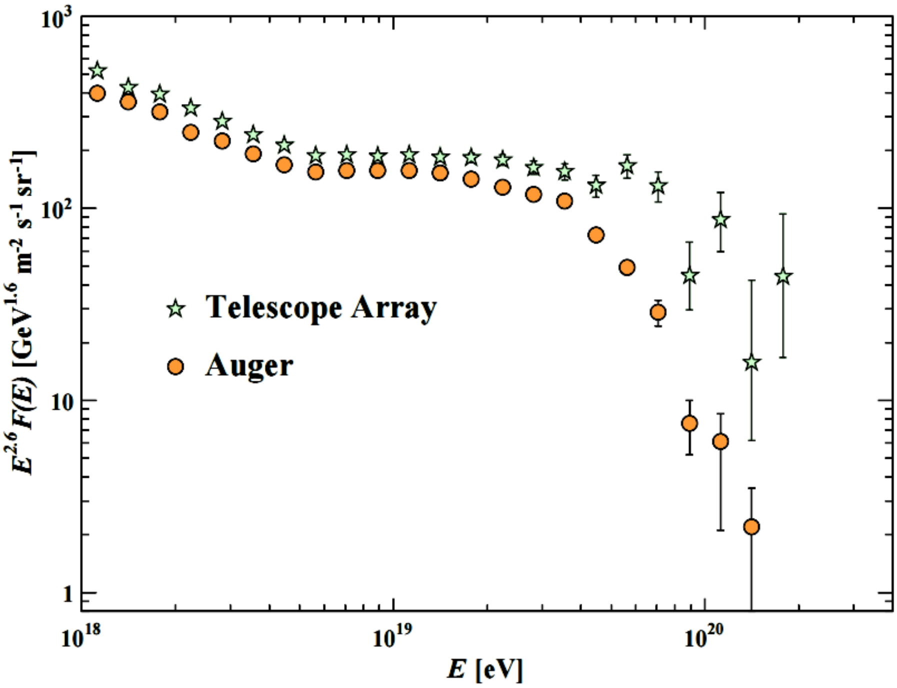

Figure 1.3 Cosmic ray spectrum detected by TA and PAO. Extracted from [55]

The Telescope Array (TA) [14] has also presented a spectrum showing this suppression. The differential energy spectra measured by both TA and Auger agree within systematic uncertainties (see Figure 1.3).

Moreover, a comparison of the energy evolution of the mean of X_{max} as measured by the Telescope Array and Pierre Auger Collaborations, after accounting for the different resolutions, acceptances, and analysis strategies of the two experiments, show that the two results are in good agreement within systematic uncertainties [44], see Figure 1.4.

1.2 Extensive air showers

A cosmic ray shower is a thin disc composed by thousands of particles spread in radial distances that travel at a speed close to the speed of light. In short, this atmospheric cascade may be described by its development in the atmosphere in terms of the amount of particles at different atmospheric depths (*longitudinal profile*) and its distribution in radial distance from the shower axis (*lateral distribution*). Figure 1.5 depicts these two main characteristics.

As stated by Pierre Auger, air showers start very high in the atmosphere where the first interaction of the primary CR with the atmosphere takes place. There are different CR primaries and this work is focused on hadronic cosmic rays, i. e. those initiated by

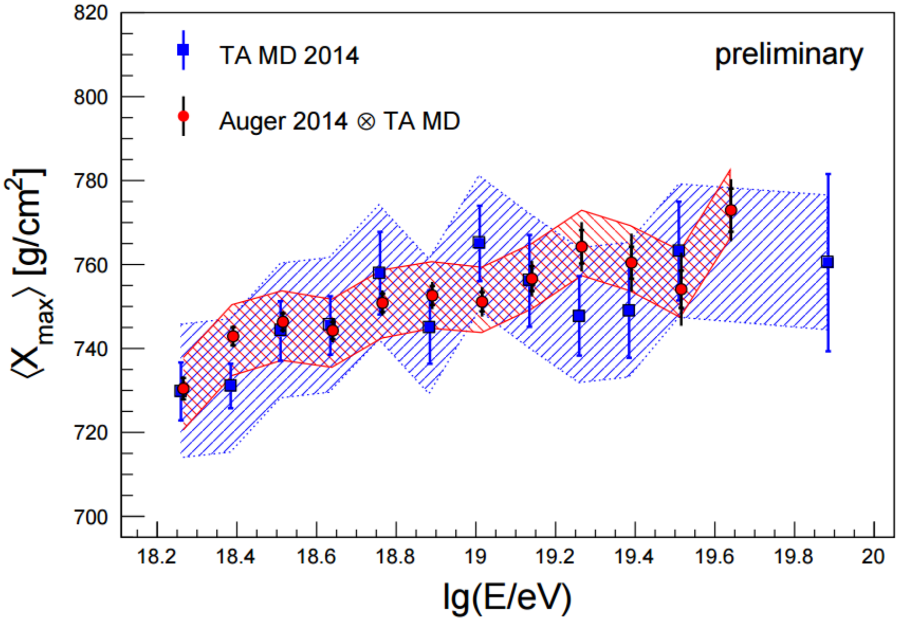

Figure 1.4 Mass composition results from PAO and TA after preliminary corrections to make possible the comparison of both detector results. Extracted from [44].

a nucleus. After the first interaction, the particles keep interacting again and this process is repeated many times generating the atmospheric cascade and increasing the number of particles produced. On each generation of interactions, approximately 30% of the particles energy is transfer to the electromagnetic component (electrons and gamma photons) via π^0 decays. This electromagnetic cascade carries at the end ~90% of the primary particle energy. The remaining energy goes into muon and neutrino productions, that are products of charged pions and kaons decays. An overview of the different components of the air-shower is in Figure 1.6.

The primary particle energy that goes into the electromagnetic component is almost proportional to it, however, the amount of muons that reach the ground level grows up slower with the primary CR energy which is used to estimate the mass composition of the primary. Heitler developed a simplified model [62] based on these topics. It considers that the electromagnetic shower develops in branches and, from each branch, the energy is divided equally into two new branches following a characteristic mean free path (λ) After n ramifications ($n = X/\lambda$) the amount of particles N can be described as in Equation 1.1.

$$N(X) = 2^{\frac{X}{\lambda}} \tag{1.1}$$

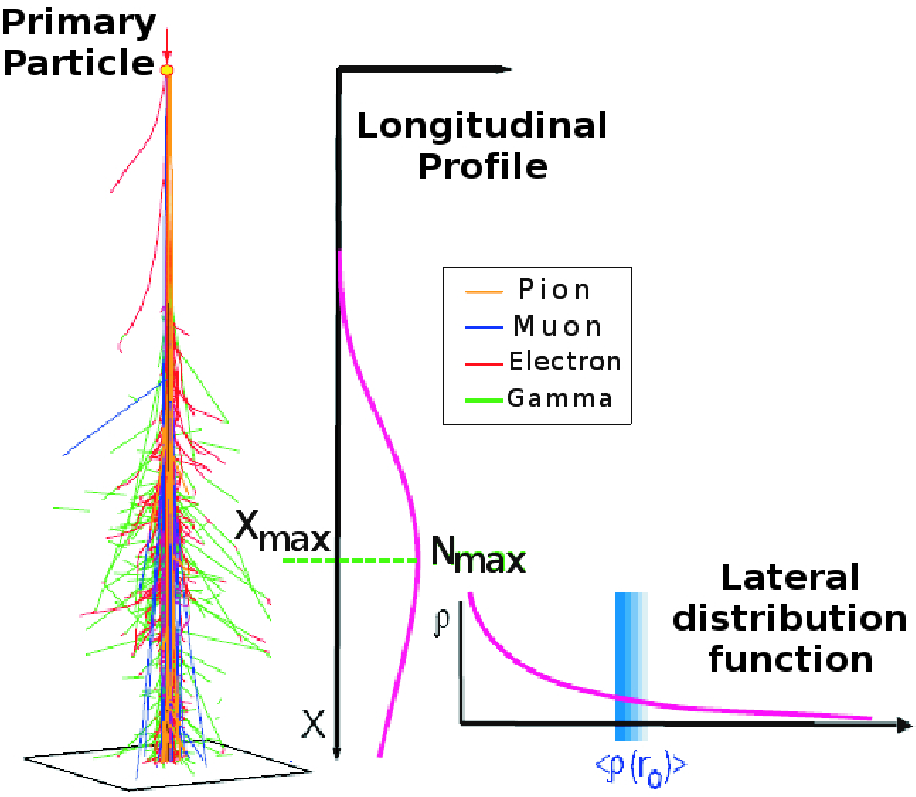

Figure 1.5 Longitudinal and lateral air shower particle distribution.

where X is the atmospheric depth, and therefore the electromagnetic longitudinal profile depends strongly on the amount of atmosphere the particles passed through. Then, the particle energy as a function of the primary particle energy can be written as in Equation 1.2.

$$E(X) = \frac{E_0}{N(X)} \tag{1.2}$$

These interactions continue up to a certain energy ($E(X) = E_c$) at which the particles can only be absorbed, lose energy, or decay. Due to this, there is an atmospheric depth (X_{max}) at which the air-shower develops its maximum amount of particles (N_{max}).

$$N_{max} = N(X_{max}) = \frac{E_0}{Ec} = 2^{\frac{X_{max}}{\lambda}} \tag{1.3}$$

$$X_{max} = \lambda \frac{ln(\frac{E_0}{E_c})}{ln2} \tag{1.4}$$

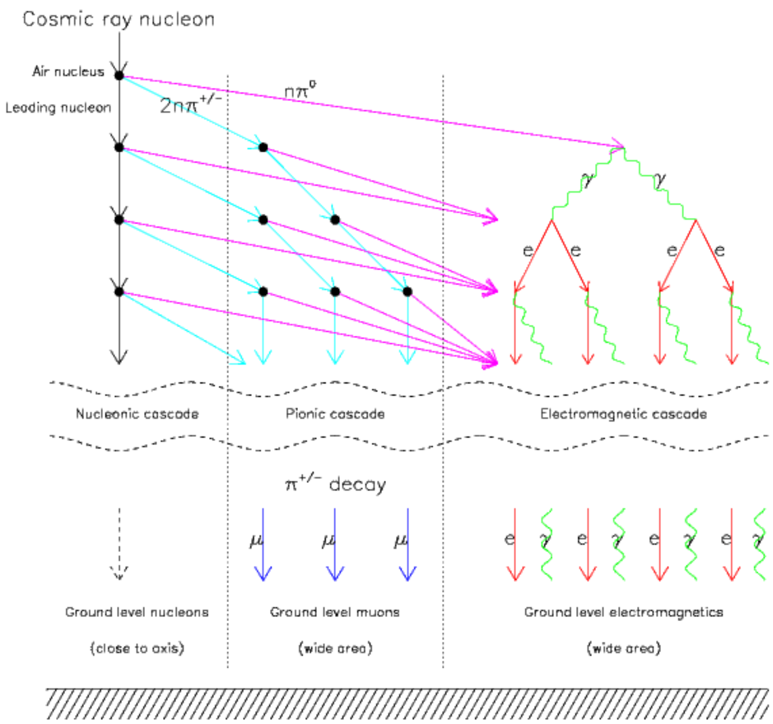

Figure 1.6 Schematic overview of the interactions in the atmosphere.

The muon content can also be described in a simplified way. From the total n_{total} amount of new particles produced by an hadronic interaction of a particle of energy E, two thirds are estimated to be charged particles ($n_{charged}$) and one third neutral particles ($n_{neutral}$). The last ones, decay immediately into electromagnetic particles ($\pi^0 \rightarrow 2\gamma$). It can be assumed also that charged particles decay into muons, we they reach their typical decay energy (E_{decay}). Following the description, charged particles will reach E_{decay} after n interactions.

$$E_{decay} = \frac{E_0}{(n_{total})^n} \tag{1.5}$$

Assuming each charged particle produces one muon (and a neutrino not considered in this simplification), the number of muons can be estimated as follows.

$$N_\mu = n_{charged}^n = \left(\frac{E_0}{E_{decay}}\right)^\alpha \tag{1.6}$$

With $\alpha = \ln \mathrm{n_{charged}} / \ln \mathrm{n_{total}} \approx 0.82 \cdots 0.95$. This evidences that the number of muons produced by an air shower depends not only on the primary energy and air density but also on the total particle multiplicities (composition). These considerations are used in several detector designs.

It was shown in this Chapter the main high-energy features of the spectrum (knee, second-knee, ankle, and spectrum suppression) each of which arises from a particular scientific reason to be unraveled and which are all linked to the primary CR mass. For this purpose, Auger is upgrading its detection system to include the second-knee region and to improve the mass identification up to the highest energies. In particular one of these upgrades is called AMIGA ("*Auger Muons and Infill for the Ground Array*") which is the main detector system to be addressed in this thesis work (see Chapter 3).

Chapter 2

The Pierre Auger Observatory

The Pierre Auger Observatory [75] was originally conceived to measure the energy and arrival directions of cosmic rays and to assess their mass composition from $E = 10^{18}$ eV to the highest energies with high statistical significance. The astrophysical interest in this energy range is well known as described in the previous chapter.

As mentioned before, above 10^{20} eV; the flux of events decreases abruptly down to about $1\,\mathrm{km}^{-2}\,\mathrm{sr}^{-1}\,\mathrm{century}^{-1}$ and for that reason, the way to reach the aimed statistical significance at the highest primary energies, is by observing over a vast area. The Pierre Auger Observatory was planned as a hybrid detection system encompassing a surface array over $3{,}000\,km^2$ of 1,600 water Cherenkov detectors arranged in a 1.5 km triangular grid plus four sites on the periphery, each one containing six telescopes measuring the air-fluorescence light produced by the atmospheric cascade during the shower development. Therefore, the surface array detects the air-shower lateral distribution while the telescopes detect its longitudinal profile.

2.1 Surface Detector

A surface detector station consists of a 3.6 m diameter water tank containing a sealed liner with a diffusive-reflective inner surface. The liner is filled with 12,000 liters of ultra-pure water. Three XP1805/D1 photomultiplier tubes (PMTs) manufactured by Photonis are symmetrically distributed on the surface of the liner at a distance of 1.20 m from the tank center axis and look inside the liner through transparent windows. These PMTs record Cherenkov light produced by relativistic charged particles passing through the water. The tank height of 1.2 m makes it also sensitive to high energy photons, which convert to electron-positron pairs in the water volume. Each surface detector station is isolated and self-contained. A solar power system provides the power needed to feed up the PMTs and electronics of

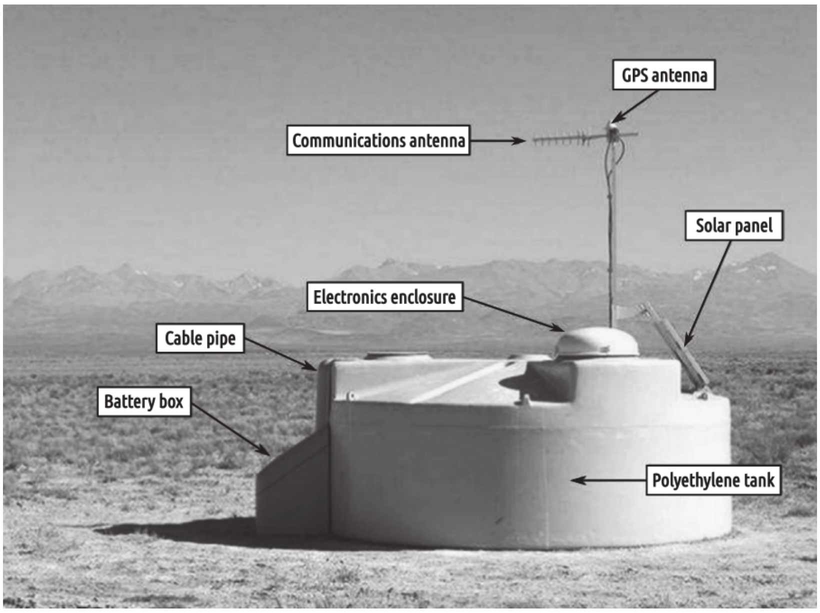

Figure 2.1 A surface detector in the field and its main components.

each surface detector station. An schematic overview of the surface detector is shown in Figure 2.1. In Reference. [32] a detailed description of the surface detector is found.

The individual surface detector stations are deployed in a triangular array nearby Malargüe, Mendoza, Argentina. Figure 2.2 shows the layout of the surface array and the FD buildings at its periphery.

The tanks are manufacture of polyethylene with resins to prevent ultraviolet damage, resulting in a low cost and uniform detector, robust against environmental elements. The interior of the wall was compounded with carbon black to guarantee light-tightness. The external side was coloured beige similar to the landscape. Each tank has inside a liner made of a flexible plastic material that provide a light-tight environment and diffusively reflect the Cherenkov light produced in the water volume. The liner has three windows through which the three PMTs of each SD station look into the water volume from above. These windows are made of UV transparent low-density polyethylene. Each PMT is optically coupled to a window with optical silicone and shielded above by a light-tight plastic cover. Three hatches, located above the PMTs, provide access to the interior of the tank for water filling, installation, and servicing of the interior parts. Once deployed in their correct positions in the field, the tanks are filled with ultra-pure water. Tests in a sampling of detectors have indicated that ultra-pure water does not show bacterial growth which could lead to reduced water clarity. Because of its high purity, the water is expected to maintain its clarity during the Observatory lifetime.

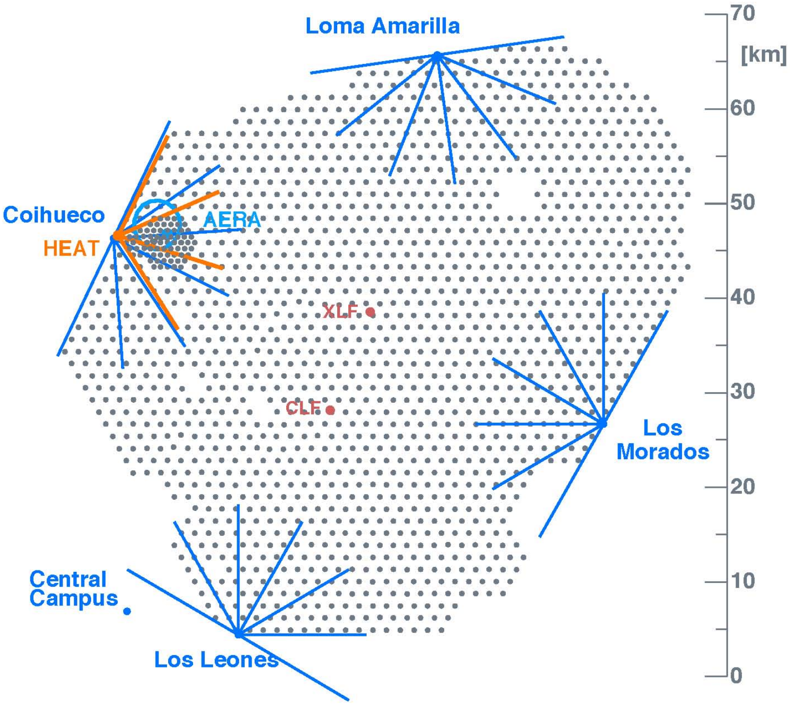

Figure 2.2 Pierre Auger Observatory map. Both surface and fluorescence detectors positions are plotted.

When charged particles pass though the pure water, they produce Cherenkov light in the water volume of the detectors. This light is collected by the three PMTs mentioned before. The PMTs have a 9 in. diameter photocathode and eight dynodes, with the chemical composition of the dynode surfaces optimized by the manufacturer to maximize linearity. Due to their proximity to water they are operated with a positive anode voltage and a grounded photocathode. The high voltage is provided locally from a module integrated in the PMT base, and is proportional to a DC control voltage provided by the slow-control system. Each PMT has two outputs: an AC coupled anode signal and the signal of the last dynode. In addition, the signal at the last dynode is amplified and inverted by the PMT base electronics to provide a signal with 32 times the charge gain of the anode. No shaping of the signal is applied on the PMT base. The maximum signal recorded before saturation corresponds approximately to 650 times the peak current of a vertical muon traversing the tank, which corresponds to the signal from a 100 EeV cosmic ray at about 500 m from the shower core. The front-end is interfaced to a unified board which implements the station controller, event timing, and slow-control functions, together with a serial interface to the communications system. The slow-control system consists of DACs and ADCs used to measure temperatures, voltages, and currents relevant to the assessment of the operation of the station. The electronics is protected by an aluminium dome that keeps out rain and dust.

Electrical power is provided by solar panels which feed two 12 V, 105 Ah, batteries wired in series to produce a 24 V system. The batteries are accommodated in a battery box. Since battery lifetime is reduced with higher temperature, the battery box is protected from direct sunlight by installing it on the shaded side of the tank. Power is expected to be available over 99 % of the time. The cables have a special coating to protect them from environmental damage. The solar panels are mounted on aluminium brackets, which also support a mast where antennae for radio communication and GPS reception are mounted at the top. Each SD station contains also a GPS receiver with its corresponding antenna for event timing and communication synchronization. Event timing is determined using a custom 27 bit clock operating at 100 MHz. This clock is latched on the GPS signal at the time of each shower trigger. A counter operating at the 40 MHz ADC clock is also latched on the GPS clock. These data, together with the timing corrections provided by the GPS receiver, are used to calibrate acquisition frequencies within 10 ns RMS.

In the following subsection a brief description of the SD trigger and its calibration is included.

2.1.1 SD trigger and calibration

The Cherenkov light recorded by a surface detector is measured in units of the signal produced by a muon traversing the tank on a vertical trajectory. This unit is named as the vertical equivalent muon (VEM). The goal of the surface detector calibration is to measure the value of one VEM in integrated FADC channels. The conversion to units of VEM is done both to provide a common reference level between tanks and to calibrate against the detector simulations. During shower reconstruction, the signal recorded by the tanks is converted into units of VEM, and the total shower energy and arrival direction are fitted using a lateral-distribution function and energy conversion based on hybrid analysis using the FD. The total bandwidth available from each SD station to the Central Data Acquisition System (CDAS) is 1,200 bit/s, which requires that the calibration must be performed by the local electronics. Also, the remoteness of the detectors implies that the calibration procedure must be robust, allowing for failures of individual PMTs, without data losses.

$\mathrm{Q}_{\mathrm{VEM}}^{\mathrm{peak}}$ (called $\mathrm{Q}_{\mathrm{VEM}}$ hereafter) is defined as the bin containing the peak in the charge histogram of an individual PMT response, and $\mathrm{I}_{\mathrm{VEM}}^{\mathrm{peak}}$ (called I_{VEM} hereafter) as the bin containing the peak in the pulse-height histogram. These quantities are used in the three main steps in the calibration procedure [75]:

- Set up the end-to-end gains of each of the three PMTs to have I_{VEM} at same channels.
- In order to compensate for drifts, adjust the electronics level trigger by continually performing a local calibration to determine I_{VEM} in channels.
- Determine the value of Q_{VEM} to high accuracy using charge histograms, and use the known conversion from Q_{VEM} to one VEM to obtain a conversion from the integrated signal of the PMT to VEM units.

The high voltages, and thus the gains of each of the three PMTs, are tuned to match a reference event rate. This tuning implies that the PMTs in the SD stations will not have equivalent gains, even for PMTs in the same tank. If, for example, a particular SD station has more detected photons per vertical muon than the average station, then the PMTs in this station will be operated at a lower gain than average to compensate. In addition to the primary conversion from integrated channels to VEM units, the calibration must also be able to convert the raw FADC traces into integrated channels. There are 6 FADC inputs, the anode and dynode of each of the three PMTs of each tank. The primary parameters needed for the calibration are then the baselines of all six FADC inputs, and the gain ratio between the dynode and anode. The calibration parameters are updated every 60 s and returned to CDAS with each detected event and stored with the event data. Each event therefore contains information about the state of each SD station in the minute preceding the trigger, allowing for an accurate data calibration. In Reference [32] a detailed description of the calibration method is included.

These traces are also used to decide on triggers for shower candidates. Several independent local-trigger functions are implemented in the front-end electronics: the scaler trigger, the calibration trigger, and the main shower trigger.

The *scaler trigger* records pulses with a very low threshold for auxiliary physics purposes such as space weather.

The *calibration trigger* collects low threshold pulses using a small number of bins (~ 20) thus providing high-rate cosmic-ray data. Data from the three high gain channels are stored from three samples before the trigger to 20 samples after the trigger. These data are used to build calibration histograms and are also used offline to convert the six FADC traces into VEM units.

The main trigger is the *shower trigger* that results in the recording of 768 samples ($19.2\,\mu s$). It has two selection levels. The first level, called T1, has 2 independent modes. The first one is a simple threshold trigger (TH) requiring the coincidence of all three PMTs being above 1.75 I_{VEM}. This trigger is used to select large signals that are not necessarily spread in time. The threshold has been adjusted to reduce the rate of atmospheric muon

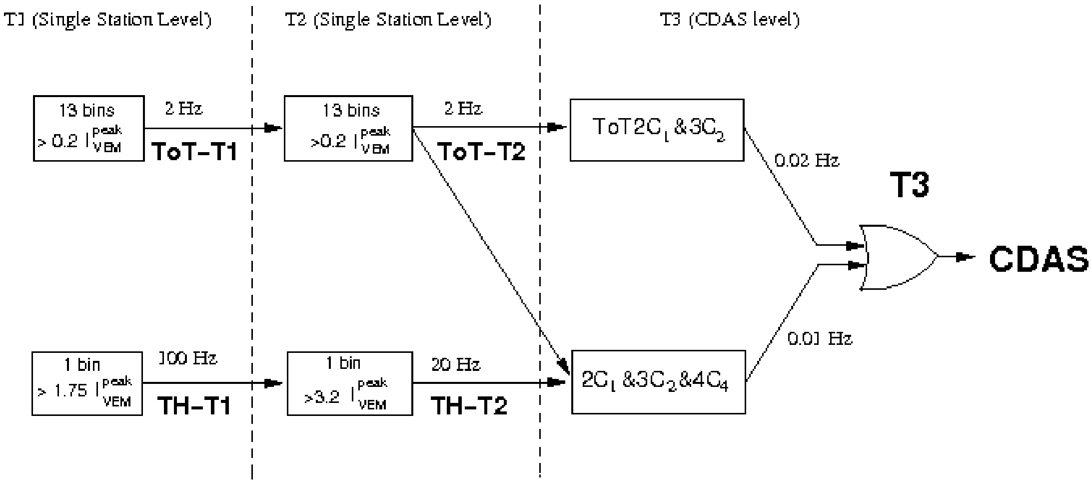

Figure 2.3 Surface-detector triggers schematic flux diagram.

triggers from about 3 kHz to 100 Hz. The second T1 mode is a time-over-threshold trigger (ToT) requiring that at least 13 bins within a 3 μs window (120 samples) exceed a threshold of 0.2 I_{VEM} in coincidence for two out of the three PMTs. The ToT trigger selects sequences of small signals spread over time, and is thus efficient for the detection of vertical events, and more specifically for stations near the core of low energy showers, or stations far from the core of high-energy showers. The rate of the ToT trigger depends on the shape of the particle pulse in the tank and averages to 1.2 Hz. The ToT trigger rarely corresponds to accidental particles impinging the detector due to its structure in time. The second trigger level, called T2, is applied to decrease the global rate of the T1 trigger down to about 23 Hz. While all T1-ToT triggers are promoted to T2-ToT, only T1-TH triggers passing a single threshold of 3.2 I_{VEM} in coincidence for the three PMTs will pass this second level and become T2-TH. See Figure 2.3 for a schematic view. All T2s send their timestamp to CDAS for the global trigger (T3) determination. More details on the triggers can be found in [68].

In June 2013, the Observatory installed across the entire array two additional SD T1 triggers. These triggers are built by applying more sophisticated analyses to the FADC traces as detailed below:

- The time-over-threshold-deconvolved (ToTd) trigger deconvolves the exponential tail of the diffusely reflected Cherenkov light pulses before applying the ToT condition. This has the effect of reducing the influence of muons in the trigger, since the typical signal from a muon, with fast rise time and $\sim$ 60 ns decay constant, is compressed into one or two time bins.

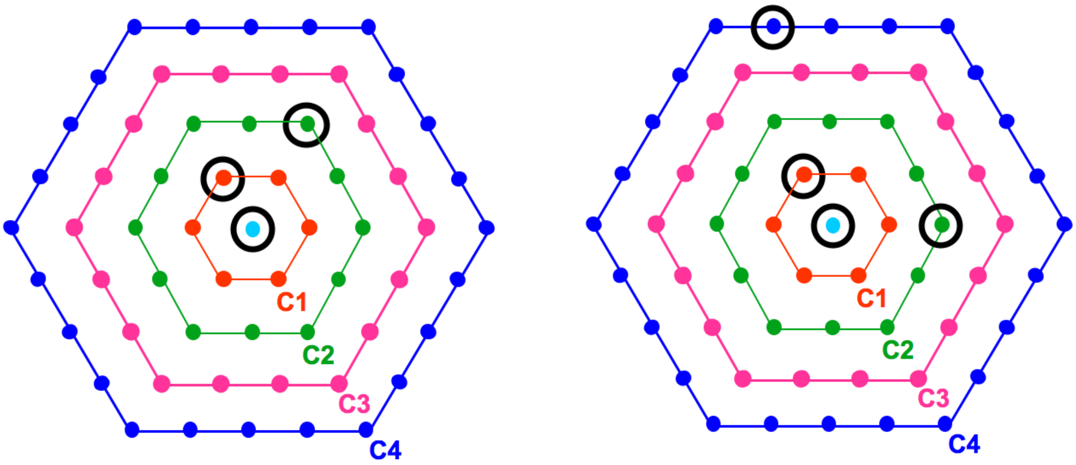

Figure 2.4 T3 trigger requirement on station level. Examples of T3 configurations: the 3-fold T3 mode $ToT2C_1\&3C_2$ is shown on the left and the 4-fold mode $2C_1\&3C_2\&4C_4$ on the right hand side, respectively (see text for details). C1, C2, C3, C4 indicate the first, second, third, and fourth crowns of neighbours. Extracted from [68].

- The multiplicity of-positive-steps trigger (MoPS), on the other hand, counts the number of positive-going signal steps in two of three PMTs within a 3 μs window. This reduces the influence of muons in the trigger.

Both ToTd and MoPS triggers also require the integrated signal to be above $\sim$ 0.5 VEM. Because these triggers minimize the influence of single muons, they reduce the energy threshold of the array, while keeping random triggers at an acceptable level. Thus they improve the energy range of the SD, as well as the trigger efficiency for both photon and neutrino showers.

In the following paragraphs, some examples of the T3 conformation are explain. The T3 trigger is decided based on two prescriptions [68] taking into account only the original T1 triggers. The first one requires the coincidence of at least three detectors that have passed the ToT condition and that meet the requirement of a minimum of compactness, namely, one of the detectors must have one of its closest neighbours and one of its second closest neighbours triggered. This T3 trigger is called $ToT2C_1\&3C_2$, see Figure 2.3 and Figure 2.4. Once the spatial coincidence is verified, also a timing criteria is imposed. An example of such T3 configuration is shown in Figure 2.4, left. Since the ToT as a local trigger has very low background, this trigger selects predominantly physics events. The rate of this T3 with an operative full array is around 1600 events per day, meaning that each detector participates in an event in mean value 3 times per day. This trigger is extremely pure since 90% of the selected events are real showers and it is mostly efficient for showers below 60°.

The second T3 mode is more permissive. It requires a four-fold coincidence of any T2 with a moderate compactness. Namely, among the four fired detectors, within appropriate time windows, at least one must be in the first set of neighbors from a selected station (C_1), another one must be in the second set (C_2) and the last one can be as far as in the fourth set (C_4). This trigger is called $2C_1\&3C_2\&4C_4$, see Figure 2.4. Such a trigger is efficient for the detection of horizontal showers that, being rich in muons, generate in the detectors signals that have a narrow time spread triggered detectors. With the full array configuration, this trigger selects about 1200 events per day, out of which about 10% are real showers.

The data acquisition system implemented on each station transmits the time stamps of the $\sim$ 23 T2 events collected each second to CDAS. CDAS returns T3 requests to the station within 8 s of the event (including communication delay due to retransmission). The station controller then selects the T1 and T2 data corresponding to the T3 requests and builds it into an event for transmission to CDAS. Calibration data is included in each transmitted event. The information is then stored for its offline analysis.

2.1.2 Triggering and storing data

The Central Data Acquisition System (CDAS) [75] was designed to assemble the triggers from the surface array detectors, to allow control of these detectors, and to organize data storage. It is constructed using a combination of commercial hardware and custom made, high level, software components. The system is designed to run continuously, with minimum intervention, with the full 1660 (1600 stations of the main array and 60 extra stations of the infill described in the next chapter) detector array, and can manage many more. Data from the FD are recorded separately at the FD locations and transferred daily to the CDAS at Malargüe, although hybrid coincidences are identified online within the SD data stream. The primary role for the CDAS is to combine local trigger information from the SD stations in order to identify potential physical events generating an SD higher level trigger (T3). These triggers combined with the T3 from FD sites (FD T3) are used to generate a request for the relevant data from SD stations for those events. The CDAS is then used to combine and store these data to form a shower event. The CDAS also contains configuration and control mechanisms, the means to monitor system performance, and the tools to access and download SD monitoring, calibration, control, and configuration data.

Except for triggering information, the CDAS and the FD data acquisition systems are completely independent. The merging of FD and SD data is made offline during the daytime following an FD run. Data are synchronized on the central storage hardware after each observation night. The newly acquired data within the central storage are mirrored at the Auger primary data mirror located at the Lyon HEP Computer Center (France) every 3 hs;

later these data can be transferred to secondary mirror sites. The data may then be transferred from a convenient mirror site to over 50 participating institutions. The disk storage system of the CDAS is comprised of redundant disk arrays installed in each server plus some standalone devices. A Network Time Protocol (NTP) GPS clock is used to synchronize system times. The whole system is installed in a Computer Center at the Observatory campus, with controlled temperature and redundant uninterruptible power supply. The data flow over the radio network, from individual SD stations to the central campus.

The datum received from each SD station belongs to different data streams:

- Local triggers, T2: the highest priority stream, with a list of time stamps and the type of trigger (threshold or time over threshold), is forwarded to the "Central Trigger" application.
- Shower data with its calibration data: data in this high-priority stream are sent only when a request is received from the CDAS at an SD station. Shower events are split into small pieces and sent together with the T2 packets so that the available bandwidth is fully used.
- Control: this is a medium-priority stream that describes the state of the detector.
- Calibration and monitoring information: this is a low-priority data stream.

The triggering system of the Observatory fulfils two conditions. Firstly, it detects showers with high efficiency across the SD array. This efficiency is above 99% for vertical showers with energy above 3 EeV. Secondly, it allows and identifies cross-triggers (hybrid events) between the FD and SD systems. FD triggers use separate algorithms but are forwarded to the SD system to construct the hybrid data set.

To apply the main trigger condition (T3), the system defines concentric hexagons centered on each station. The "Central Trigger" processor is used to identify groups of stations that are clustered in time and space as SD events. To begin with time clusters are sought by centering a window of $\pm 25\,\mu s$ on each T2. Clusters, with multiplicity of three or more, are then examined for spatial coincidences, following the description included in Subsection 2.1.1.

As already mentioned, the DAQ system of the fluorescence detector is independent from the CDAS. Local triggers are generated at each FD site and those identified as T3 FD event triggers are logged by a local processor if a shower track is found. T3 FD event triggers are transmitted online (within 1 s) from the local FD site to the CDAS system at the central site. The trigger information sent describes the geometry of the shower candidate. This includes the estimated time of arrival of the light front of the shower at the camera as well as the geometry. From this information, the time of impact of the shower at a ground position in the region of the SD stations is computed and a corresponding SD event T3 is constructed. All FADC traces recorded within $20\,\mu s$ of the computed time are assembled as a normal "SD only" event, but with the addition of the identification of the corresponding T3 FD trigger. After each night of operation, details of events recorded at the FD telescopes for each T3 FD event triggers are transferred to the CDAS. Data from these triggers are then merged with the data collected by the SD DAQ and form the hybrid data set. A hybrid event is therefore an "FD only" event together with a special SD event that contains all the information from the surface stations that were in space and time coincidence with the FD event.

2.2 Fluorescence Detector

As mentioned before, the 24 telescopes of the Fluorescence Detector (FD) look inside the SD array from four sites: Los Leones, Los Morados, Loma Amarilla and Coihueco (See [67] for details). Each site is composed of six independent telescopes located in a clean climate controlled building. One of the buildings is seen in Figure 2.5. Each single telescope has a field of view of $30\,\text{deg} \times 30\,\text{deg}$ in azimuth and elevation, with a minimum elevation of $1.5\,\text{deg}$ above the horizon. The combination of the six telescopes provides $180\,\text{deg}$ coverage in azimuth. The telescopes face towards the interior of the array. An schematic description including its principal components of each FD telescope is included in Figure 2.6

The telescope design is based on Schmidt optics since it reduces the coma aberration of large optical systems. During the development of the air shower, nitrogen fluorescence light is emitted isotropically, and enters through a circular diaphragm covered with a filter glass window. This filter transmission is above 50% (80%) between 310 and 390 nm (330 and 380 nm) in the UV range. The filter reduces the background light flux and thus improves the signal-to-noise ratio of the measured air-shower signal, and also serves as a protection over the aperture (keeps the room containing the telescopes and electronics clean and climate controlled). An extra shutter is placed as the last layer protecting the telescopes from daylight. It closes automatically at night when the wind becomes too strong or rain is detected. In addition, a curtain is mounted behind the diaphragm to prevent daylight from illuminating a camera in case of a malfunction of the shutter. These additional precautions are needed since the detectors work in an stand-alone mode.

Inside the room, a simplified annular lens, which corrects spherical aberration and eliminates coma aberration, is mounted in the outer part of the aperture.

Fluorescence light is focused by a spherical mirror of $\sim$3,400 mm radius of curvature onto a spherical focal surface with radius of curvature $\sim$1,700 mm. Due to its large area

Figure 2.5 Los Leones FD building, telecommunication antenna, and an SD station.

($\sim 13\,\mathrm{m}^2$), the primary mirror is segmented to reduce the cost and weight of the optical system. The average reflectivity of a cleaned mirror segments at a wavelength λ = 370 nm is more than 90%.

The camera body is machined from a single block of 60 mm thickness. The hexagonal photomultiplier tubes, model XP3062 manufactured by Photonis, are positioned inside 40 mm diameter holes at the locations of the pixel centres. The pixels are arranged in a matrix of 22 rows by 20 columns. The PMT boundaries are approximate hexagons with a side-to-side distance of 45.6 mm. To prevent photons losses in the dead spaces between the PMT cathodes, simplified Winston cones are placed in the separation between PMTs, serving as light collectors. The pixel field of view defined by the upper edges corresponds to an angular size of 1.5deg.

All support structures and cables are distributed so as to minimize any obscuration in the light path. The room is completely dark to avoid contamination of the detected signal due to reflections. The reflectivity of a few selected mirror segments is measured once or twice each year and it changes less than 1% per year. Moreover, additional methods using data measured by telescopes were used, such as star tracking, Central Laser Facility (CLF) and eXtreme Laser Facility (XLF) shots, or a comparison of FD and SD geometry reconstruction. Throughout each night of FD operation, thousands of collimated UV laser pulses are directed into the atmosphere from two facilities located near the center of the SD (CLF and XLF). Both are a Q-switched frequency tripled YAG laser. Light pulses delivered to the sky with

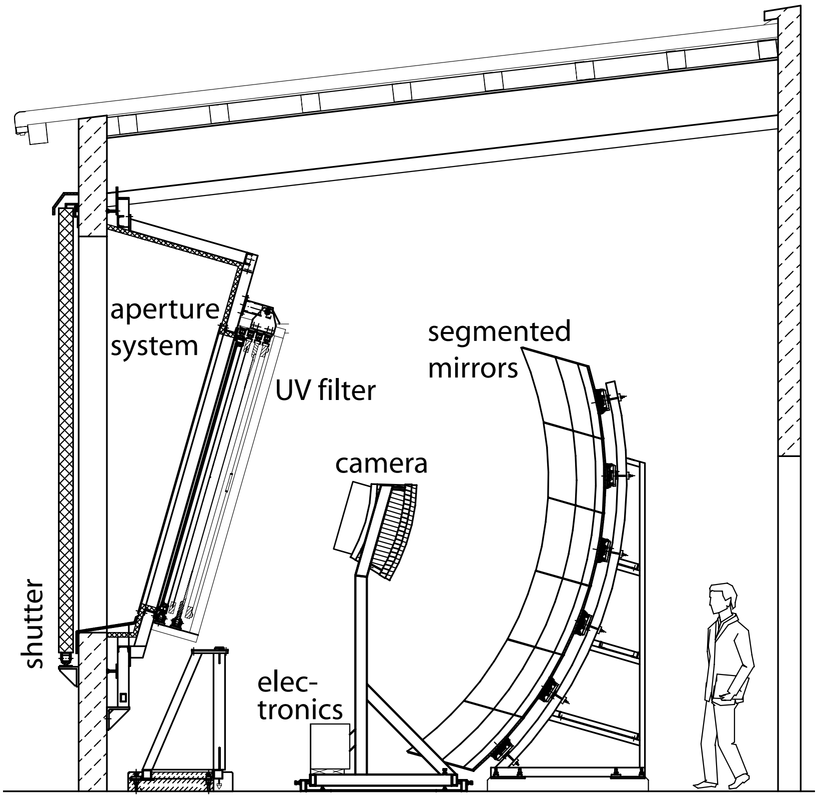

Figure 2.6 Schematic description of the main components of an FD telescope.

spectral purity of the 355 nm better than 99.9%. This wavelength falls between the two major N_2 fluorescence bands of 337 nm and 357 nm. Light scattered out of the laser pulses generates tracks in the same FD telescopes that also record the tracks generated by air showers. In contrast to high-energy air showers, the direction, rate, and energy of the laser pulses can be preprogrammed as desired. Laser pulses can be fired at specific directions relative to the ground, for example vertically. An optical fibre at each laser directs a small amount of light into an adjacent SD station to provide hybrid laser events. Laser data recorded by the FD telescopes are used to measure FD performance, measure SD-FD time offsets, check FD pointing, and make the hourly measurements of aerosol optical depth vertical profiles for the atmospheric database.

The FD electronics must provide linearity in a large dynamic range and strong background rejection. The selected photomultiplier tube (XP3062) is an 8-stage unit with a bialkaline photocathode with quantum efficiency of about 25% in the wavelength range 350-400 nm. The normal dark sky background (moonless nights, when the FD operates) induces an anode current of about 0.8 μA on each PMT. The PMT signal is shaped and digitized in the front-end electronics (FE) unit, where threshold and geometry triggers are also generated.

Analog boards in the FE unit are designed to handle the large dynamic range required for air fluorescence measurements; this means a range of 15 bits and 100 ns timing.

The trigger rate of each pixel in a camera (*first level trigger*) is kept around 100 Hz by adjusting the pixel threshold level. The algorithm of the *second level trigger* searches for track segments at least five pixels in length within a camera. The typical trigger rate per camera fluctuates between 0.1 and 10 Hz. The *third level trigger* is a software algorithm designed to clean the air shower data stream of noise events that survive the low-level hardware triggers. It is optimized for the fast rejection of triggers caused by lightning and by impacts of atmospheric muons on the camera.

The events surviving all trigger levels are sent through the local computer to the so-called EyePC, which builds an event from the coincident data in all telescopes at a given site and generates a hybrid trigger (FD-T3) for the surface array. The event rate is about 0.012 Hz per site for the 24 baseline telescopes.

The reconstruction of air shower longitudinal profiles requires the conversion of an ADC count into a light flux for each pixel with a portion of the signal from a shower. To this end, the absolute calibration of the detector response is needed. A calibrated drum-shaped light source provides an absolute, end-to-end calibration for each pixel of the fluorescence telescopes. An independent verification for some pixels by atmospheric Rayleigh scattering from vertical laser pulses is also implemented. From the end-to-end calibration, the appropriate constants are found to be approximately 4.5 photons/ADC count for each pixel. To derive a flux of photons for observed physics events, the integrated ADC number is multiplied by this constant and divided by the area of the aperture. The flux in photons per m^2 perpendicular to the arrival direction is thus obtained. Other calibrations and cross checks are performed to ensures a long term reliability of the detector.

2.2.1 FD extension: High Elevation Auger Telescopes (HEAT)

Three additional fluorescence telescopes with an elevated field of view were built about 180 m in front of the FD site at Coihueco [26]. These telescopes are very similar to the original fluorescence telescopes but can be moved upward with an electrically driven hydraulic system. These three telescopes work independently of other FD sites and form the "fifth site" of the Observatory (see Figure2.7). HEAT telescopes were designed to allow a determination of the cosmic ray spectrum and X_{max} distributions in the energy range from 0.1 EeV up to the ankle. For that purpose they cover the elevation range from 30deg to 58deg, which lies above the field of view of the other FD telescopes.

The main objective of this extension was to lower the energy threshold of hybrid data to enable an unbiased detection of nearby low-energy showers. In combination with the

Figure 2.7 High Elevation Auger Telescopes (HEAT) photograph. This three new telescopes are deployed close to Coihueco to complement its field of view, allowing the detection of lower energy showers.

SD, information from an 60 positions of an infilled array of water Cherenkov detectors on a 750 m grid close to the HEAT site, the energy range of high quality hybrid air shower measurements has been extended down to 10^{17} eV. The HEAT telescopes can be tilted using the hydraulic mechanism. The telescopes are parked in the horizontal position between the FD data taking periods to be accessible for maintenance. The same position is used for the absolute calibration of the HEAT telescopes and also for the cross-calibration with telescopes at Coihueco. All three HEAT telescopes are usually moved in the upward position before the first DAQ night and stay there during the whole data taking period.

The response of the HEAT cameras was tested at multiple elevations using the relative calibration method. The effect on the signal of tilting HEAT is at one percent level or below, which matches the overall magnitude expected due to the direction of the Earth's magnetic field as seen by the PMTs. Also, the absolute calibration may be determined in the horizontal mode. The Schmidt optics of the HEAT telescopes, camera body, PMTs, light collectors, etc., are the same as in the other sites. A feature that sets HEAT apart from the classic Auger telescopes is its new electronics kit that can sample up to 40 MHz instead of 10 MHz. In practice, a sampling rate of 20 MHz was chosen. The higher rate improves the measurement for close showers that have a correspondingly larger angular velocity. From this it follows that the first level trigger interval was reduced to 50 ns, whereas the second level trigger continues to operate every 100 ns. The length (in time) of the FADC traces remains the same, so the number of bins doubles. The trigger rate of the HEAT telescopes is high, particularly due to the Cherenkov light from nearby low-energy showers.

2.3 Other extensions of the Observatory and Observatory Upgrade

Since the beginning of the Pierre Auger Observatory, new methods of air shower detection have been developed. These new ideas were guided by the physics of cosmic rays that was revealed by analysis of the detected data set. Research and development is currently advanced on different techniques which complement the array of water Cherenkov and air fluorescence detectors. In the next Chapter the *Auger Muon and Infill for the Ground Array* (AMIGA) extension will be described in detail. In this section the *Auger Engineering Radio Array* (AERA) and the *Surface Scintillator Detector* (SSD) upgrades are going to be briefly described. They will allow a multi-detector study of the primary cosmic-ray.

2.3.1 Auger Engineering Radio Array (AERA)

High-energy cosmic-ray air showers generate radio emission via two processes: one is a geomagnetic, current-induced emission mechanism [17]; the other is a charge-excess mechanism [23]. One of the particularities and advantages of the AERA detector is that the observation of air showers can be done even during the day. Moreover, radio signals are sensitive to the development of the electromagnetic component of particle showers in the atmosphere of the Earth and, in particular, to the X_{max} of the incoming cosmic ray [57].

The questions to be addressed in the VHF band (30-300 MHz) are whether radio signals can be used to determine the primary energy, the arrival direction, and contribute towards determining the mass composition of cosmic rays. If so, may a large surface detector array based on the radio detection technique be built within an affordable price? The Pierre Auger Collaboration has started and is well advanced in a research program to answer both questions. Various prototypes at the site of the Pierre Auger Observatory have already been deployed and commisioned [11] [35] [69].

AERA enhancement is based on radio detection, a technique that was first pursued elsewhere many years ago but is now benefiting from recent advances in electronics.

Each radio detection station has a dual polarization antenna, sensing the electric field in the north/south and east/west directions. This antenna is associated to analog and digital readout electronics, an autonomous power system and a communication link to a central data acquisition system. The antennas are sensitive between 30 and 80 MHz. AERA deployment began in 2010 with 24 stations. These stations are equipped with logarithmic periodic dipole antennas and are connected via a fibre optic link to a central data acquisition site. Stable physics data taking started in March 2011, and the first hybrid detection of cosmic ray events

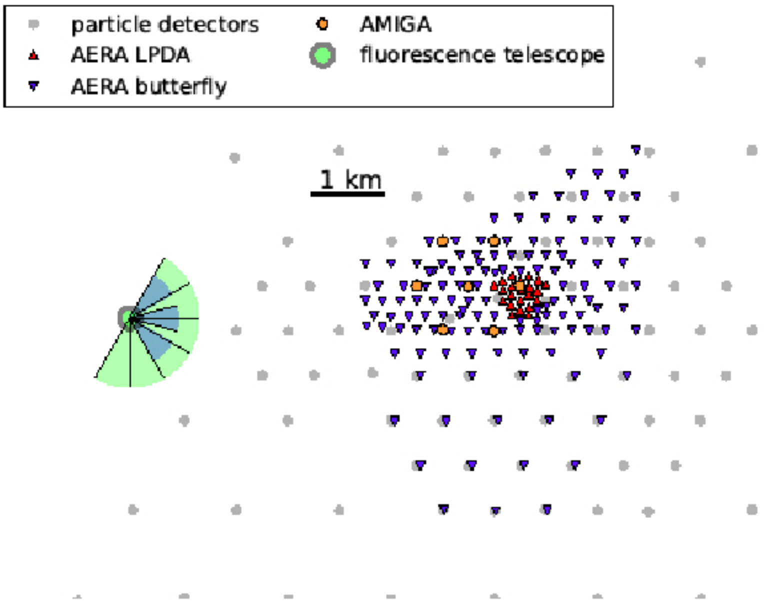

Figure 2.8 Distribution of AERA antennas in the AMIGA site of the Pierre Auger Observatory.

by radio, fluorescence, and surface particle detectors was recorded in April 2011. In May 2013 an additional 100 stations equipped with butterfly antennas were installed. Detailed simulations and measurements demonstrated that butterfly antennas perform better for narrow pulse detection as compared to the logarithmic periodic dipole antennas.

AERA now includes 153 radio detection stations, spread over an area of $17\,\mathrm{km}^2$. The detector spacings range from 150 m to 750 m, which enables the full exploitation of radio detection of air showers. An overview of the AERA antennas distribution in the field is included in Figure 2.8.

Since this radio technique is rather new, the emission mechanisms need to be understood. The contributions of the main emission mechanisms have been measured recently. Simultaneously, experiment and theory are being connected through software tools where end-to-end simulations and data analysis can be performed within the same software package.

As a second step the data obtained with radio detection stations deployed at the Observatory will be used to check their sensitivity with respect to the determination of the air shower parameters. Hardware and software are being developed to study the required specifications and performance of solitary radio stations as a blueprint for a larger array.

Chapter 3

AMIGA: Auger Muon and Infill for the Ground Array

The main objectives of the Auger Observatory are 1) to find cosmic-ray sources at the highest energies (charged-particle astronomy for proton-like primaries), 2) elucidate the missing muon component (composition, hadronic models, new physics), and 3) study exotic primaries, namely photons and neutrinos. As described in Chapter 2, these three goals are intimately linked to primary mass composition. Note also that composition and hadronic interactions are strongly interwoven [70] [1] [54] since the latter rules the shower energy partition between electromagnetic and hadronic components mainly by means of pion productions and decays. As such, research at lower energies (i.e. $10^{16} - 10^{17}$ eV) has the enormous advantage to give an anchoring point for the hadronic interaction from LHC results.

The optimum detector measurements for each cosmic ray event are its energy, $\mathrm{X}^{\mathrm{e}}_{\mathrm{max}}$ (or $\mathrm{X}^{\mu}_{\mathrm{max}}$), and the number of muons at an optimal lateral distance from the shower axis, N_{μ}. Leaving aside any of these three parameters might seriously handicap the above-mentioned physics goals. Once and only once these parameters are measured, the best available multiparametric fit (e.g. Universality) may be applied.

AMIGA is based on a direct measurement N_{μ} and of $\mathrm{X}^{\mu}_{\mathrm{max}}$ via detailed muon arriving times with reduced systematics in energy calibration. As originally planned, AMIGA consists of two in-filled arrays at 433 and 750 m detector distances. The 433 and 750 m arrays are estimated to be fully efficient at $E \geq 10^{16.6}$ and $10^{17.1}$ eV, respectively. As such, AMIGA physics objectives are:

- Measure composition/hadronic models related observables in conjunction with the FD and SD detectors at LHC energies and above.

- Study the second-knee region, explore the heavy knee as observed by Kascade-Grande. Transition from galactic to extra-galactic cosmic-ray sources.

- Study photons in a) the 0.1 EeV region [61] and b) in the region of gamma production from the GZK model (0.1-10 EeV).

- Cast light on the missing extragalactic proton component in the below-ankle region.

These objectives encompass the general Auger 2) and 3) objectives and allow a smooth and safer transition towards objective 1). They also enrich cosmic-ray research with studies from $10^{16.6}$ eV allowing the whole spectrum region from the second-knee onwards to be studied with a single and unique Observatory.

As above-mentioned, in order to fully describe the cosmic ray flux, the optimum set of detector measurements for an event include energy, $\mathrm{X}^{\mathrm{e}}_{\mathrm{max}}$ or $\mathrm{X}^{\mu}_{\mathrm{max}}$, and N_{μ}. If an Observatory aims at getting these parameters with good resolution, quality measurements of both shower muonic and the electromagnetic components are needed.

AMIGA is designed to measure muon arrival times and the number of muons at the detector position. Combining this information, the reconstruction of the longitudinal profile and the ground-level lateral distribution of muons can be obtained. These two observables reduce energy reconstruction systematics and improves the mass composition estimation, particularly when the fluorescence detector is not operating. Note that AMIGA can directly measure the muonic component with a nearly a 100% duty cycle.

As a general description, the AMIGA 750 m array Auger's enhancement consists of an in-filled area of 61 detector pairs, each one composed of a surface water-Cherenkov detector combined with a buried 30 m^2 Muon Detector (MD). These MDs are deployed on a 750 m triangular grid, that is half distance of the original 1.500 m array. This spacing within an area of 23.5 km^2 was chosen due to the small particle footprint and high flux of lower-energy showers.

3.1 Muon detector module description and Unitary Cell

MDs have a modular design in which the 30 m^2 detection area is divided into two modules of 5 m^2 and two of 10 m^2 in the engineering array configuration (Figure 3.1, left). This modular design will be simplified for the production phase to three 10 m^2 modules (Figure 3.1, right). In this thesis work by MD is understood all modules in a single position, while a Muon Module (MM) is referred to as each individual detector system. So MDs will have an area of 30 m^2 while MMs either of 5 or 10 m^2. Each MD is associated to a SD station. Since many

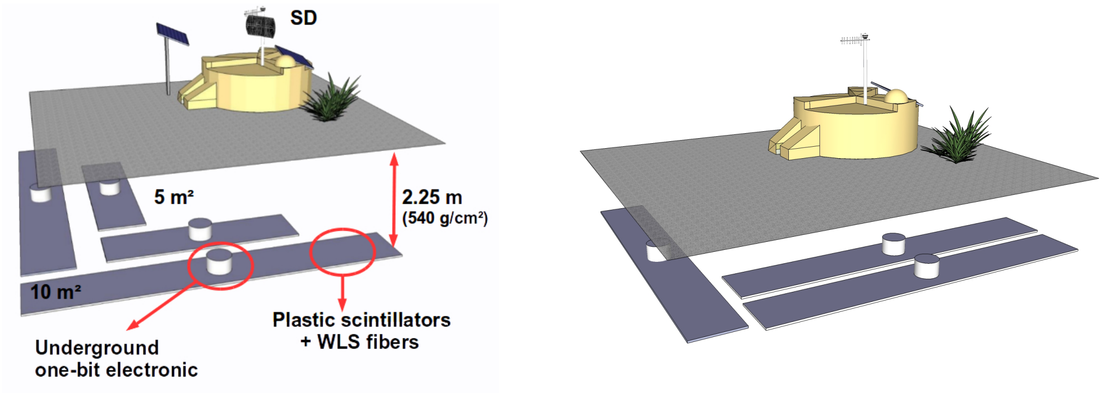

Figure 3.1 Schematic view of a MD combined with a SD station. On the left the engineering array design and on the right the production design.

detectors are to be deployed in the field over a large-area array, a photovoltaic system with a low-power electronics design must be developed too.

3.1.1 AMIGA Modules

Following AMIGA physics purposes, a plastic scintillator was selected for particle detection. The AMIGA module design in though to efficiently detect underground muons, with a simple, low-cost and low power consumption electronics. The scintillating area of each module is segmented in order to lessen muon pile-up within a fixed time window, since two muons arriving in the same time window will be counted as one. The minimum muon time window is defined by the convolution of the decay times of the scintillator and the optical fiber. The detection area was chosen to be 30 m^2 divided in 192 segments (see [5] for details about detection area and segmentation simulations and selection). Therefore, every scintillator module consist of 64 scintillation bars, each measuring 40 mm × 10 mm × 400 mm (for the 10 m^2 modules), with a 1.2 mm diameter wavelength-shifting (WLS) optical fiber glued into a lengthwise groove of the bar [72].

Each scintillation bar is an extruded bar of polystyrene doped with fluorine and co-extruded with TiO_2 as an outer layer to increase reflectivity and light collection. The dopants follow the proportions: 1% PPO [2,5-diphenyloxazole] and 0.03% POPOP [1,4-bis(5-phenyloxazole-2-yl)benzene], by weight of base material. Both dopants scintillate, but the PPO is more efficient. However, PPO emitted UV-wavelength light is attenuated in short distances. Therefore, POPOP is introduced as a first WLS to shift UV photons to blue-like ones. These dopant components result in a blue-emitting scintillator with an emission maximum at approximately 420 nm. The resulting attenuation length of the extruded

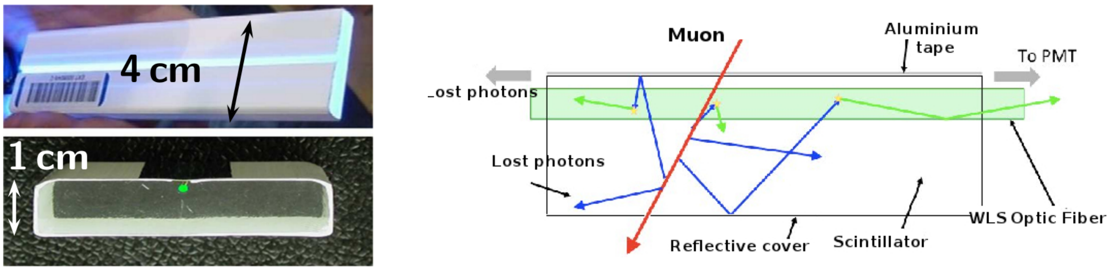

Figure 3.2 Left: an AMIGA scintillator with its groove on top with the WLS glued. Right: schematic view of the process produced when a charged particle impinges the detector.

scintillation bars is (55 ± 5) mm for the fast component and approximately 24 cm for the slow component. Therefore, the light must be carried to the photon-sensitive detector using an optical fiber. This optical fiber must be a WLS in order to collect photons from the side and scintillate inside the fiber. Photons produced with an angle contained in the transmitting cone of the fiber are going to be transmitted. To avoid the light emitted to the back of the module, the fiber end is cut off with a 45° angle. Only the light transmitted in the direction of the photosensitive detector is consider. To place the fiber, the bars have a 2.0 mm groove centered on the top side without a TiO_2 coating (see Figure 3.2, left). The WLS optical fiber is glued in the groove with an optical cement that matches the refractive index of the fiber and the scintillator, reducing photon loss. Then, the uncoated groove, with the optical fiber inside, is covered with a reflective aluminum foil to increase photon collection. The fibers used in the AMIGA modules are the Saint-Gobain BCF-99-29AMC multi-clad fibers. Its absorption spectra overlaps with the emission spectra of the scintillators. The light produced in the scintillation bars is collected and propagated along the WLS fibers, which then couple to a photon-sensitive detector (multianode photon-multiplier tubes or silicon photomultiplier, MaPMT and SiPM, respectively). Schematically, the process produced when a particle impinges the detector is described in Figure 3.2, right.

The main components of each MM and the distribution of the scintillating bars and fibers in it are shown in Figure 3.3. The fibers coming from the 32 scintillators on each side of the module are joined to the MaPMT/SiPM by an optical connector made out of black POM (black Polyoxymethylene). The 64 optical fibers are threaded and glued inside the drilled holes of the optical connector. Then a fly-cutter milling machine is used to simultaneously cut and polish all the fiber ends and the connector's front face. This flattened face is then coupled with optical grease to the fotomultiplier. The MaPMT used in AMIGA modules is the H8804-200MOD manufactured by Hamamatsu. The SiPM readout will be explained in Section 3.3. The 64 scintillators and optical fibers are covered with a PVC (Polyvinyl Chloride) casing and, together with the electronics kit, form the MM.

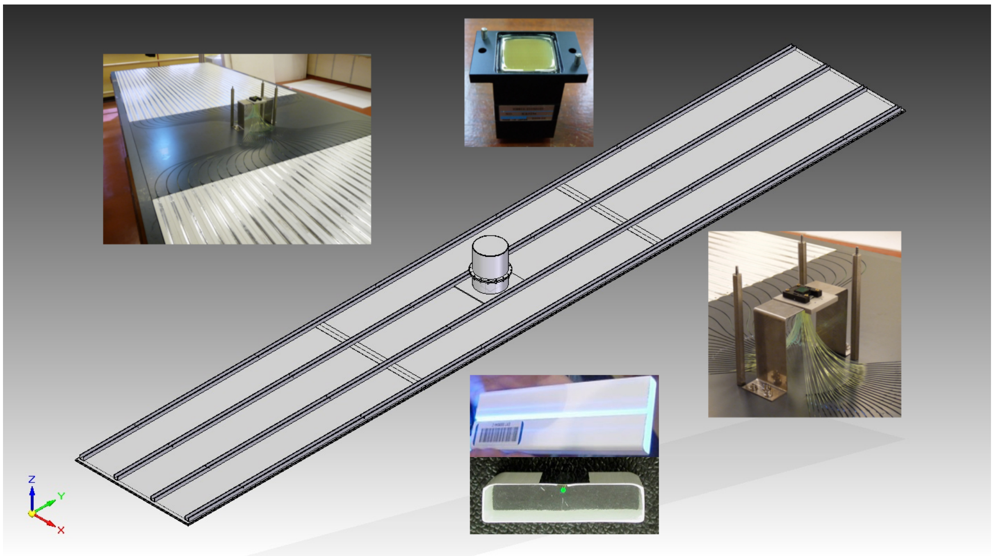

Figure 3.3 A 10 m^2 MM and its main components.

A complete description of module manufacturing and deployment can be found in [72].

3.1.2 AMIGA Electronics

An AMIGA MM can either work as a charge adder (total summed up shower signal at a MM position processed by a dual-ADC) or as a counter, being the latter the main working condition. For this last operation mode, the electronics of a module is designed to identify pulses above a given threshold. The thresholds of the 64 channels of the module can be individually set. A counting strategy is applied offline to the resulting traces to allow muon counting without a detailed knowledge of either the signal structure or peak intensity. This procedure relies on the muon-pattern identification in the time structure of the pulse pattern generated by the impinging muon on the detector, and not on the amplitude or charge of the produced signal. As a consequence, the design looks for a minimal dependency on the MaPMT gain (and its fluctuations), the muon impact position on the scintillator bar, and the corresponding light attenuation along the fiber length. These three last assumptions are the tested one when an individual module efficiency is studied. It also does not require thick scintillators to reduce the uncertainty introduced by poisson fluctuations in the number of SPEs (single photo-electrons) produced by the impinging particle. However, it does rely on fine counter segmentation to prevent under counting due to simultaneous muon arrivals. It additionally depends on the adjustment of thresholds within an appropriate range to ensure good counting efficiency, combined with and adequate MaPMT high-voltage selection. Once

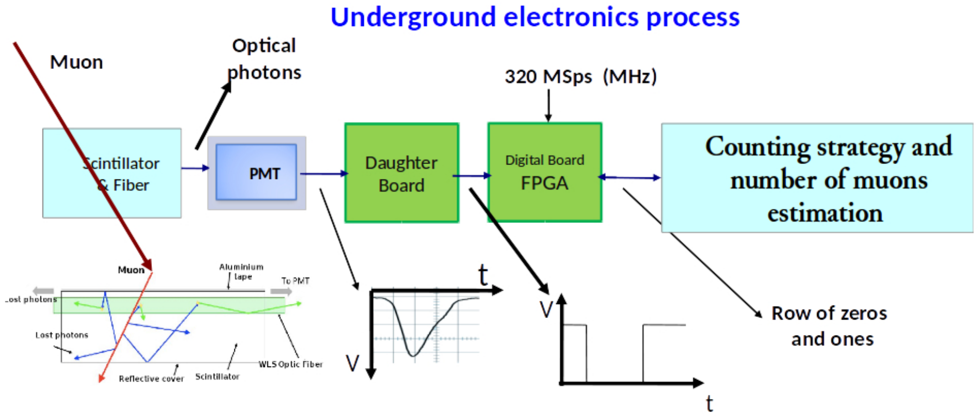

Figure 3.4 Schematic view of the MM electronics. Depicted is the process starting with the impinging particle up to the traces transmitted for the muon-counting proposes.

the signals are discriminated, an FPGA samples the 64 channels at 320 MHz to turn the signals into zero-ones traces of $3.125\,\mu$s length that are stored in a circular buffer waiting for a T3 requirement. A general description of the electronics associated to each module is shown in Figure 3.4.

Additionally, the MM electronics allows for charge integration of the 64-channels detected signals. Integration permits muon measurements close to the core. Moreover, there will be a region where both working modes, integration and counting, would efficiently perform allowing cross-checks and cross-calibrations. A detailed description of the AMIGA electronics can be found in [2].

3.1.3 AMIGA Unitary Cell

As it was mentioned at the beginning of this chapter, MDs must be sensitive only to the muon content of air showers produced by incident cosmic rays. Simulations show that a vertical shielding of $540\,\mathrm{g\,cm^{-2}}$ clearly suffices to reduce the electromagnetic punch-through to a negligible level at core distances of interest. This shielding is equivalent to burying the detectors $\sim 2.25\,\mathrm{m}$ underground (considering the measured average local soil density of $2.38 \pm 0.05\,\mathrm{g\,cm^{-2}}$). This is the final shielding selected for the AMIGA production stage. Nevertheless, in this thesis work, a thinner shielding was also evaluated.

Once the modules are ready, they are transported to the AMIGA site to be deployed in the field. At the present time, AMIGA is finishing the engineering array stage, the Unitary Cell (UC). This UC consists of 7 SD stations on a hexagonal grid deployed with MDs. It includes MMs with different detection areas, $5\,\mathrm{m}^2$ and $10\,\mathrm{m}^2$, both of which have 64 channels

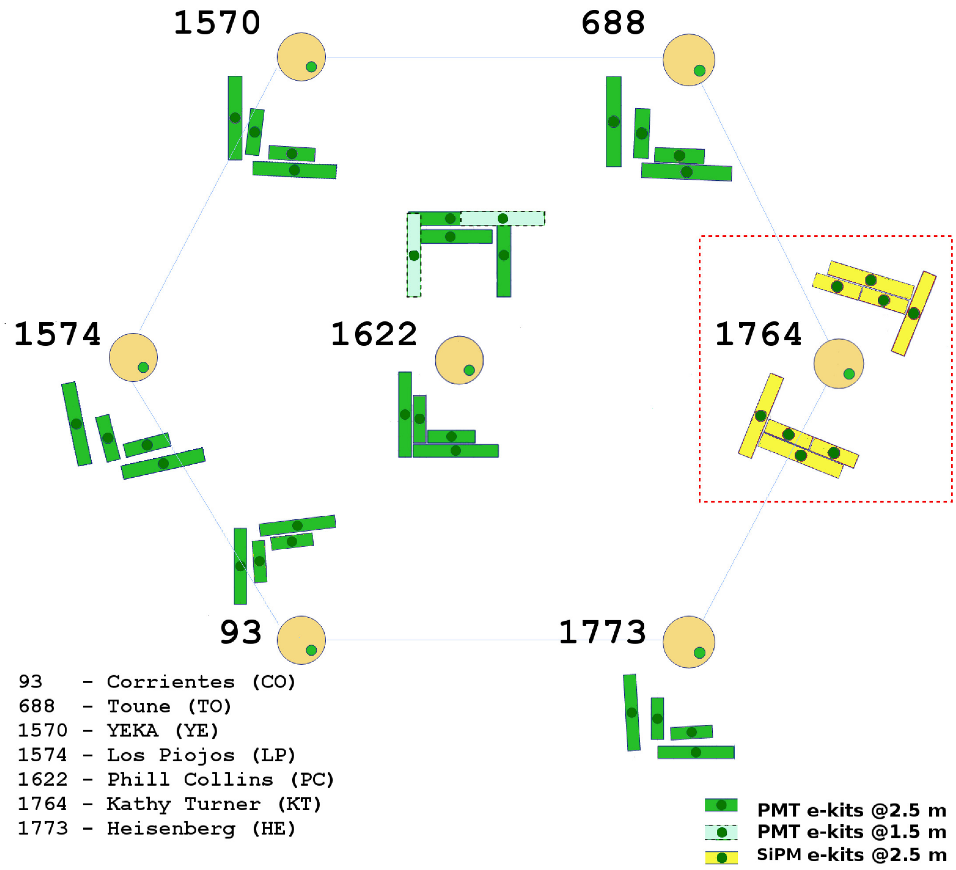

Figure 3.5 AMIGA UC by November 2016.

resulting in a factor of 2 difference in the segmentation area. Four modules, 2 × 5 and 2 × 10 m^2, were deployed at each site of the UC [22] to study the detector performance. The UC has helped in debugging the detector design and understanding the counting uncertainties. Complementary, two positions of the UC have twice the detection area, i.e. 60 m^2 instead of 30 m^2, the so-called twins. Each twin position allows detector performance studies in a reduced period of time.

Additionally, one of the positions has two extra modules deployed at 1.5 m depth to evaluate any punch-through contamination and the possibility of changing the buried-module depth. A map describing the status of the UC by November 2016 is shown in Figure 3.5.

The AMIGA electronics at each position is divided into two parts. The first one is the underground electronics, already described as being associated to each MM. The second one is the surface electronics associated to the MD. This electronics manages the underground electronics, works as an interface with the SD electronics (delivers the T1 trigger of the SD station to each MM and also makes the T3 requirements), and establishes the communication with the CDAS to perform the data transmission. The AMIGA photovoltaic system supplies power to the underground and surface electronics and to the wireless system for data transmission. In one of the twins, Kathy Turner (Figure 3.5, right), the MaPMT opto-electronics system was replaced in November 2016 by the new SiPM system which is currently tested in the field. This new design is described in Section 3.3.

3.2 MDs muon counting

Muon counters are supposed to efficiently count the muonic content of the cosmic ray shower. To ensure this, three correlated steps must be taken into account.

- Select an adequate operation point (calibration procedure).
- Establish a counting strategy (under and over-counting probabilities).
- Evaluate the efficiency.

This procedure is applied to both MaPMT and SiPM opto-electronics systems. The operation point is directly linked to setting the MM HV and its individual 64 pixels thresholds.

The counting strategy encompasses to establish the inhibition window and choosing a minimum FPGA pattern to be identified as a muon. The convolution of fiber and scintillator light yields plus decay times defines the signal structure. The fiber-end opposite to the photomultiplier is painted black and clipped at 45° in order to reduce photon reflections, which may result in delayed SPE detections and thus larger signal time widths. This will augment the inhibition-window time duration during which all arriving signals are considered as coming from the same muon. Therefore pile-up would increase, constraining the use of MDs as counters and reducing the overlap region between its integration and counter modes. For the same purpose of reducing the inhibition window, fast fibers were selected. Laboratory measurements led to set the inhibition window to $\sim 30\,\mathrm{ns}$. Still it is noted that undercounting by pile-up could be statistically corrected up to a given point from the number of bars with signal [16].

The minimum FPGA pattern for the MaPMT is chosen such as to diminish the cross-talk (XT) between pixels which might lead to over-counting. XT has been measured to be less than 1% (per each SPE of the muon pulse) between adjacent pixels and negligible for diagonally neighbouring pixels [3]. XT is essentially removed by selecting signals where at least two non-overlapping SPE pulses are above threshold. This is because the probability of having two cross-talk SPEs in the same neighbouring pixel is negligible. The condition

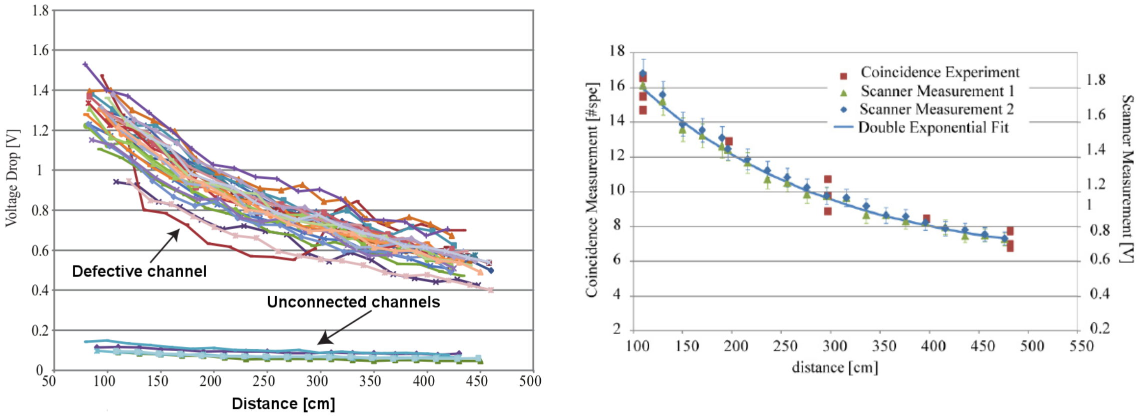

Figure 3.6 MM attenuation curve with a MaPMT. Figure extracted from [43].

of non-overlapping is set since the FPGA might sample a single SPE twice. Currently the counting strategy is being updated to make it more flexible and to include additional timing and adjacency conditions.

The MM efficiency is linked to the number of SPEs per muon. Light attenuation along the fiber translates into higher or lower SPE numbers at closer or farther distances, respectively. This effect can be observed in Figure 3.6 which shows the light-yield curve for different bars in a MM obtained with a radioactive source and measured with a MaPMT. The SPE yield (see Figure 3.6, right) was experimentally measured in a dark box with atmospheric background muons. The curves obtained with the radioactive source are normalized with this measurement. The radioactive source is a 5 mCu radioactive ^{137}Cs source moved by an $x-y$ scanning system designed for AMIGA which permits a quick quality control of all modules before transportation to the Observatory.

MMs with MaPMT opto-electronics was the design selected for AMIGA at the beginning. A new design including SiPMs instead of MaPMTs was developed during this thesis. A join work with engineers ends in a new opto-electronics system described in the next subsection and in FAL Auger Collaboration paper [74].

3.3 Muon counting using Silicon Photomultipliers

A continuous effort has been performed during this thesis work towards upgrading MMs with SiPMs. This work entails the detector calibration and operating point selection to ensure a high-quality performance. Details on this work can be seen in [74]. It is important to

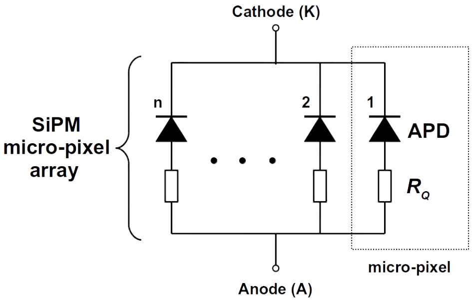

Figure 3.7 Schematic view of the internal structure of a SiPM made up of an array of cells, all connected in parallel. Each cell is composed of an APD working in Geiger mode and a quenching resistor (R_Q) in series.

underline that the AMIGA requirements have been fulfilled and, therefore, for the production phase of AMIGA the current MaPMTs are going to be replaced by SiPMs.

The main motivations for this upgrade are the advantages these devices have compared to current MaPMTs: lower cost per channel, longer life-time, better sturdiness, lower high-voltage, higher photon detection efficiency at the optical fiber emission wavelength, no optical cross-talk between channels, and negligible after pulses. The main disadvantages of SiPMs are its higher noise rate and temperature dependence. This last characteristic was analyzed in detail to ensure an adequate detector performance.

3.3.1 SiPM description

A SiPM [59] is a solid-state device capable of detecting individual photons. It is composed of an array of cells, all connected in parallel. Each cell has an avalanche photo-diode (APD) working in Geiger mode and a quenching resistor (R_Q) in series (see figure 3.7).

The APD starts working in Geiger mode when the reverse voltage (V_{bias}) applied to it exceeds a specific voltage value called the breakdown voltage (V_{BR}). In this mode the injection of a single charge carrier (e.g. due to an impinging photon) causes a self-sustained avalanche. The current that flows through the APD depends on the voltage value over the breakdown which is called overvoltage ($\Delta V = V_{bias} - V_{BR}$). The flow of this current through R_Q produces the decrease of the reverse voltage (V_{APD}) applied to the APD. When V_{APD} is below V_{BR} the avalanche is extinguished. This last sequence describes the “firing” of a cell. From now on, the signal produced by this firing process will be called *Single Photon Equivalent* (SPE). If multiple cells are fired simultaneously the resulting output signal will be a superposition of SPEs. The amplitude of this signal will be directly proportional to the number of fired cells.

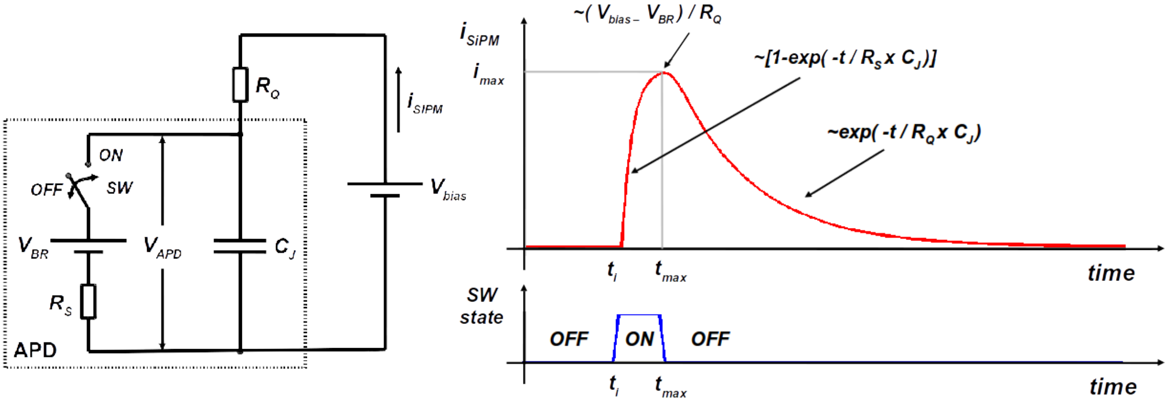

Figure 3.8 Equivalent circuit (left) and time evolution description (right) to explain the firing of a cell. Right, top plot describes the current signal and its characteristic time features. The time evolution of the switch state (SW state) is shown in bottom right figure. Both plots on the right are synchronized in time.

The firing of a cell can be explained with an equivalent circuit (see figure 3.8 left). The initial state of the switch (SW) is OFF. In this state (see figure 3.8 right, bottom), the junction capacitance (C_J) is fully charged to the cathode-anode voltage (V_{bias}) and the current through the APD is zero (see figure 3.8, right, top). When a charge carrier is injected to the depletion region, the avalanche starts. This corresponds to the time (t_i) when the switch changes to the ON state. At that time the current i_{SiPM} rises rapidly, governed by its characteristic time ($R_S \times C_J$). Due to the voltage drop in the R_Q, the applied voltage to the APD decreases. By the time t_{max} V_{APD} is equal to V_{BR}, the avalanche is extinguished. This is represented by changing the switch to the OFF position (see figure 3.8 right, bottom). At this time (t_{max}) the current starts decreasing due to the recharging of the C_J governed by its characteristic time ($R_Q \times C_J$). The total charge produced in the avalanche can be calculated with equation 3.1 and the gain (M) of this process is defined by equation 3.2.

$$Q = C_j \Delta V \tag{3.1}$$

$$M = Q/e \quad \text{where } e \text{ is the electron charge.} \tag{3.2}$$

It can be inferred from equations 3.1 and 3.2 that the gain depends linearly on the overvoltage. Therefore for the special case when the gain is zero, $V_{bias} = V_{BR}$. This equivalence will be important for the calibration procedure.

As was previously mentioned, SiPMs are employed to detect photons. An undesirable effect is the overcounting of those photons due to noise in the cells. In the next subsection, the sources of noise are described in detail.

SiPM Noise

Noise in SiPMs is defined as all the firings of a cell that were not produced by a photon impinging the device. There are three noise sources which can be separated in two types of noise depending on the correlation or not with the firing of a cell.

Uncorrelated Noise: Dark Noise

Dark noise occurs randomly due to the thermally-generated charge carriers (electron-hole pairs) either in the depletion region or in the avalanche region. The amplitude and shape of these pulses are the same as the ones produced by the absorption of a photon. Dark noise is sensitive to the temperature, and also depends on the array of cells size, overvoltage magnitude, and semiconductor material quality.

Correlated Noise: Afterpulsing and Cross-Talk

- Afterpulsing is a secondary avalanche produced after the firing of a cell, due to the release of trapped charges. The release of these trapped charges occurs after a characteristic time that depends on the type of the trapping centers. It is noise correlated to the firing of a cell and it is produced in the same cell.

- When a primary avalanche in a cell produces photons with energy greater than the band gap energy, there is a probability that a nearby cell absorbs the photon, producing its firing. The secondary avalanche is in first order synchronized in time to the main primary avalanche to produce a resulting signal of a channel with an increased amount of SPEs stacked. This effect is called cross-talk.

SiPM Selection

Two main features were taken into account in order to select the specific device to improve the signal-to-noise ratio: high photo-detection efficiency (PDE) and low noise. The PDE of the selected devices is around 35% for the emission wavelength of the fiber optic (485 nm). Low noise is obtained by combining low dark rate with reduced cross-talk and low afterpulsing probability. Three devices manufactured by Hamamatsu (S12572-100C, S12571-100C, S13081-050CS) were tested in the laboratory to evaluate their performance. In Figure 3.9 an overlap of 5000 dark rate traces of each SiPM model is shown. Pulses of more than one SPE, stacked due to cross-talk, can be observed synchronized with the trigger time. Afterpulsing pulses can also be observed many hundreds of nanoseconds after the trigger time.

The three SiPMs exemplified are some of the latest devices developed by Hamamatsu up to 2015. The second SiPM (S12571-100C) in figure 3.9 shows a reduction in the afterpulsing probability compared to the first one (S12572-100C). The third model (S13081-050CS) not

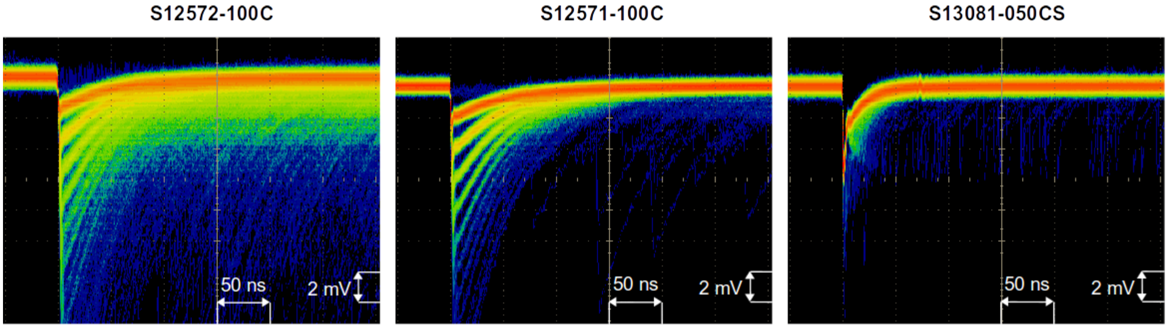

Figure 3.9 Overlap of 5000 dark rate traces (signal amplitude as a function of time) of each SiPM model. All measurements were done with the same amplifier at 25 °C. The ΔV of each SiPM was set to the value recommended by Hamamatsu.

only shows a reduction in the afterpulsing, but also a significantly lower value of cross-talk. This last one was the selected device for this work due to its features and benefits. The main characteristics of these SiPMs, obtained from the Hamamtsu datasheets, are summarized in table **??**.

Parameter		**SiPM Model**			**Unit**
		S12572-100C	S12571-100C	S13081-050CS	
Cell Pitch		100	100	50	μm
Effective Photosensitive Area		3 x 3	1 x 1	1.3 x 1.3	mm
Geometrical Fill Factor		78.5	78	61	%
Photon Detection Efficiency		35	35	35	%
Number of Cells		900	100	667	-
Dark Count	Typ.	1000	100	90	kcps
	Max.	2000	200	360	kcps
Gain M		2.8 x 10^6	2.8 x 10^6	1.5 x 10^6	-
Crosstalk Probability		35	35	1	%

Table 3.1 Main characteristics, obtained from the Hamamatsu datasheets, of the three SiPMs being tested: S12571-100C [28], S12572-100C [29] and S13081-050CS [30].

After several tests and laboratory measurements, the selected SiPM was the S13081-050CS [30] due to its low cell crosstalk and afterpulsing. The CITIROC ASIC was selected [46] as the electronics front-end and the Hamamatsu C11204-01 power supply [27] was chosen for biasing the SiPMs.

3.3.2 Calibration Method of the Counting System

A new calibration method for these new devices was adopted. It consists of two steps (see [74]). The first step consists in calibrating the optical sensors to set the operation point of each individual channel (see subsection 3.3.2). The second step consists in calibrating the detector (see subsection 3.3.2) by setting the threshold value of the discriminators and establishing a counting strategy.

- **SiPM Calibration.** This is the first step of the calibration needed in the counting system. The goal is to set the operation point of the SiPMs. First, the breakdown voltage of each individual channel must be obtained. Then, all the SiPMs must be biased to its corresponding breakdown voltage with an added pre-determined overvoltage. This overvoltage can be changed to optimize the efficiency. In [74] a method for obtaining the breakdown voltage and biasing of the SiPMs with the proposed AMIGA electronics is explained. This method is based on the measurement of the rate over threshold curve.
- **Detector Calibration.** Once the SiPM is calibrated, the next step consists of determining the discrimination level and the counting strategy (detector calibration), ensuring an adequate performance of the counting system. The proposed counting strategy for the SiPMs is based on an amplitude criteria. The high PDE ($\sim$35 %) of these devices at the emission wavelength of the WLS optical fiber allows setting a threshold of a small number of SPEs to discriminate particles from noise, with a reduced losing particle detection efficiency. The discrimination level is set at the lowest value that ensures a low rate of contamination (negligible accidental counting) and also does not damage the counting efficiency.

Both calibrations combined guarantee the performance of the detector by an adequate overvoltage and threshold levels selection. The counting strategy is simpler, since a muon is consider as any signal detected in a window of 11 bins. The width of the window was decided as a result of the laboratory measurements performed for different fiber distances of the impinging particle. Both steps are designed to be performed at the Observatory site thus guaranteeing a long-term performance of the detector, improving its stability for long periods.

In the following subsections, a description of the new calibration method for the new devices is included.

SiPM Calibration

This is the first step of the calibration needed in the counting system. The goal is to set the operation point of the SiPMs. First, the breakdown voltage of each individual channel must be obtained. Then, all the SiPMs must be biased to its corresponding breakdown voltage

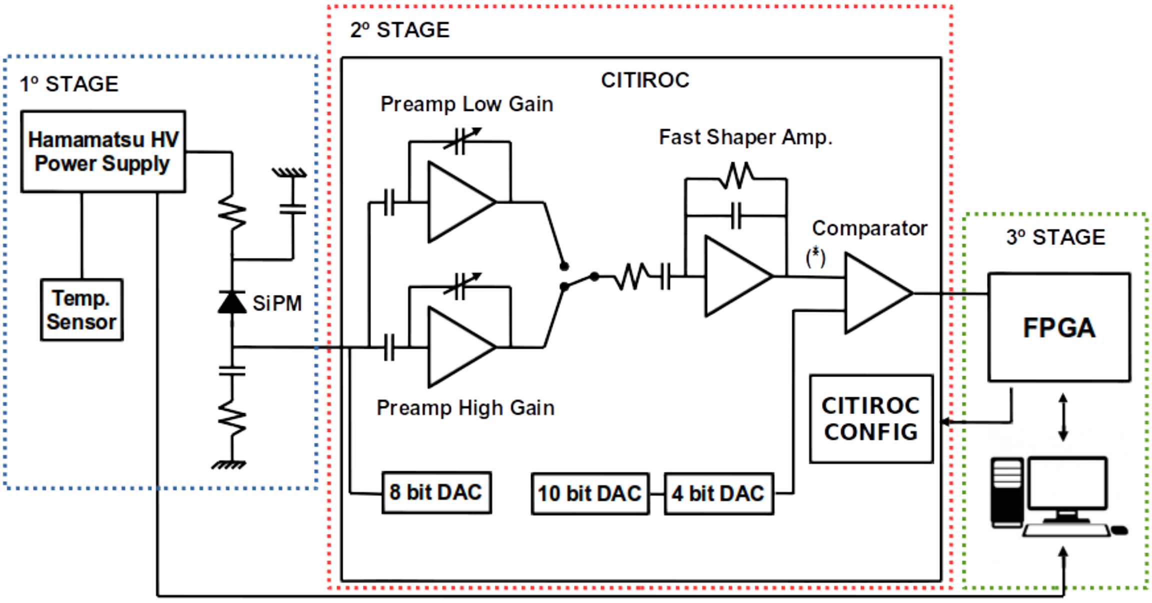

Figure 3.10 SiPM Calibration Setup. The three stages are distinguished with dotted lines. The output of the fast shaper amplifier $(*)$ has a DC offset component.

with an added pre-determined overvoltage. This overvoltage can be changed to optimize the efficiency. In this section a method for obtaining the breakdown voltage and biasing of the SiPMs with the proposed AMIGA electronics is explained.

SiPM Calibration Setup

The setup for the SiPMs calibration is divided into three stages (see figure 3.10). The first stage is composed of the SiPM, the high voltage power supply and the temperature sensor. Since the SiPM breakdown voltage varies significantly with temperature, the high voltage power supply has a built-in high precision temperature compensation system that constantly corrects the SiPM operation point. This function tries to keep the gain value fixed independently of temperature variations. The compensation of the high voltage (HV) output is determined by the equation 3.3 (given by Hamamatsu). In this formula, the $\Delta T'$ and ΔT are respectively the quadratic and linear temperature coefficients for the compensation, and V_b is the reference voltage. For the SiPMs under test $\Delta T'$ was set to 0 mV/°C^2, ΔT to 54 mV/°C and the reference temperature (T_b) to 25 °C. The resulting formula for the calibration is described in equation 3.4.

The second stage consists of the CITIROC. This stage amplifies and then discriminates SiPM pulses. The chip was programmed to use the high gain pre-amplifier, with its maximum gain of 10, to improve the separation between SPEs in the SPE spectrum. The 8-bit DAC input

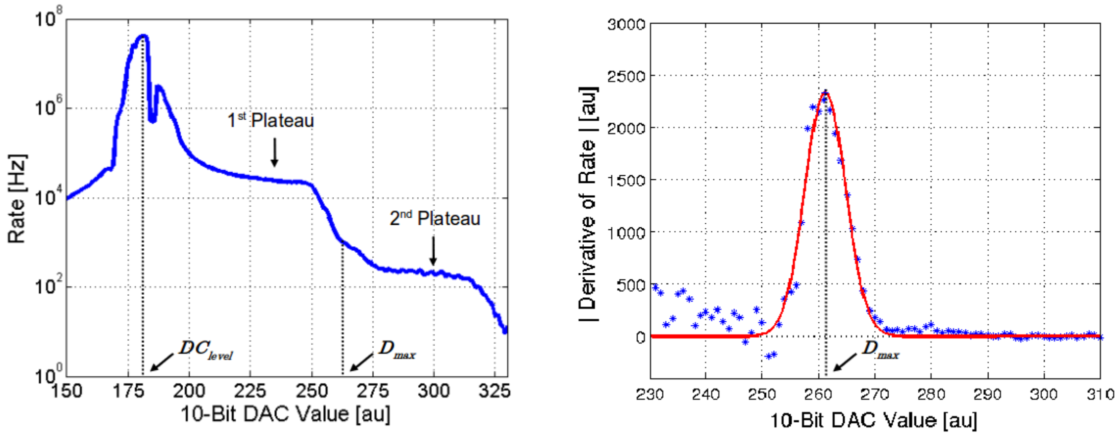

Figure 3.11 On the left, the measurement of the rate of the SiPM pulses as a function of the DAC value. DC_{level} corresponds to the fast shaper DC offset component. See subsection 3.3.2 for details on the setup. On the right, the absolute value of the derivative of the rate evidences the mean value of the peak (D_{max}), obtained with a Gaussian fit of the points (red curve).

was set to a fixed value (e.g. 250 dac-units). The 10-bit DAC was used to set the comparator threshold for all the channels and the 4-bit DAC of each channel was fixed to its minimum value.

$$HV = \Delta T' * (T - T_b)^2 + \Delta T * (T - T_b) + V_b \tag{3.3}$$

$$HV = 54\ mV/^{\circ}C * (T - 25\ ^{\circ}C) + V_b \tag{3.4}$$

The third stage is composed of a FPGA. The FPGA was programmed to measure the rate of the CITIROC digital pulses output.

Single Photo-Electron Peak Measurement

To be able to perform the calibration proposed in this subsection, a difference in the rate value of one SPE and two SPEs is needed. A dedicated software was developed to automatically measure the rate of the digital pulses at different discrimination levels. In the measurement of the SiPM noise rate as a function of the 10-bit DAC values (see figure 3.11, left) there is a clear transition from the first to the second plateau. This transition represents the threshold of the comparator passing through the first SPE peak.

The absolute value of the derivative of this curve (see figure 3.11, right) represents the distribution of the SPE peak values. The mean value of the SPE peak (D_{max}) is correlated to the maximum absolute value of the Gaussian distribution coming from the derivative of the rate curve. This value has an offset (DC_{level}) because the signal in the fast shaper has a

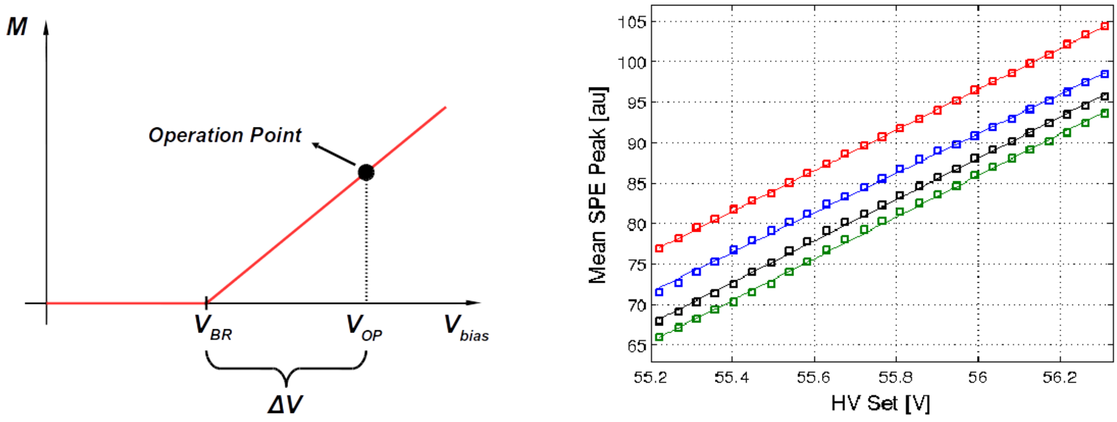

Figure 3.12 The plot on the left summarizes equations 3.1 and 3.2. The mean SPE_{peak} as a function of the HV value for four different SiPMs is plotted on the right. The mean SPE_{peak} is proportional to M, and HV Set represents the V_{bias}.

DC offset component (see figure 3.10). The value of this DC offset is the DAC value where the rate is maximum (see figure 3.11, left). To obtain the real value of the SPE peak it is necessary to subtract this offset (see equation 3.5).

$$SPE_{peak} = D_{max} - DC_{level} \tag{3.5}$$

As was mentioned before, the employment of these devices (SiPMs) combined with the method explained in this subsection, allow the SPE_{peak} estimation which is used to calculate the breakdown voltage of the device, as will be explained in the next subsection.

Breakdown Voltage Measurements

There are several methods to estimate the breakdown voltage of a SiPM (i.e. by gain, current, PDE). Due to the constrain of the proposed electronics, the method to estimate each channel breakdown voltage is the one described in this subsection.

Equations 3.1 and 3.2 are summarized in figure 3.12, left. This figure shows that if the gain (M) is measured over the V_{bias}, the breakdown voltage can be obtained as the value where the curve intercepts the X axis ($V_{bias} = V_{BR}$). It is also known that the SPE_{peak} is directly proportional to the gain (Mean $SPE_{peak} \propto$ M). By using this information and following the procedure explained in the previous subsection, a plot of SPE_{peak} for different V_{bias} values, can be obtained. From that plot, the V_{BR} is estimated as the point where the linear fit of the curve (figure 3.12, right) intercepts the X axis ($HV\ set \equiv V_{bias} = V_{BR}$). An example for four different SiPMs is shown in figure 3.12, right.

To automatize the breakdown voltage estimation, the 8-bit DAC input of the CITIROC (see figure 3.10) was fixed to 250 dac-units for all the channels and the HV value was changed (V_{bias} changes following the power supply HV). With this method, it is possible to calculate each SiPM characteristic breakdown voltage at the same time, with a single power supply. This is the case with the electronics that will be deployed. In the following subsection a possible equalization of SiPMs overvoltage is explained following this constraint.

Equalization Between Channels

As was mentioned before, the ΔV applied to each device is the only parameter that can be changed to modify the characteristics of the SiPM behaviour, for a fixed temperature. Therefore, it is desirable for all the SiPMs in the detector to have the same ΔV applied. The equalization consists in applying the same ΔV to all the channels. This equalization does not ensure the same gain or rate at a given threshold between channels.

Since the designed electronics has only one power supply and considering that the SiPMs have different V_{BR}, in order to set the desired operation voltage (V_{OP}) for each SiPM individually, the following procedure is carried out:

1. Set the HV voltage of the power supply to the largest V_{BR} of the 64 SiPMs with the desired ΔV added (see equation 3.6).
2. Change the voltage setting individually by the 8-bit DAC input of the CITIROC ($V_{8bitDAC}$) for each SiPM (i). Combining equations 3.6 and 3.7, equation 3.8 can be obtained. In this last equation, the $V_{8bitDAC}$ value that must be set is shown.

$$HV = V_{BR_{max}} + \Delta V \tag{3.6}$$

$$HV - V_{8bitDAC_i} = V_{BR_i} + \Delta V = V_{OP_i} \tag{3.7}$$

$$V_{8bitDAC_i} = V_{BR_{max}} - V_{BR_i} \tag{3.8}$$

An example of this equalization for four channels can be observed in figure 3.13.

Detector Calibration

Once the SiPM is calibrated, the next step consists of determining the discrimination level and the counting strategy (detector calibration), ensuring an adequate performance of the counting system.

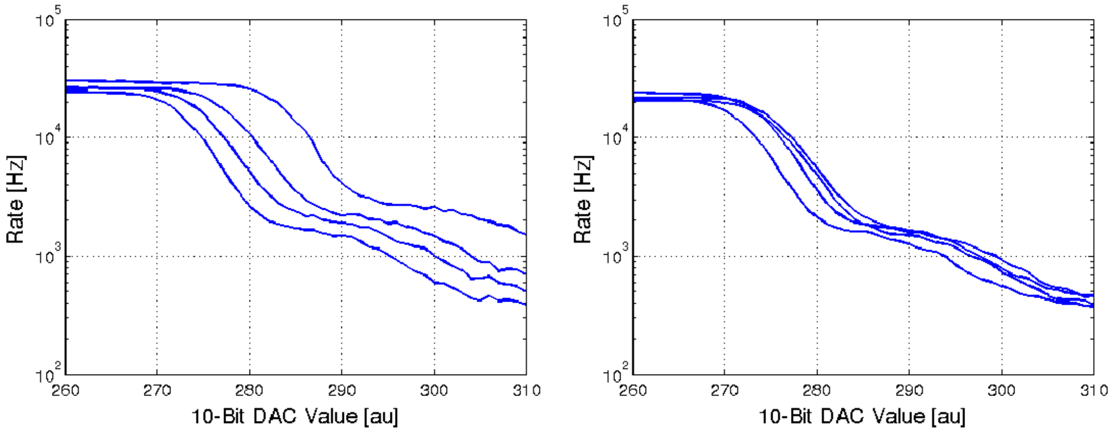

Figure 3.13 The rate of the SiPM pulses as a function of the 10-bit DAC value for four channels that are not equalized is shown in the left plot. The same four channels after the equalization process are shown in the right plot. After the equalization process all the channels are operating with the same ΔV.

Detector Calibration Setup

The setup for the detector calibration is divided into six stages (see figure 3.14). The first stage is the same as the first stage described in the subsection 3.3.2. The second stage is composed of the stages two and three described in the subsection 3.3.2. For this calibration, the CITIROC was programmed to use the high gain pre-amplifier, with its minimum gain of 1, to reduce the digital time span of the discriminated pulses. The 4-bit DAC was fixed to its minimum value and the 8-bit DAC input was set following the procedure detailed in the subsection 3.3.2 (equalization). The 10-bit DAC is used to set different discrimination levels. The third stage is an amplifier to allow the measurement of the analog signal of the SiPM. The fourth stage consists of a 4 m plastic scintillation bar with a 5 m wavelength-shifting optical fiber threaded. At the end of the optical fiber there is an optical connector coupled to the SiPM. The fifth stage is a muon telescope trigger [43] that ensures the acquisition occurs every time a particle passes through each position of the scintillator where the telescope is placed. The sixth stage is the acquisition system. This stage is composed of a Tektronix DPO7104 oscilloscope. This oscilloscope is set up to store the discriminated signal of the CITIROC (stage 2) and the amplified analog signal of the SiPM (stage 3) every time the muon telescope produces a coincidence in a time window of 60 ns (stage 5).

Selection of the Counting Strategy

As was described in [71] the current counting system (PMT and electronics) is conceived to count muons by identifying a pattern in the digital trace. The discrimination level is set at a

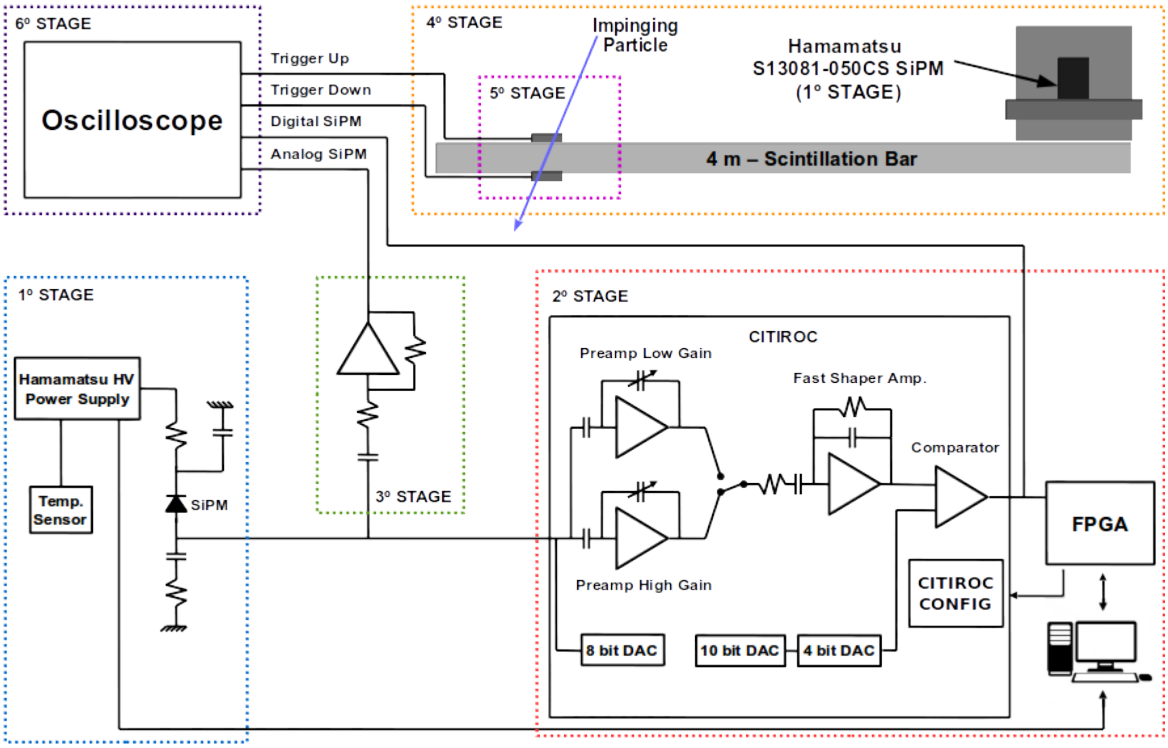

Figure 3.14 The six stages of the setup needed for the detector calibration.

value lower than one SPE and then a pattern recognition technique is applied to discriminate particles from noise. This counting strategy takes into account the time structure of the signal over a threshold.

The proposed counting strategy for the SiPMs is based on an amplitude criteria. The high PDE (∼35 %) of these devices at the emission wavelength of the WLS optical fiber allows setting a threshold of a small number of SPEs to discriminate particles from noise, without losing particle detection efficiency.

The discrimination level is set at the lowest value that ensures a low rate of contamination (negligible overcounting) and also does not damage the counting efficiency. In figure 3.15, the rate of SiPM pulses as a function of the 10-bit DAC threshold is shown. Two cases are plotted: in red the rate when the fiber is coupled to the SiPM, and in blue when it is not. When the fiber is not coupled to the SiPM, only the noise from the SiPM is measured. When the fiber is coupled to the SiPM, not only the dark rate is measured, but also all the signals produced by charged particles impinging the scintillator. These particles will be considered as the environmental radiation. In figure 3.15, for one and two SPE rate levels, the correlated and the uncorrelated noises, explained in section 3.3.1, dominate. If the threshold level is set in any of these values, the overcounting probability for the whole detector (64 channels) is over the desired limit level of 5%. At three SPE rate level, the environmental radiation starts

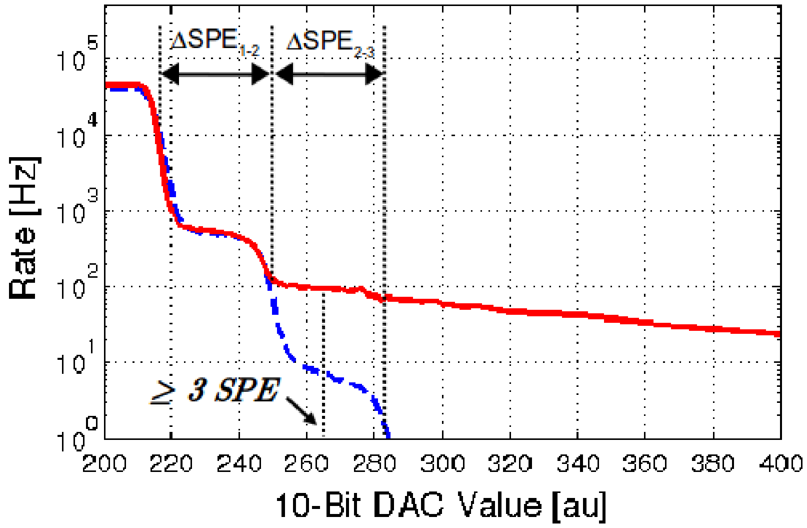

Figure 3.15 Measurement of the SiPM pulses rate with (red complete line) and without (blue dashed line) the scintillating bar over the 10-bit DAC value. Each plateau represents the transition for different amounts of SPEs. The value marked with the $\geqslant 3\ SPE$ is the selected value for the threshold of the discriminator.

to dominate over the noise. For this level, the overcounting probability (see equation 3.10) is mainly due to the environmental radiation and fulfils the requirement, therefore this is the selected level for the threshold.

As it was mentioned in subsection 3.3.2, the transition between plateaus in the SiPM rate as a function of the 10-bit DAC value represents the threshold of the comparator passing through the SPE peaks. Furthermore, as was mentioned in section **??**, the amplitude of the signal generated by multiple simultaneously fired cells is directly proportional to the number of them. Therefore, it is expected that: $\Delta SPE_{1-2} = \Delta SPE_{2-3} = SPE_{peak}$ (see figure 3.15). In the example shown, the obtained values were: $\Delta SPE_{1-2} = (32 \pm 2)$; $\Delta SPE_{2-3} = (36 \pm 2)$; $SPE_{peak} = (34 \pm 2)$. Taking into account the uncertainties in the measurement, they are all compatible.

The middle point of the transition between the two and three SPE peaks ($SPE_{peak} * 2.5$) corresponds to the value that ensures the detection of signals with three or more SPEs. Considering the offset (DC_{level}), this value can be calculated with equation 3.9.

$$3SPE_{level} = SPE_{peak} * 2.5 + DC_{level} \simeq (34 \pm 2) * 2.5 + (182 \pm 1) = 267 \pm 6 \qquad (3.9)$$

As an example, in the case exemplified in figure 3.15 the estimated SPE_{peak} was (34 ± 2) and the DC_{level} was (182 ± 1). The calculated $3SPE_{level}$ is marked in the figure as $\geqslant 3\ SPE$. It can also be seen in the figure that the calculated value corresponds to the middle point of the third SPE plateau. The $3SPE_{level}$ must be estimated and set individually for each channel.

$$P_{overcount} = n \cdot T_{event} \cdot R_{noise} \simeq 64 \cdot 3.2\ \mu s \cdot 100\ Hz \equiv 2.05\ \% \tag{3.10}$$

To estimate the overcounting probability ($P_{overcount}$) three factors are taken into account: the segmentation (n), the acquired event time window (T_{event}) and the noise rate (R_{noise}, i.e. the environmental radiation and dark rate). As an example, for the AMIGA modules the segmentation is of 64 channels, the acquired event time window is 3.2 μs and the noise rate in the laboratory is ~100 Hz (this value is highlighted in figure 3.15). The efficiency will be studied in detail in section 3.3.4.

3.3.3 Proposed On-site Calibration

As was mentioned before, the electronics design enables calibration to be performed at the observatory site. To ensure their long-term performance, both calibrations detailed in sections 3.3.2 and 3.3.2 will be applied regularly and automatically. Each module will acquire the data locally and then send it to a dedicated calibration server that will be running in the Central Data Acquisition System (CDAS) of the Pierre Auger Observatory. This calibration server will carry out the SiPM Calibration as well as the Detector Calibration. This dedicated server will do the calculations to set three groups of parameters: the HV value, the 8-bit DAC input to equalize the channels, and the 10-bit DAC value to set the discrimination level. All the calibration data and the parameters obtained will be stored for long-term stability studies.

3.3.4 Efficiency Measurements

The module must count efficiently the number of impinging muons. To test its efficiency, the setup described in subsection 3.3.2 was used. Several measurements at different fiber lengths were taken using the muon telescope. Every time there is a muon telescope trigger (event), the acquisition system (see sixth stage of section 3.3.2) stores the discriminated signal of the CITIROC (digital trace) and the amplified analog signal of the SiPM (analog trace).

From the amplified analog traces, the voltage amplitude peak and charge (integral of the current) of each pulse were obtained by an offline analysis. The charge was numerically calculated integrating the voltage signal trace, in a time window of 200 ns, divided by the oscilloscope input impedance value (50 Ω). A histogram illustrating the voltage amplitude peak and charge of the analog traces obtained at a fiber distance of 430 cm with the S13081-050CS SiPM is shown in figure 3.16. Two colored areas can be distinguished in each

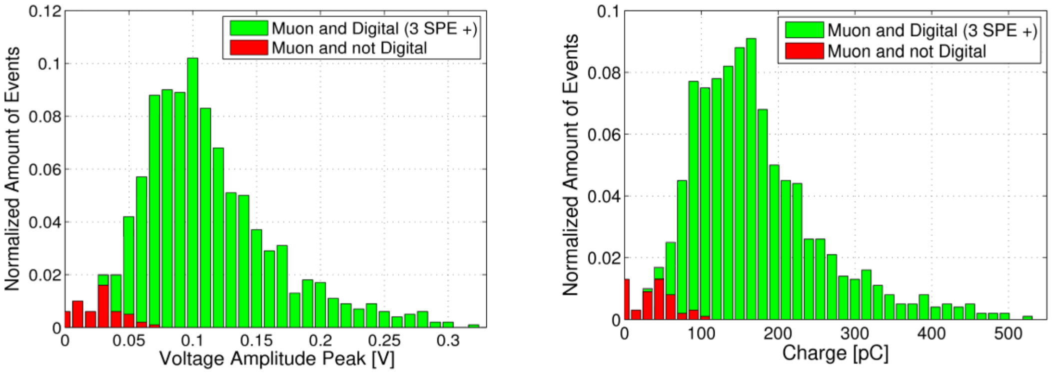

Figure 3.16 In the left (right) plot, the voltage amplitude peak (charge) histogram of 1000 triggered muon events is shown. The red colored area corresponds to the events that do not have a positive digital trace. All the measurements were done at 25 °C, $\Delta V = 3.75\,V$, and with the muon telescope placed at 430 cm of fiber from the SiPM.

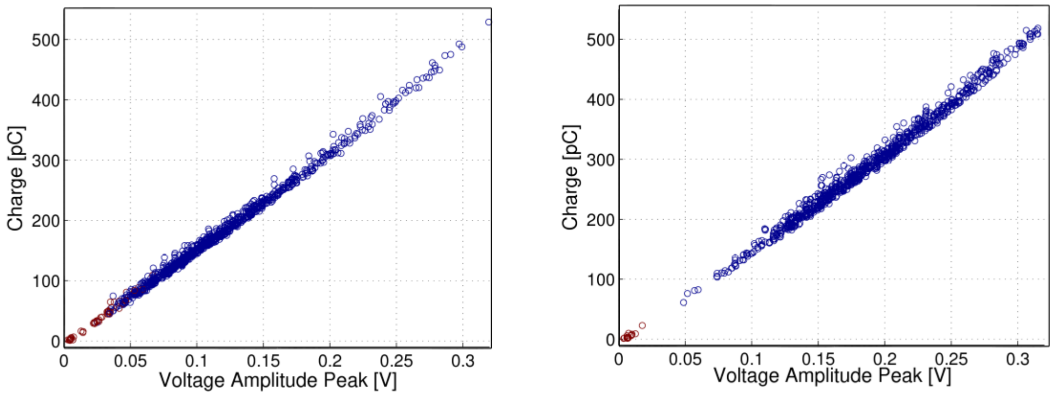

Figure 3.17 Both plots show the relationship between the voltage amplitude peak and the charge of 1000 triggered muon events. The red colored points correspond to events that do not have a digital output. In the left (right) plot the muon telescope was placed at 430 cm (130 cm) of fiber. Isolated red points in the lower left corner in the right figure evidence the false coincidences of the muon telescope trigger. All the measurements were done at 25 °C and $\Delta V = 3.75\,V$.

histogram. The red area represents the events that do not have a corresponding positive digital trace of the CITIROC. This means that no particle was detected by the counting system. The green area represents all the events that have a positive digital trace.

Both plots in figure 3.17 show a correlation between the voltage amplitude peak and charge of SiPM signals. In these plots there is a discrimination between the traces with (blue) or without (red) digital output. In the left plot, the results with the muon telescope placed at 430 cm of fiber are shown, and in the right one, the muon telescope was moved to 130 cm.

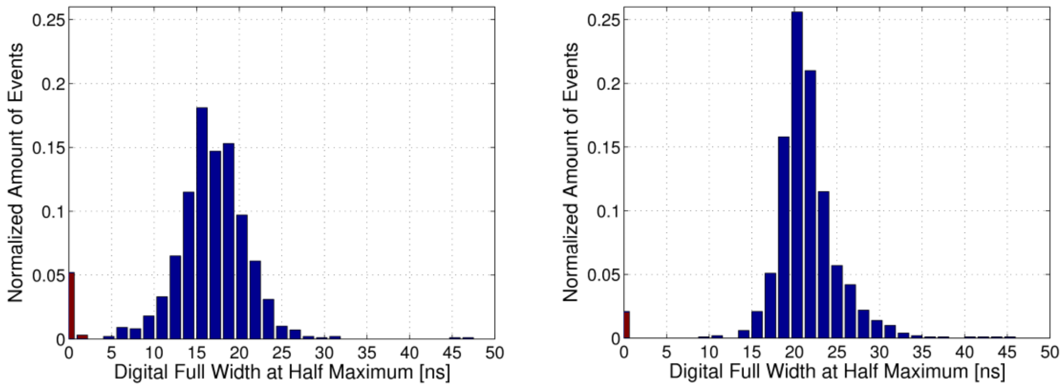

Figure 3.18 Both plots show the width histogram of 1000 digital output pulses of the CITIROC. The red colored bar corresponds to the traces that do not have a digital output pulse. In the left (right) plot the muon telescope was placed at 430 cm (130 cm) of fiber. All the measurements were done at 25 °C and $\Delta V = 3.75\,V$.

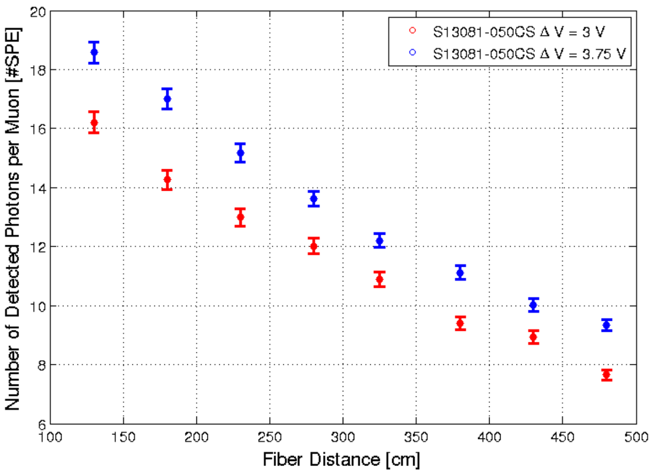

Figure 3.19 Number of detected photons per muon impinging the detector as a function of the fiber distance for two different overvoltages: $\Delta V = 3\,V$ and $\Delta V = 3.75\,V$. The detector light yield is not uniform due to the fiber attenuation. Error bars are only due to statistic errors of the mean. All the measurements were done at 25 °C.

As expected, the data sets have higher mean voltage amplitude and charge values due to a decrease in the light attenuation of the fiber.

In figure 3.18, the full width at half maximum (FWHM) of the digital output pulse of the CITIROC, acquired with the oscilloscope at two fiber distances measured is shown. As it was pointed out in the requirements, 99 % of the digital widths are lower than 35 ns. This requirement was achieved by the fast shaper included in the CITIROC. There was no evidence of afterpulses in the observed digital output.

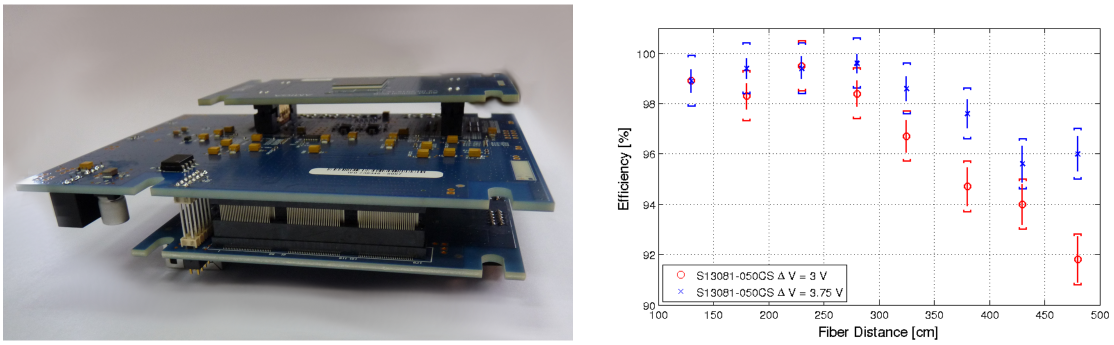

Figure 3.20 Right: The new electronics including the selected SiPM array on top. Left: Efficiency measurements for two different ΔV are compared. A larger ΔV produces an efficiency increase. The estimated integrated efficiency is: 96 % for $\Delta V = 3\,V$ (red) and 97 % for $\Delta V = 3.75\,V$ (blue). Extracted from [74].

In figure 3.19, the mean value of the number of detected photons per muon impinging the detector as a function of the fiber distance is shown. This mean value was obtained as the mean value of the distribution of the rate between the charge of measured traces and the mean charge of the SPE. Error bars are only due to statistic errors of the mean. This light yield curve was obtained with the setup shown in Figure 3.14. The muon telescope trigger selects mainly vertical muons and the acceptance angle considering the muon telescope geometry is $\sim 35^\circ$. There are two main factors that constrain the performance of the detector since its light yield is not uniform due to the fiber attenuation. In the farther distances, the efficiency strongly depends on the threshold selection, since the attenuation of the optical fiber significantly decreases the number of photons that arrive to the SiPM. At the closest distances, the number of detected photons is higher and the digital width is consequently increased. The selected pre-amplifier gain, i.e. high-gain pre-amplifier set to the lowest gain, combined with the fast shaper ensures an adequate width of the digital output.

A photograph of the new electronics AMIGA with the selected SiPM array is shown in Figure 3.20, left.

Laboratory efficiency studies show promising results (see Figure 3.20, right). The high integrated efficiency obtained (97 %) combined with a low probability of accidental counting (∼2 %) evidences an adequate performance of the proposed counting system.

3.3.5 A Unitary Cell calibrated event

Since November 2016, the AMIGA Unitary Cell is acquiring new data with its seven detector positions calibrated. Six of them have MaPMT and a twin position has SiPMs. An event was selected to show the new calibrated detectors.

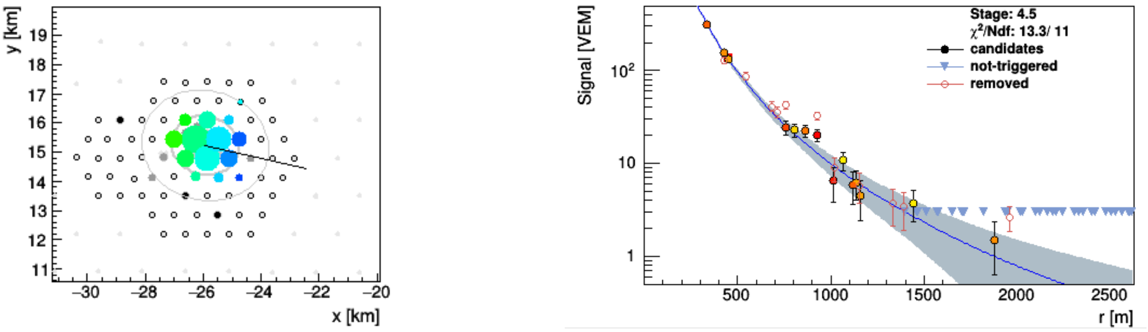

Figure 3.21 The SD trigger map (left) and the LDF reconstruction (right).

The selected event was detected on th 8th of November 2016 by both SDs and the AMIGA UC MDs. The main SD parameters are summarized in Table 3.2 and Figure 3.21.

SD Reconstructed Parameters	
Parameter	Value
Energy	$(1.69 \pm 0.06 \pm 0.03)\ 10^{18}\ eV$
(θ,ϕ)	$(31.5 \pm 0.3,\ 347.3 \pm 0.5)\ deg$
(x,y) Core	$(-25.93 \pm 0.01,\ 15.23 \pm 0.01\ )\ km$
S_{450}	$(134.4 \pm 4.6(\pm 2.1))\ VEM$

Table 3.2 Main parameters obtained through SD reconstruction.

From the point of view of the MD, four stations were used in the reconstruction: Kathy Turner (ID: 1764, KT), Phil Collins (ID: 1622, PC), Toune (ID: 688, Toune), and Heisenberg (ID:1773, HE) . Corrientes(ID: 93, Co), Yeka (ID: 1570, YEKA) and Los Piojos (ID: 1574, LP) were too far away and did not have detected muons. The interesting feature of this event is that stations with MaPMT and SiPM MMs detected the shower, since the shower core was close to Kathy Turner (1764) position. By normalizing the number of muons by the effective scintillating area in each position (some modules and some individual channels were out of acquisition) and using the geometrical reconstruction from the SD, the muon density (ρ_μ) at each distance to the core axis in the shower plane (r) can be obtained. The core distance (in the shower plane) of each station is calculated from the SD geometrical reconstruction: KT 337 m, HE 760 m, PC 929 m, and Toune 1015 m.

An example of two MMs with SiPM raw data is included. There is a significantly higher amount of muons in the 107 (Figure 3.22, 10 m^2) compared to the 106 (Figure 3.23, 5 m^2) module.

The applied counting strategy is different for the different detectors. In the case of the MMs with PMT the counting strategy applied is the one described in [20] and in the case of the MMs with SiPM is the one described in [74]. The resulting number of counted muons

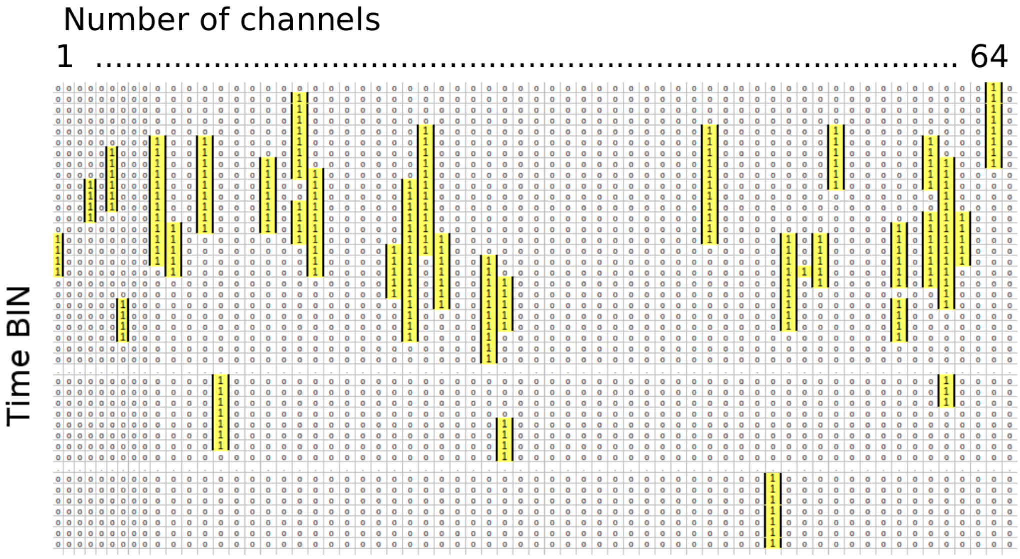

Figure 3.22 AMIGA 10 m^2 MM with SiPMs.

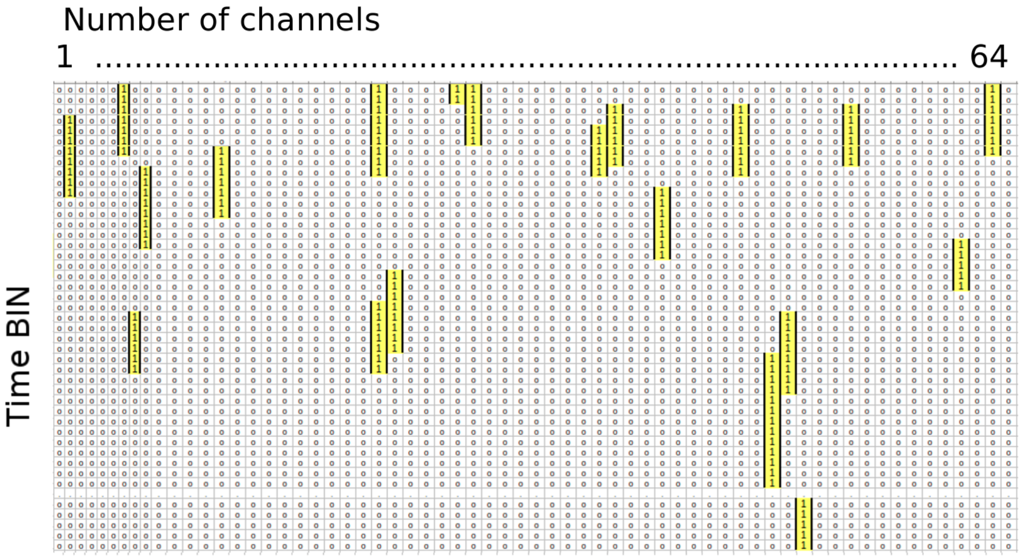

Figure 3.23 AMIGA 5 m^2 MM with SiPMs.

(without corrections due to pile-up effects) for each position is detailed in Figure 3.24, left. The detection area was corrected subtracting not-working channels or modules. The obtained densities are in concordance with the values expected for the stations radial distances and the measured shower energy. Furthermore, the density measured by all 10 m^2 MMs is 3.81 μ/m^2

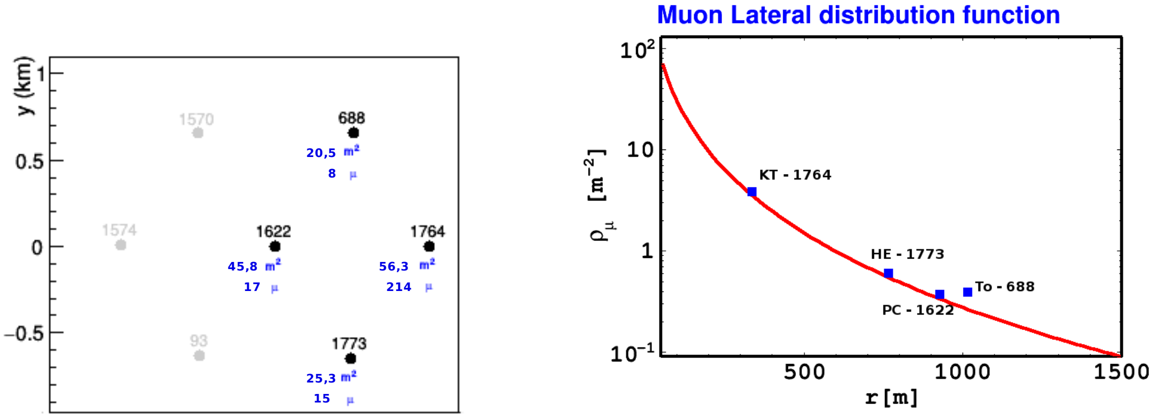

Figure 3.24 The MD trigger map [left]. The MLDF reconstructed combining stations with SiPM (KT) and with MaPMT (PC,To,HE).[right]

and the measured density of all the 5 m^2 MMs is 3.78 μ/m^2. This is not a full analyzed detector behavior result, but it is very promising.

The main MD parameters are summarized in Table 3.3 and Figure 3.24.

A *Kascade Grande* type LDF [60] is used to reconstruct the muon lateral distribution function. It has two possible free parameters $\rho_\mu(450)$ and β, density at 450 m from the core and LDF slope, respectively.

$$\rho_\mu(r) = \mathrm{K} \times \rho_\mu(450) \times \left(\frac{r}{R_0}\right)^{-\alpha} \times \left(1+\frac{r}{R_0}\right)^{-\beta} \times \left(1+\frac{(0.1r)^2}{R_0^2}\right)^{-\gamma} \tag{3.11}$$

The other three parameters (i.e. α, γ and R_0) are chosen and fixed from standard reconstruction values. Therefore they will differ from those of Kascade-Grande [36, 60]. The distance at which the density is evaluated (450 m) is the optimal distance for this detector array, i.e. where fluctuations and uncertainties are minimized.

MLDF Reconstructed Parameters	
Parameter	Value
$\rho_\mu(450)$	$(2.63 \pm 0.15)\ \mu/m^2$

MLDF Fixed Parameters	
Parameter	Value
β	1.04
α	1
γ	1.85
R_0	150
r_{opt}	450

Table 3.3 Parameters obtained from an Kascade-Grande MLDF reconstruction of the real event. Only statistic uncertainties are shown for $\rho_\mu(450)$. β is fixed to the standard reconstruction value.

3.4 Conclusions of the chapter

AMIGA (Auger Muons and Infill for the Ground Array) is an upgrade of the Pierre Auger Observatory designed to extend its energy range of detection and to directly measure the muon content of the cosmic ray primary particle showers. The array is formed by an infill of surface water-Cherenkov detectors associated with buried scintillation counters employed for muon counting. For production, each counter is planed to be composed of three scintillation modules, with a $10\,m^2$ detection area per module.

Currently a Unitary Cell is already deployed and acquiring data. The design of the UC muon counters has been shown to function successfully within expectations working with an opto-electronics system based on 64 pixel PMT for each module. First longitudinal and lateral muon profiles have been reconstructed and are currently under further analysis. The stable and quality performance of the AMIGA muon counters is reflected in the analysis of events recorded thus far.

During the last years a new generation of detectors, replacing the current multi-pixel photomultiplier tube (PMT) with silicon photo sensors (aka. SiPMs), was proposed. During this thesis a new opto-electronics system was proposed and a new calibration method tested (see [74]. The selected SiPM was the S13081-050CS due to its low crosstalk and afterpulsing. The CITIROC ASIC was selected as the electronics front-end. Its fast shaper enables a digital output width of the discriminator similar to the characteristic time width of the light pulses produced by the impinging particles in the detector. The Hamamatsu C11204-01 power supply was chosen for the biasing of the SiPMs. The selection of the new device and its front-end electronics was based on the previous PMT design. A method to calibrate the counting system that ensures the performance of the detector was achieved. This method has the advantage of being able to be carried out in a remote place such as the one where the detectors are deployed.

High efficiency results, i.e. 98 % efficiency for the highest tested overvoltage, combined with a low probability of accidental counting ($\sim 2\%$), show a promising performance for this new system.

Kathy Turner position has eight modules acquiring calibrated data since December 2016. Preliminary results related to detector performance and twin data analysis are promising. A full author list Pierre Auger Collaboration paper was the result of this work [74]. The complete Unitary Cell working with SiPM is planning to be full operating by the beginning of 2018.

Chapter 4

Tri-hybrid simulation and reconstruction of an UHECR event

The Pierre Auger Observatory was planned to study atmospheric showers produced by high-energy cosmic-ray primaries. Its hybrid technique combines surface water Cherenkov detectors and fluorescence detectors to study the atmospheric shower development with a high resolution and reduced systematic uncertainties. The introduction of a new detector, AMIGA (see Chapter 3), improves the Observatory's capabilities to accomplish hybrid composition analyses by a direct measurement of the shower muon component.

AMIGA buried scintillators are now stably acquiring data in seven positions (an hexagon and its central station). A high energy event ($\sim 10EeV$) was registered in 2013 by the AMIGA Pre-Unitary Cell (same 7 current positions but $\sim 1/3$detector area), the highest energy event detected by AMIGA yet and moreover, the detection was hybrid. A detailed study of this event offers experimental evidence of the impact MD may give with their $\sim 100\%$ duty cycle. This information will be further enhanced when the arrival time of each individual muon is incorporated in the analysis.

The *Muon Lateral Distribution Function* (MLDF) at the underground level (2.3 m soil shielding) was studied and tested with a real detected shower.

The first section of this Chapter, Section 4.1, includes the detected event reconstruction with three Auger detector system: Surface (SD), Fluorescence (FD), and Muon (MD) detectors. The geometry and energy obtained from SD and FD are used to simulate showers for two primaries (proton and iron) and two hadronic models (QGSJetII-04 and EPOS-LHC), see Section 4.2. These simulated events are reconstructed and the results are compared with the detected event.

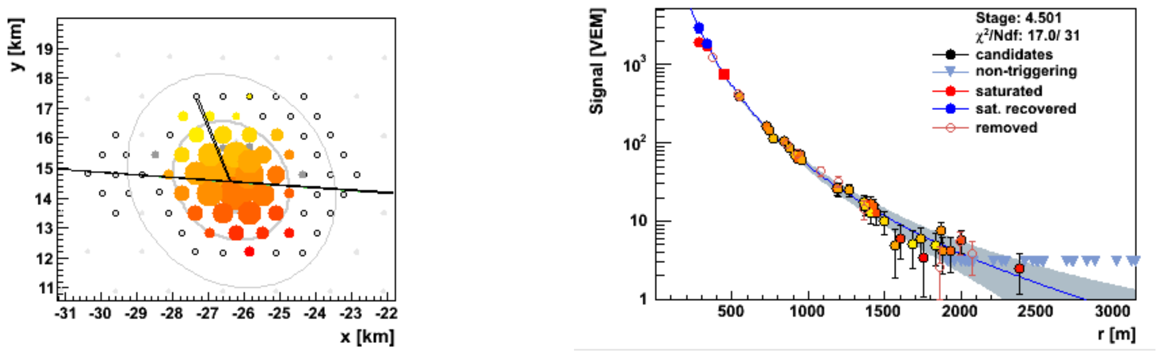

Figure 4.1 The SD trigger map (left) and the LDF reconstruction (right). Note the high number of stations with signal.

4.1 Real event reconstruction

The Auger event 201307906520 was detected on March 21, 2013 at 8:05 AM (UTC+0). It triggered the Coihueco FD and both SDs and MDs in the AMIGA region. It was reconstructed using the Auger Offline package *Framework v2r9p0-svn-trunk* configured in the tri-hybrid mode.

4.1.1 Surface Detector

The SD provides the most reliable information since the number of triggered stations with values higher than the silent limits is 36 (see Figure 4.1). Two of the stations, the closest to the core, were saturated: Heisenberg (1773) at 279 m, and Isidorito Jr. (1813) at 338 m.

Due to the number of triggered stations, the LDF can be accurately reconstructed and the shower parameters extracted (shower geometry and primary energy). Figure 4.1 on the right hand side shows the LDF reconstruction.

Table 4.1 summarizes the main parameters obtained through SD reconstruction, which will be considered as reference values for the cosmic ray shower.

SD Reconstructed Parameters	
Parameter	Value
Energy	$(1.03 \pm 0.03 \pm 0.04)\ 10^{19}\ eV$
(θ,ϕ)	$(39.5 \pm 0.1,\ 108.8 \pm 0.2)\ deg$
(x,y) Core	$(-26.36 \pm 0.01,\ 14.58 \pm 0.01\ )\ km$
S_{450}	$(741 \pm 19(\pm 29))\ VEM$

Table 4.1 Main parameters obtained through SD reconstruction.

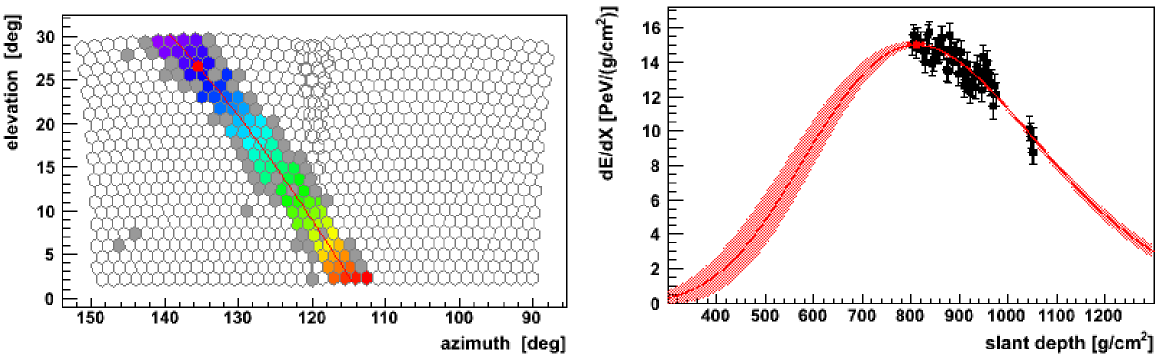

Figure 4.2 PMTs traces left in cameras in bays 4 and 5 (left). On the right, the measured longitudinal profile (black) and its fit (red).

As shown in Table 4.1, the core position and arrival direction were accurately reconstructed within $< 1\%$ and the energy within a $\sim 5\%$. The final uncertainties would be larger than these values due to systematics, but these low uncertainties imply high-quality data reconstruction.

4.1.2 Fluorescence Detector

Fluorescence detector data may provide trustworthy information towards determining the energy and mass composition of the primary particle. Event 21354417 was seen only by two bays at Coihueco, numbered 4 and 5 (see Figure 4.2). Unfortunately there is no HEAT information available for this event (there were difficulties at starting the HEAT DAQ that night[1]). Figure 4.2 shows the event longitudinal profile and its reconstruction.

Although the profile shows a short track length, it is possible to check the curvature of the longitudinal profile of the FD event. If the $\chi^2_{LinearFit}$ ($\sim$ 79) and the χ^2_{GH} ($\sim$ 58) are compared and the GHNdf (60) is considered, both fits are possible and reasonable, but the GH fit is still better ($\sim$1.3 compared to $\sim$1). It can be concluded, then, that the curvature is acceptable. The information obtained from the FD reconstruction is displayed in Table 4.2.

The comparison of Table 4.1 and Table 4.2 indicates that if uncertainties are considered the reconstructed azimuth and zenith angles are in agreement. Moreover, the reconstructed core positions differ by about 1% and the reconstructed energy by 7%, percentages which are within the uncertainties of the detection systems.

---

[1] FD Elog on March 20 2013

FD Reconstructed Parameters	
Parameter	Value
Energy	$(9.66 \pm 0.72)\ 10^{18}\ eV$
(θ,ϕ)	$(39.6 \pm 0.2,\ 109.1 \pm 0.5)\ deg$
(x,y) Core	$(-26.44 \pm 0.02,\ 14.68 \pm 0.01)\ km$
Distance to Eye	$(5.30 \pm 0.03)\ km$
X_{max}	$(812 \pm 15)\ g/cm^2$

Table 4.2 Main parameters obtained from the FD reconstruction.

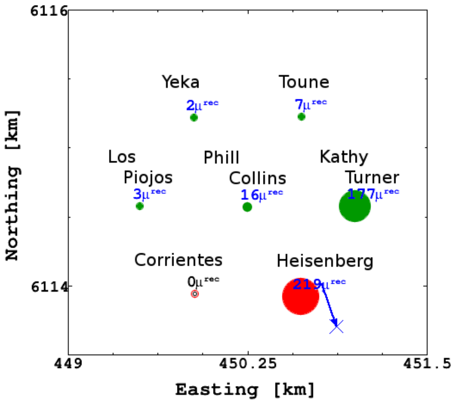

Figure 4.3 PUC stations with their reconstructed muon number. The large number of counted muons at Kathy Turner is due to its extended 60 m^2 area. Heisenberg saturates due to its proximity to the core (blue cross).

4.1.3 Muon Detector

The AMIGA MD prototype array, named Pre-Unitary Cell (PUC), consists of seven 10 m^2 scintillator modules deployed in an hexagon centered around the Phil Collins water-Cherenkov detector (WCD) ([33], [19],CDAS [12]). The Kathy Turner station is a twin-detector position with a 60 m^2 area: four 10 m^2 modules and four 5 m^2 modules. Fortunately, the shower core position is close to th PUC array (Figure 4.3, blue cross), counters triggered and actually Heisenberg, the closed tank saturates. Individual muons (with their associated timing) were counted and the MLDF reconstructed.

By the time the event was acquired, each module high voltage was 960 V and the discrimination level was selected to 100 mV. Laboratory measurements performed afterwards evidence that this selected operation point can introduce possible inefficiencies in the detector. The discrimination level was set too high and therefore some muons can be lost. Five stations were used in the reconstruction: Kathy Turner (ID: 1764, KT), Phil Collins (ID: 1622, PC), Toune (ID: 688, Toune), Los Piojos (ID: 1574, LP), and Yeka (ID: 1570, YEKA). Corrientes (ID: 93, Co) was not working at the time of the event, therefore no muon information of this station is available. As already mentioned, Heisenberg (ID: 1773, Hei) was saturated (the

MLDF reconstruction was done assuming 56 scintillators with signal in a time window as the saturation limit). Nevertheless this station enters in the MLDF reconstruction as a lower muon-number limit. By normalizing the number of muons by the effective scintillating area in each position and using the geometrical reconstruction from the SD, the muon density (ρ_μ) at each distance to the core axis in the shower plane (r) can be obtained. The core distance (in the shower plane) of each station is calculated from the SD geometrical reconstruction: Hei 279 m, KT 724 m, PC 842 m, Toune 1198 m, LP 1405 m, Yeka 1423 m, and Co 956 m. A *Kascade Grande* type LDF [60] is used to reconstruct the muon lateral distribution function. It has two possible free parameters $\rho_\mu(450)$ and β, density at 450 m from the core and LDF slope, respectively.

$$\rho_\mu(r) = \mathrm{K} \times \rho_\mu(450) \times \left(\frac{r}{R_0}\right)^{-\alpha} \times \left(1+\frac{r}{R_0}\right)^{-\beta} \times \left(1+\frac{(0.1r)^2}{R_0^2}\right)^{-\gamma} \tag{4.1}$$

The other three parameters (i.e. α, γ and R_0) are chosen and fixed from end-to-end simulations. Therefore they will differ from those of Kascade-Grande [36, 60]. The distance at which the density is evaluated (450 m) is the optimal distance for this detector array, i.e. where fluctuations and uncertainties are minimized.

The MLDF thus obtained is compared to the SD LDF in Figure 4.4. Within this distance to the shower axis, the slopes are slightly different. It is underlined that the uncertainties (gray surface) are reduced around the region of interest, $\rho_\mu(450)$, probably due to the neighbouring 60 m^2 KT MD.

Table 4.3 summarizes the reconstructed $\rho_\mu(450)$ value from a likelihood fit and the fixed values taken for Equation 4.1. All of them will be compared with simulations of different kinds of primaries and hadronic models in the following sections.

MLDF Reconstructed Parameters	
Parameter	Value
$\rho_\mu(450)$	$(12.3 \pm 1.2)\ \mu/m^2$

MLDF Fixed Parameters	
Parameter	Value
β	1.36
α	1
γ	1.85
R_0	150
r_{opt}	450

Table 4.3 Parameters obtained from an Kascade-Grande MLDF reconstruction of the real event. Only statistic uncertainties are shown for $\rho_\mu(450)$. β is set to the mean value from simulations (see text).

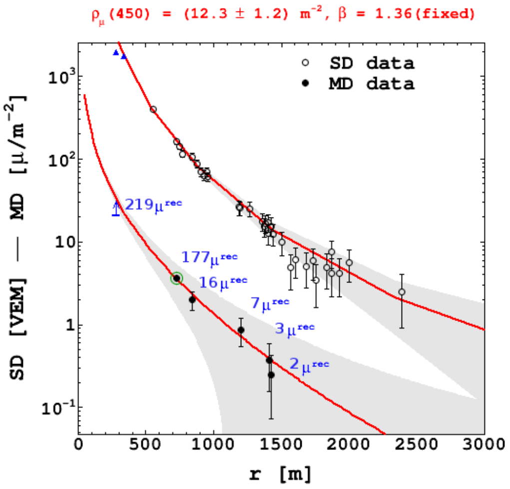

Figure 4.4 LDF vs. MLDF. The figure corresponds to a fixed β MLDF reconstruction (Kascade-Grande LDF parametrisation). The gray surface corresponds to uncertainties arising from the likelihood fit to the available data.

In this particular event the slope β will be fixed since the PUC does neither have enough MDs nor detector area to set it as a secondary free parameter. Fixing the slope improves $\rho_\mu(450)$ estimation by reducing it uncertainty from $\sim 36\%$ to $\sim 10\%$, without introducing any significant difference in the $\rho_\mu(450)$. This large uncertainty reduction in this particular event permits to perform a good-quality mass composition analysis with the MDs data. The chosen β is taken as the mean value of the corresponding values for proton and iron simulations (same shower geometry and energy). See Section 4.2 for details in the influence of β.

4.2 Simulated showers

Seventy showers for each primary (proton and iron) were simulated using *CORSIKA v7370* [31] with the latest hadronic models EPOS-LHC [50] and QGSJetII-04 [47]. In order to compare simulations with the real event, both the simulated shower energy and geometrical parameters were fixed to those of the real event.

Some of the CORSIKA showers main characteristics are enumerated here:

- To generate Cherenkov light in the tank, standard energy cuts were selected: $Ecut_{hadron}$ = 55 MeV, $Ecut_\mu$ = 55 MeV, $Ecut_\gamma$ = 265 KeV, $Ecut_{e+/e-}$ = 265 KeV.
- A thinning of 10^{-6} with the corresponding optimization for 10 EeV was chosen.

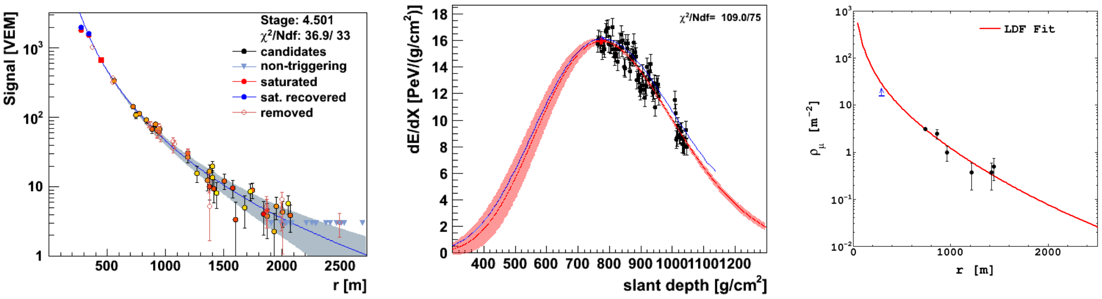

Figure 4.5 Example of an EPOS-LHC simulated and reconstructed proton event.

- The median values of Malargüe magnetic field and atmosphere molecular profile during March (GDAS model) were chosen.
- An altitude of 1560 m.a.s.l was chosen, which corresponds to the area next to the shower core position.
- The hadronic GHEISA model was chosen to depict the low energy range.
- R_{min} was 50 m.Within this radius, particles are treated with the thinning algorithm.

These showers were used as input for the Auger Offline Software. The tri-hybrid event was fully simulated and reconstructed under the same conditions as the real event detected in field. Simulations were performed for the FD at Coihueco, the full SD infill, and the MDs PUC area.

An example of an EPOS-LHC reconstructed proton simulated shower is shown in Figure 4.5 for the three detector systems under consideration.

Table 4.4 shows mean values and σ for each primary and hadronic model. The SD reconstructed energy is compared to the cosmic-ray primary Monte Carlo (MC) simulated energy. The deficit in the reconstructed energy of simulated events is quite apparent.

Primary & Model	$< \frac{E^{MC}-E^{rec}}{E^{MC}} >$	$\sigma(\frac{E^{MC}-E^{rec}}{E^{MC}})$
Proton QGSJetII-04	27%	4%
Proton EPOS-LHC	19%	7%
Iron QGSJetII-04	20%	4%
Iron EPOS-LHC	11%	4%

Table 4.4 Mean and σ of energy difference with MC simulations over 70 showers.

The number of muons imping onto the underground-shielded detectors was compared with the number of reconstructed muons for each simulated shower: the under-counting was

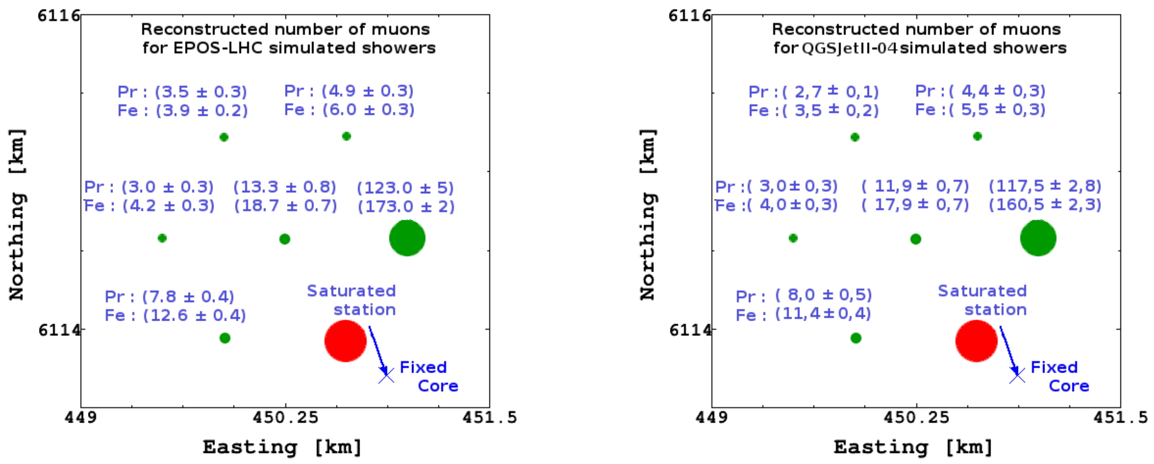

Figure 4.6 Expected muons at each station position from hadronic-models simulations. Mean values and 1σ fluctuation for proton and iron showers are shown.

found to be lower than 5% which is within the current accuracy expected by AMIGA MCs. Figure 4.6 shows the mean value and 1 σ fluctuations of the reconstructed muon numbers at each position. A comparison between Figures 4.3 and 4.6 shows that the number of muons is lower than the number detected in the real event. This is due to the muonic component deficit in simulated showers at these energies.

The deficit on both energy and shower muon component are linked since the latter directly impact on the SD energy reconstruction due to their longer tracks inside water tanks. It confirms the muon-production deficit found in hadronic models [65]. Research on this deficit is one of the mayor science goals of the Auger Observatory which is intimately linked to muon counters. The muon deficit (hadronic model) impacts on the composition determination which it is based on the number of muons of each primary.

As only PUC positions with the deployed associated muon counter are available, 7 positions with signal are at most expected in our simulated events. MDs were simulated assuming they are 100% efficient. An attempt to fit the MLDF was made leaving both $\rho_\mu(450)$ and β as free parameters. Still, it was found that a considerable number of simulated showers had only 4 triggered stations (1 saturated, taken as a lower limit) due to shower-to-shower fluctuations and a possible muon deficit. Consequently, $\rho_\mu(450)$ could not be estimated with high resolution. As already mentioned, it was decided to fix β to 1.36. Figure 4.7 depicts the comparison between the free and fixed β results. The reconstructed $\rho_\mu(450)$ is compared to the expected value extracted from the Monte Carlo simulations. The mean bias in $\rho_\mu^{rec}(450)$ is less than 5% in both cases, but the uncertainty is significantly reduced.

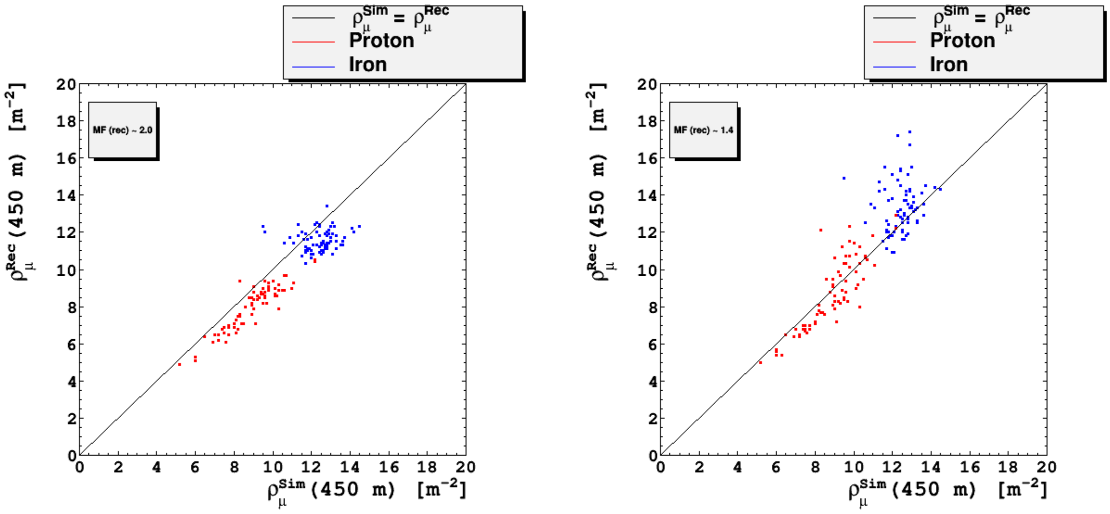

Figure 4.7 Comparison between the fixed (left) and free (right) β results. The reconstructed $\rho_\mu(450)$ is compared to the expected value extracted from the Monte Carlo simulations. See text for details.

The MLDF was then reconstructed, obtaining $\rho_\mu(450)$ from each individual shower reconstruction. Table 4.5 shows, for each hadronic model, its mean values and 1-σ fluctuations as well as its associated Merit Factor (MF) [2].

In short, the MF of the selected parameter, ($\rho_\mu(450)$), is 2.0 for both hadronic models clearly pointing out that MLDF analyses may lead to a strong impact on mass composition determination. As a final comment, it is mentioned, that β was also used as a free parameter but the associated MFs were lower than 1 and as such β appears not to be a good candidate to improve mass composition discrimination among hadronic primaries.

		Parameters		
		Pr	Fe	MF
EPOS-LHC	$\rho_\mu(450)$ $[\mu/m^2]$	9.06 ± 1.22	12.01 ± 0.81	2.01
QGSJetII-04	$\rho_\mu(450)$ $[\mu/m^2]$	8.51 ± 1.06	11.33 ± 0.90	2.03

Table 4.5 Mean and σ of each parameter from histograms of showers without detector reconstruction. The merit factors show the potentiality of $\rho_\mu(450)$ as a mass composition estimator.

Figure 4.8 shows on the left side the comparison between $\rho_\mu(450)$ distributions of the expected underground (i.e all simulated muons reaching the MD depth, no reconstruction) and reconstructed muons. On the right side, the $\rho_\mu(450)$ distributions for reconstructed proton and iron primaries are shown for a selected hadronic model (QGSJetII-04).

---

[2] Defined as $(<\rho_\mu^{Fe}> - <\rho_\mu^{Pr}>)/\sqrt{(\sigma^2_{\rho_\mu^{Pr}} + \sigma^2_{\rho_\mu^{Fe}})}$,

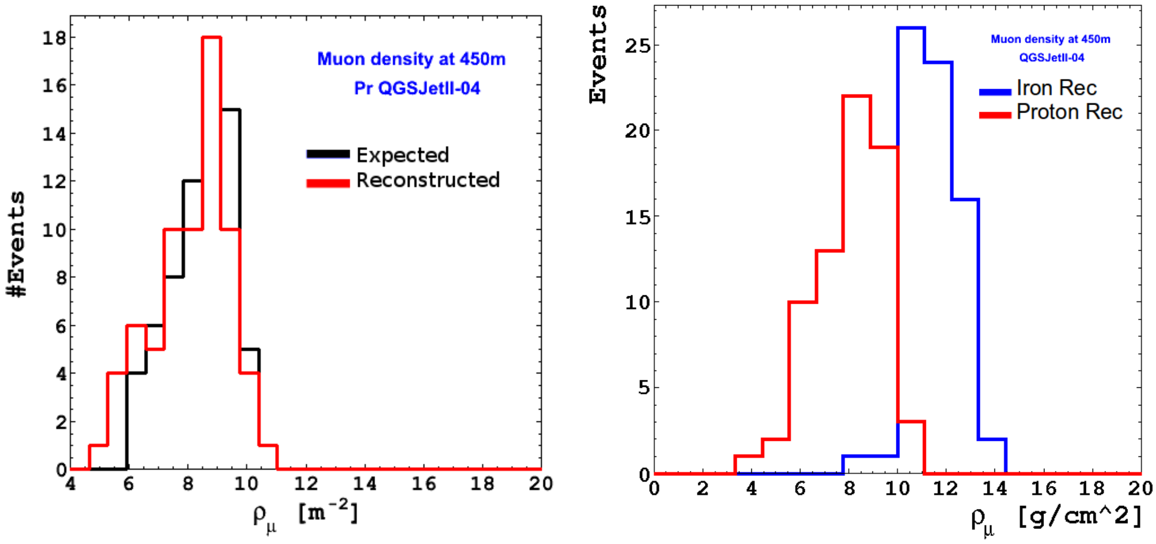

Figure 4.8 $\rho_\mu(450)$ fitted valued from expected and reconstructed underground muons (left, QGSJetII-04 proton). Histograms of reconstructed $\rho_\mu(450)$ for proton and iron primaries (right, QGSJetII-04).

As it can be seen in Figure 4.8, the reconstruction did not introduce significant variations in the estimated parameter. The mean values, σs and MFs for $\rho_\mu^{rec}(450)$ with detector reconstruction, are summarized in Table 4.6 (β = 1.36). It is seen that the detector and reconstruction effects does not alter significantly the MFs which is due to the robust design of the MDS as a 1-bit electronics. They count muons individually by just setting a threshold on the electronics signal.

	$\rho_\mu^{rec}(450)$ $[\mu/m^2]$			
	Pr	Fe	MF	β (fixed)
EPOS-LHC	8.41 ± 1.75	12.18 ± 0.91	1.91	1.36
QGSJetII-04	8.16 ± 1.37	11.51 ± 1.06	1.93	1.36

Table 4.6 Mean and one 1-σ fluctuation of $\rho_\mu^{rec}(450)$ for reconstructed showers considering only PUC MDs.

As a summary, the reduced PUC array has shown as a power tool towards testing hadronic models and elucidating mass composition. It should be considered that a full AMIGA array (i.e. 30 m^2 scintillating area in all infill positions) would improve the $\rho_\mu(450)$ resolution. So the current results must be taken as a lower limit of the full detector potentiality.

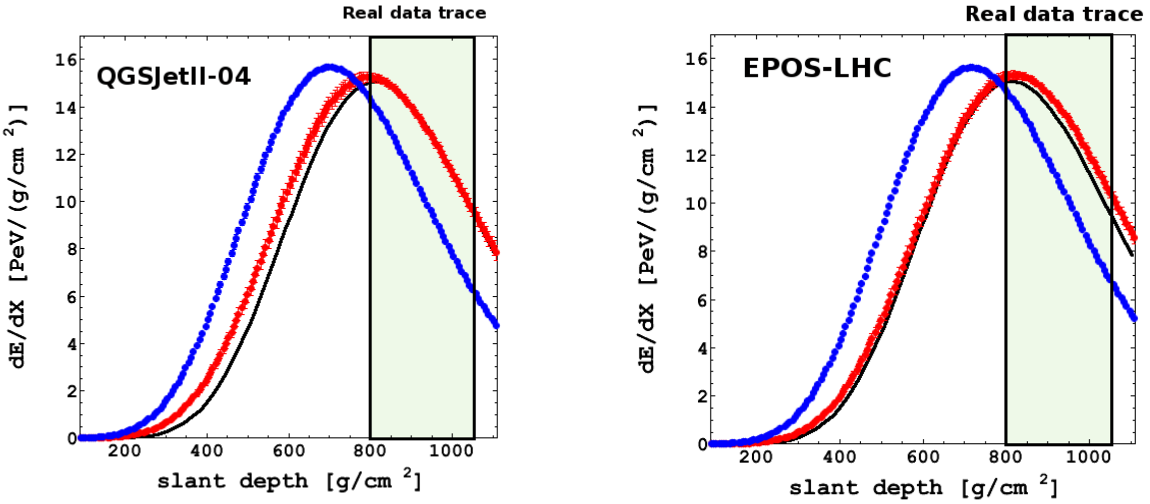

Figure 4.9 Comparison between the average profile of 70 simulated CORSIKA showers (proton in red, iron in blue) and the real event fit (in black). Means and the error of the mean are included.

4.3 Mass composition discrimination

In this section a thorough method to study a single event is depicted. The main parameters describing the detected event are shown and compared with the reconstructed simulations. Consistency of mass assignments from FD and MD will be assessed.

4.3.1 Fluorescence Detector

Longitudinal-profiles mean values from the 70 CORSIKA shower simulations for each primary were obtained and then compared with the reconstruction of the real event (see Figure 4.9. Shown in Table 4.7 is the bias ($X_{max}^{Sim} - X_{max}^{Rec}$) and its $1-\sigma$ dispersion for both hadronic models and primaries.

	EPOS-LHC	QGSJetII-04
Proton	$(29 \pm 17)\ g/cm^2$	$(27 \pm 50)\ g/cm^2$
Iron	$(40 \pm 30)\ g/cm^2$	$(32 \pm 28)\ g/cm^2$

Table 4.7 ($X_{max}^{Sim} - X_{max}^{Rec}$) bias and its 1σ dispersion for both hadronic models and both primaries.

The reconstructed X_{max}^{Sim} value may appear slightly biassed for both hadronic models and primaries but they lie within the X_{max}^{Rec} FD uncertainty (around $40\,\mathrm{g/cm^2}$). Note also that the actual X_{max}^{Rec} FD uncertainty might be larger for this event since its track length does not include X_{max}. The X_{max}^{Sim} values also lie within the 1σ uncertainty arising from shower-to-shower fluctuations (see Table 4.7)

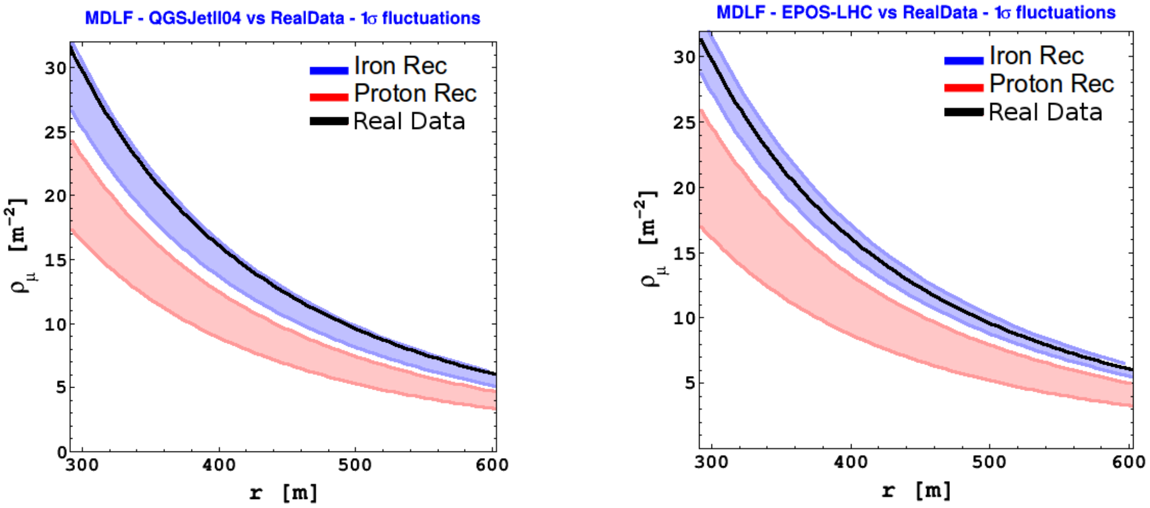

Figure 4.10 MLDF comparison of real event (black) to simulated events for proton (red) and iron (blue). The shaded areas comprise the simulated 1-σ fluctuations.

As shown in Figure 4.9, the real-event longitudinal-profile fit clearly suggests a light primary, both in the overall profile as in the shaded area outlining the region with measured signal.

4.3.2 Muon Detector (MD)

A similar analysis procedure as applied to the longitudinal profile was performed to the muon lateral distribution. It has to be bear in mind that the real-event $\rho_\mu(450)$ parameter is expected to be larger than simulated values due to our current lack of knowledge of the hadronic model in this energy range or a possible underestimation of the primary particle energy. A direct and independent measurement of the muonic component and the longitudinal profile at the same time can help to disentangle the source of the apparent muon deficit.

Inspection of the $\rho_\mu(450)$ results appears to identify the event as a composition more likely to be an iron rather than a proton. For both hadronic models, the simulated proton MLDFs are more than 1 σ away from the detected MLDF. Results are shown adopting the most pessimistic scenario, where detector efficiency systematic uncertainties due to MM's calibration were not taken into account. Therefore the real-event $\rho_\mu(450)$ can have even a higher value.

The comparison to simulations is shown in Figure 4.10 where the real even MLDF is depicted in black, simulated protons in red, and simulated irons in blue. The shaded areas correspond to 1-σ fluctuation.

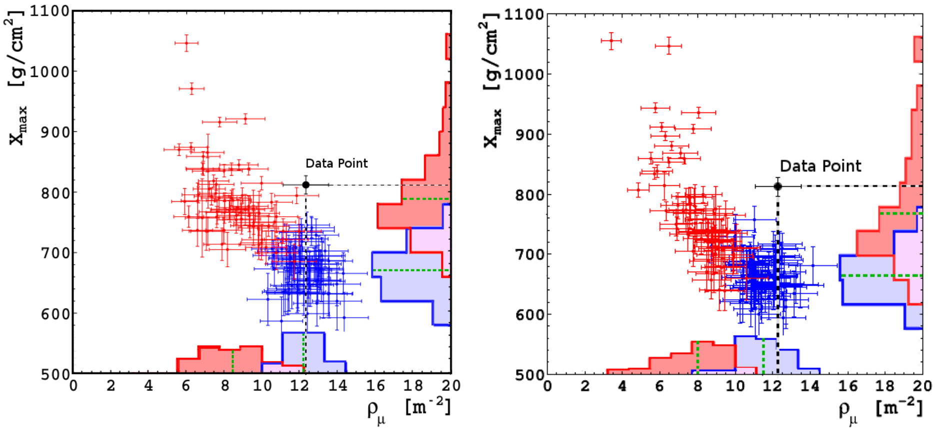

Figure 4.11 Plot combining both mass composition estimators:$\rho_\mu(450)$ and X_{max}. Proton in red, iron in blue, and the detected event in black. EPOS-LHC model on top, QGSJetII-04 model on bottom.

4.4 Possible two-dimensional analyses

Both FD and MD detectors allow for an independent measurement of mass composition estimators, X_{max} and $\rho_\mu(450)$, respectively. Figure 4.11 gathers the information of both detectors. The black dot corresponds to the real reconstructed values. No systematic errors are included in the plot. Green lines depict the mean values for each variable and primary.

This kind of combined FD and MD analysis compared to simulations may give valuable information about hadronic models and their capability to predict shower developments of UHECR primaries. Figure 4.11 depicts a possible composition estimation discrepancy between detectors since FD and MD predict light and heavy compositions, respectively. However [65] states a muonic deficit in the hadronic models employed in this analysis. Table 1 of [65] predicts a deficit of 33% for EPOS-LHC and 61% for QGSJetII-04. Figure 4.12 gathers the information of Figure 4.11 but with this mentioned correction for each hadronic model. This is an example of the potentiality of having an independent measurement of the muonic component but no further conclusions are to be inferred on muon deficit since only one event is analysed.

In order to optimize merit factors, a Principal Component Analysis (PCA) was performed which is based on suitably combining both variable and rotate the axis frame through a δ angle. In order to combine variables, it is necessary to normalize them (see Equation 4.2). This normalization leads both variables to have values contained in the [0,1] interval. They

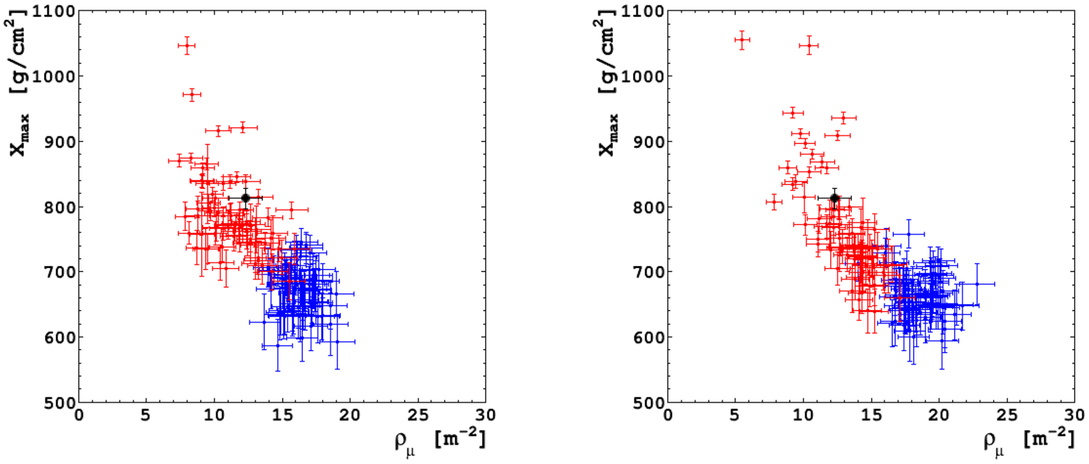

Figure 4.12 Plot combining both mass composition estimators:$\rho_\mu(450)$ and X_{max}. Proton in red, iron in blue, and the detected event in black. A correction of 33% was applied to EPOS-LHC model (left) and a 61% was applied to QGSJetII-04 model (right). These corrections follow the results in [65].

are then combined as shown in Equations 4.3 and 4.4. An angular sweep over δ is performed. Figure 4.11 shows the MF dependence as a function of δ.

$$\begin{aligned}
\rho_\mu^{Pr-Norm}(450) &= (\rho_\mu^{\mathrm{Pr}}(450) - \mathrm{MIN}(\rho_\mu^{\mathrm{Pr}}(450)))/(\mathrm{MAX}(\rho_\mu^{\mathrm{Fe}}(450)) - \mathrm{MIN}(\rho_\mu^{\mathrm{Pr}}(450))) \\
\rho_\mu^{Fe-Norm}(450) &= (\rho_\mu^{\mathrm{Fe}}(450) - \mathrm{MIN}(\rho_\mu^{\mathrm{Pr}}(450)))/(\mathrm{MAX}(\rho_\mu^{\mathrm{Fe}}(450)) - \mathrm{MIN}(\rho_\mu^{\mathrm{Pr}}(450))) \\
X_{max}^{Pr-Norm} &= (\mathrm{X}_{\mathrm{max}}^{\mathrm{Pr}} - \mathrm{MIN}(\mathrm{X}_{\mathrm{max}}^{\mathrm{FE}}))/(\mathrm{MAX}(\mathrm{X}_{\mathrm{max}}^{\mathrm{Pr}}) - \mathrm{MIN}(\mathrm{X}_{\mathrm{max}}^{\mathrm{FE}})) \\
X_{max}^{Fe-Norm} &= (\mathrm{X}_{\mathrm{max}}^{\mathrm{Fe}} - \mathrm{MIN}(\mathrm{X}_{\mathrm{max}}^{\mathrm{FE}}))/(\mathrm{MAX}(\mathrm{X}_{\mathrm{max}}^{\mathrm{Pr}}) - \mathrm{MIN}(\mathrm{X}_{\mathrm{max}}^{\mathrm{FE}}))
\end{aligned} \tag{4.2}$$

$$X_1^{Pr} = \rho_\mu^{Pr-Norm}(450)cos(\delta) - X_{max}^{Pr-Norm}sin(\delta) \tag{4.3}$$

$$X_1^{Fe} = \rho_\mu^{Fe-Norm}(450)cos(\delta) - X_{max}^{Fe-Norm}sin(\delta) \tag{4.4}$$

Table 4.8 summarizes the δ that maximizes the MF for each hadronic model.

	EPOS-LHC	QGSJetII-04
δ	$\sim 34^\circ$	$\sim -6^\circ$
MF	2.21	2.11

Table 4.8 Values of δ that maximize the MF according to Equations 4.3 and 4.4.

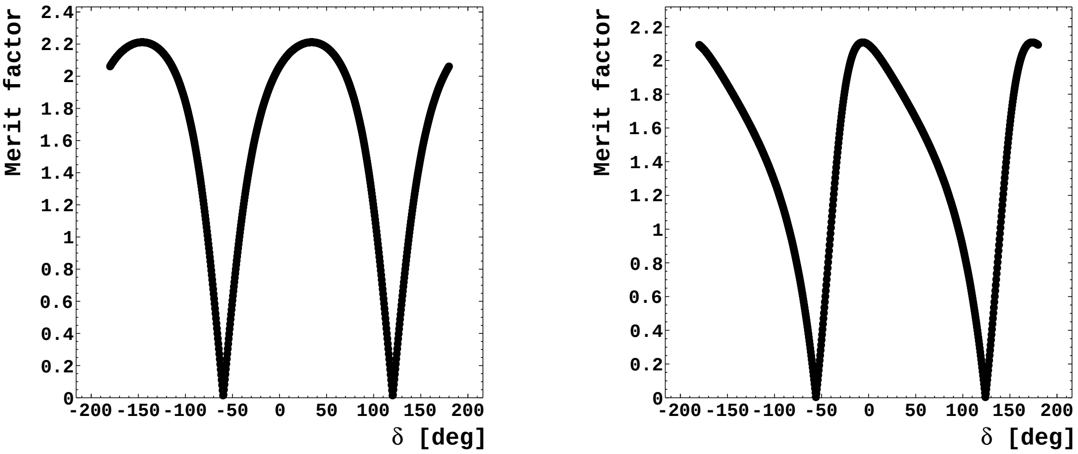

Figure 4.13 MF combining both $\rho_{\mu}^{Norm}(450)$ and X_{max}^{Norm} (Equations 4.3 and 4.4). EPOS-LHC model on the left side and QGSJetII-04 model on the right side.

In both cases, MFs goes slightly over a value of 2, which does not appear to be a significant improvement over the MFs obtained from the sole MD reconstruction.

4.5 Conclusions of the chapter

In this Chapter, the high energy event 201307906520 ($\sim 10EeV$) was fully examined. This is the highest energy event ever seen by the three detectors, SD, FD, and MD. A method based on detailed simulations is outlined which may be applied to any specific events of interest.

A detailed reconstruction of the MLDF was performed and $\rho_\mu(450)$ was estimated using a fixed slope β in the reconstruction ($\beta = 1.36$, derived from simulations). This mass composition estimator was determined within $\sim 10\%$ uncertainty ($\rho_\mu(450) = (12.3 \pm 1.2)\mu/m^2$).

CORSIKA simulations were performed using the reconstructed parameters of the real event as input (i.e. energy and geometry) for proton and iron primaries and the latest hadronic models (QGSJetII-04 and EPOS-LHC). From these simulations, the merit factor discriminator between proton and iron primaries was estimated. The results confirmed $\rho_\mu(450)$ as a quite good mass composition sensitive parameter (MF ~ 1.9). Also the simulated $\rho_\mu(450)$ values prior and post MD reconstructions show just a 5% difference, confirming the robustness of the MD counter design. The results will probably improved when the full AMIGA array is completed. In this analysis, fluctuations in $\rho_\mu(450)$ estimation due to energy uncertainty were not taken into account which might diminish the MFs

Two-dimensional analyses were presented as possible future tools for deconvoluting hadronic models and mass composition towards higher precision analysis with the view of including more than a two-mass groups. A method of linearly combining both FD and MD mass estimators in two new variables (axis rotation as a free parameter) was applied. MF was only slightly improved.

A combined analysis of both FD and MD (X_{max} and $\rho_\mu(450)$, respectively) was performed and simulated showers were compared to the detected event. Data from both detectors evidence a possible contradiction since FD predicts a lighter primary than MD. This discrepancy is solved by assuming the muon deficit obtained by an independent analysis (see [65]).

It is also worthwhile to stress the significant advantage of a $\sim 100\%$ MD duty cycle compared to FD $\sim 10\%$ towards the scientific goals depicted in this Chapter.

Chapter 5

Universality signal model of the muon counter

As it was described in previous chapters, the flux at ultra-high energies cosmic rays (UHECR) is low, therefore their detection can only be achieved by measuring Extensive Air Showers (EAS), i.e. the billions of secondary particles resulting from the interaction of the primary cosmic rays with the Earth's atmosphere. The measurement of the cosmic ray energy, flux, and mass composition relies on an understanding of this phenomenon. In this section, it is going to be shown that hadronic EAS can be characterized, to a remarkable degree of precision, by only three parameters: the primary energy E, the depth of shower maximum $\mathrm{X}_{\mathrm{max}}$, and an overall normalization of the muon component, which is herein called R_{μ}. The relative quantity R_{μ} is defined as the ratio between the muonic signal and the predicted value for a proton QGSJetII-03 shower with the same E and $\mathrm{X}_{\mathrm{max}}$. It is evaluated at a radial distance of 1000 m and azimuth of 90°, being only one number for each shower. Also the cosmic ray particle impinging conditions are included in the description, zenith angle θ and ground air density ρ_{air}. The parameters X_{max} and R_{μ} are linked to the mass of the primary particle, ranging from proton to iron, proton showers have a larger depth of shower maximum than iron showers, while iron showers can contain $\sim 40\%$ more muons than those induced by protons. Both parameters are subject to shower-to-shower fluctuations. This is what is called *air shower universality* [42]. A remarkable feature of shower universality model functional parametrization is that it is independent of hadronic models and primary particle composition.

Previous studies have demonstrated that the energy spectra and angular distributions of electromagnetic particles [18, 40] as well as the lateral distribution of energy deposits close to the shower core [13] are all universal, i.e. they are functions of E, X_{max}, and the atmospheric depth X only. For studies of shower universality in the context of ground detectors, see [39, 48, 49].

In this thesis work, an extension of the air-shower universality applied to underground detectors (i.e. AMIGA MDs) is developed [41].

5.1 Shower universality applied to underground and surface detectors

As described in Chapter 2, the Pierre Auger Observatory was designed to measure cosmic-ray showers with two main detector systems: the fluorescence detector and the surface detector. By sampling the longitudinal development of the electromagnetic shower component close to the shower axis, fluorescence detectors measure both $\mathrm{X}_{\mathrm{max}}$ and E. The systematic uncertainty in the energy E might be around 15%, mainly due to the uncertainties in the air fluorescence yield. The surface detector only samples the properties of an EAS at a given stage of the shower development (ground level) and at several points at different distances from the shower axis (positions of the detectors in the array). To estimate the energy of the primary cosmic ray, Hillas [17] proposed to use the signal at a given distance r from the shower axis, $S(r)$. This distance, named the optimal distance $\mathrm{r}_{\mathrm{opt}}$ [18], is the one that minimizes the fluctuation and it is array-spacing dependent. This signal could then be calibrated in order to obtain the energy from the SD measurement only. This calibration is borne from simulations and has large systematics due to uncertainties in the hadronic models and the unknown primary cosmic-ray composition. Nevertheless, SD calibration can be performed without dependence on hadronic models by using a small subset of the data (hybrid events) which are simultaneously measured by the fluorescence and the surface detectors. This hybrid calibration will yield a mean energy estimate to the $S(\mathrm{r}_{\mathrm{opt}})$ parameter, a signal that would still vary on the primary mass for any given energy since muons deposit very large SD signals (see Figure 5.2). In particular and since γ primaries produce essentially muonless showers, their hybrid calibration energy estimate has to be either increased by $\sim 20\%$ or directly measured with the FD [64]). Note that an outstanding characteristics of reconstructing with the universality method is its independence from either the hadronic model or the mass composition. Therefore, the energy obtained from universality may yield an improved estimate over the hybrid calibration.

The signal $\mathrm{S}(\mathrm{r}_{\mathrm{opt}})$ is the result of the sum of signals from different shower components. The main components are: electromagnetic which to a good approximation depends only on the shower E and $\mathrm{X}_{\mathrm{max}}$; and muonic which, in addition to E and $\mathrm{X}_{\mathrm{max}}$, depends on an overall normalization (R_μ) encompassing the dependence on the hadronic model and primary composition.

Shower universality applied to the PAO started about ten years ago. First results are presented in [66]. PAO air-shower universality was first developed as a tool for getting the universal parameters from SD data [21].

The average signal let by a shower with a given set of (E, $\mathrm{X}_{\mathrm{max}}$, R_μ, θ, ρ_{air}) in ground detector at a certain (r, ψ) is described by air shower universality by [9]:

$$S(E,\mathrm{X}_{\mathrm{max}},\mathrm{R}_\mu,\theta,\rho_{\mathrm{air}})|_{\mathrm{r},\psi} = \sum_{i=1}^{4} S_0^i(DX,E)\cdot f_{\mathrm{mod}}^i(r,\theta,\psi)\cdot f_{\mathrm{conv}}^i(r,DX,\theta,\psi)\cdot f_{\mathrm{atm}}^i(r,\rho_{\mathrm{air}})\cdot \mathrm{f}^{\mathrm{i}}_{\mathrm{R}_\mu,\mathrm{fluct}} \tag{5.1}$$

where

- $S_0^i \cdot f_{\mathrm{mod}}^i$ is the signal deposited by an air shower simulated in an ideal detector, i. e. a detector with the same projected area regardless the impinging particle direction and considering a detector response signal equivalent to a vertical particle.
- DX carries the dependence on X_{max} and geometry and will be described later in the text.
- f_{conv}^i is the conversion factor to a real detector. This correction considered changes in the detector signal due to the change in the projected area and detector response when particles impinges the detector with a different angle from the normal one.
- f_{atm}^i evidences changes in the signal due to seasonal changes in the atmospheric profiles.
- $f_{R_\mu,\mathrm{fluct}}^i$ is a factor that takes into account fluctuations in the shower muon production with an explicit dependence with air shower components.

In the SD universality reconstruction, $\mathrm{X}_{\mathrm{max}}$ is obtained from the SD timing signal [10], and R_μ can only be achieved by calibrating with the FD. This could introduce systematics on the R_μ reconstruction since the muonic component is not directly measured. The new AMIGA MDs can help towards improving the air-shower reconstructions by a direct measurement of R_μ. This has a remarkable impact, specially in the AMIGA energy range, where the transition from galactic to extra-galactic sources is expected. Furthermore, MD muonic component direct measurement can also improve R_μ estimation in the main array by calibrating other detectors in the AMIGA area of detection (like it is expected for the Auger Upgrade).

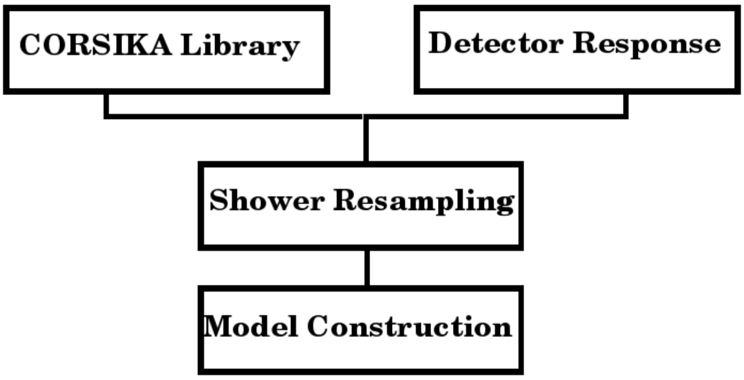

Figure 5.1 Model construction steps.

In this Chapter the design and implementation of the universality signal model for AMIGA MDs will be explained and developed. The SD method already implemented will be taken as a guidance.

In a few words, the construction of the signal model is split in three stages, the first one includes two steps, as it is schematically seen in Figure 5.1. Firstly, an extended library of simulated showers is produced (*CORSIKA Library*) and at the same time, the detector response is built in parallel (*Detector Response*). Secondly, both results are used to estimate the detector response to all the showers in the library (*Shower Resampling*). Thirdly, a semi-empirical model is constructed and the corresponding parameters obtained (*Model Construction*).

In the following sections these four steps will be described in detail as well as the construction of the model parametrization.

5.2 CORSIKA Showers and Detector Response

CORSIKA (*COsmic Ray Simulation for KAscade*, [31]) showers provide the particles at ground level via detailed simulations of all interactions along the shower longitudinal profile.

The CORSIKA library used in this thesis work was the same used for the development of the first version of the SD universality signal model. It is an extended library with proton and iron primaries. Since universality is assumed hadronic model independent, only one model and primary is employed to make the parameterizations. The high-energy hadronic-interaction model used was QGSJetII-03 [58] and the low-energy model FLUKA [24]. For model validation, new simulations were performed with the newest hadronic models derived from the latest LHC data.

The selected library must include a sample of all the expected cases for the measured showers. Accordingly, the library encompasses simulations with different atmospheric parametrizations, in particular twelve atmospheric models (one for each calendar month based on measured mean values at the Observatory site), primary energies, and arrival-direction angles. Shower-to-shower fluctuations are also taken into account since many showers are simulated in each case. In short, the simulated input parameters are:

- Model: QGSJetII-03.
- Primary: proton, iron (iron primaries are used only for validation).
- Impinging angles: 0, 12, 25, 36, 45, 53, 60 [°]. MCs are only expected to measure up to 45°. Higher zenith angles may include clipping corners contamination.
- Energies: 18.6, 19.0, 19.5, 20.0 (logE[eV]). Energy range of the main array.
- For each case there are 120 CORSIKA showers, ten simulated showers for each of the 12 mean monthly models, in order to account possible atmospheric effects in the parametrization.

The CORSIKA primary particle simulation output that must be preserved is the information of the particles on ground after the development of the shower. CORSIKA configuration file and version is included in Appendix A.

Following the ideas developed for the SD, ground level particles are separated into four components: (a) the purely electromagnetic component, (b) the electromagnetic component arising from muon interactions and decays, (c) the electromagnetic component from low-energy hadrons (jet component), and (d) the purely muonic component [38] . An example of the lateral distributions of these four components at ground level is shown in Figure 5.2.

Note that all detector signals will strongly depend on the amount of overburden shielding on the underground detectors (See Figure 5.3). In this thesis two different soil overburdens, ~1.3 m and ~2.3 m, were studied in order to assess their impact on the detected particles. A good approximation on the detected muon threshold energy is obtain by considering a continuous linear energy loss, as described in Equation 5.2.

$$E_{\mu}(x) = E_{\mu 0} - \alpha \rho \, sen(\theta) x \tag{5.2}$$

In Equation 5.2, $E_{\mu 0}$ is the initial muon energy, $\rho \sim 2.4\,\mathrm{g/cm^3}$ is the measured soil density at the AMIGA site in Malargüe, $\alpha = 1.81\,\mathrm{MeV\,cm^2/g}$ (standard rock), θ is the angle of the impinging muon, and x the travelled distance. Therefore soil overburdens of ~1.3 m

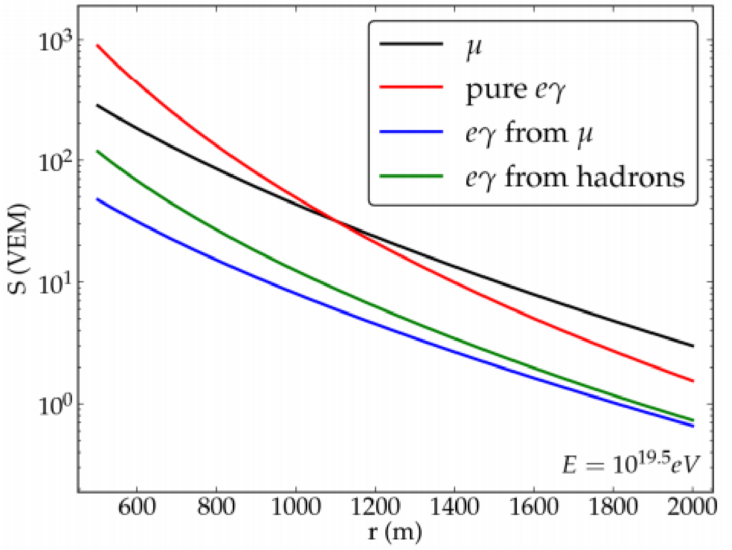

Figure 5.2 Example of the four components that sums up the total signal at ground level.

Figure 5.3 Lateral view of the MD and SD detectors.

and ∼2.3 m will produce threshold energies in vertically arriving muons of ∼500 MeV and ∼1 GeV, respectively.

An accurate muon detector response can be obtained from a set of end-to-end simulation with enough statistics. The Offline Software was used and the simulations were performed following four main steps:

1 Select a particle type, energy, and geometry at ground level that could impinge on the underground MM.

2 Propagate the particles through the ground down to the underground position of the detector. Geant4 tools were implemented for this propose.

3 Estimate the energy deposit for each particle in the simulated detector and set a minimum amount of energy over which the particle is detected. If the particle lets

in the scintillator a minimum energy of 2 MeV (corresponding to a vertical particle passing through 1 cm of scintillator), no other detector efficiency effects are considered and the particle is counted as detected.

4 Repeat the procedure for a large amount of particles of different types, energies, and geometries.

4.1 Particle type: muons. Other particles were initially included but since their contamination was found to be negligible, they were not further considered.

4.2 Particle impinging angles: 0, 8, 12, 20, 25, 27, 30, 36, 38, 40, 42, 45, 47, 50, 53, 57, 60, 62, 64, 66, 68, 70 [°].

4.3 Particle energy: from 0.1 to 20 GeV. For the lowest energies the muon-detection probability is expected to be zero (0.1 GeV $<$ 500 MeV) and for the highest is expected to be one (20 GeV $\gg$ 1 GeV).

The simulated response of each detector system (SD and MM) to each of the four mentioned components is stored. The SD signal is the sum of all four components. Noteworthy, for MMs the soil shields off particles belonging to the first three components, only the muonic component remains.

After the simulation of the detector response, a table with the MM muon-detection probability as a function of particle energy, type, and impinging angle is stored. In Figure 5.4 the detection probability as a function of the impinging particle kinetic energy for the two shieldings under consideration and for different angles is depicted. The GEANT4 results (full circles) are completed with a smooth interpolation (open circles). The results for vertical muons are consistent with the continuous linear energy loss.

These tables are used to resample the CORSIKA showers. The resampling is performed to get the MM response to all simulated shower in the library. The MM signal model is based on these signals and it is made by only using the proton QGSJetII-03 library. Iron primaries are afterwards used to validate the model.

5.3 Universality signal model for an ideal and real detector

An appropriate coordinate, DX, is needed to derive a universal description. DX is defined as a detector distance to the atmospheric slant depth at which the shower develops the maximum number of particles (X_{max}), see Figure 5.5.

The proposed signal model is then the sum of contributions to the total signal from the different components in a detector. As previously mentioned, this parametrization only

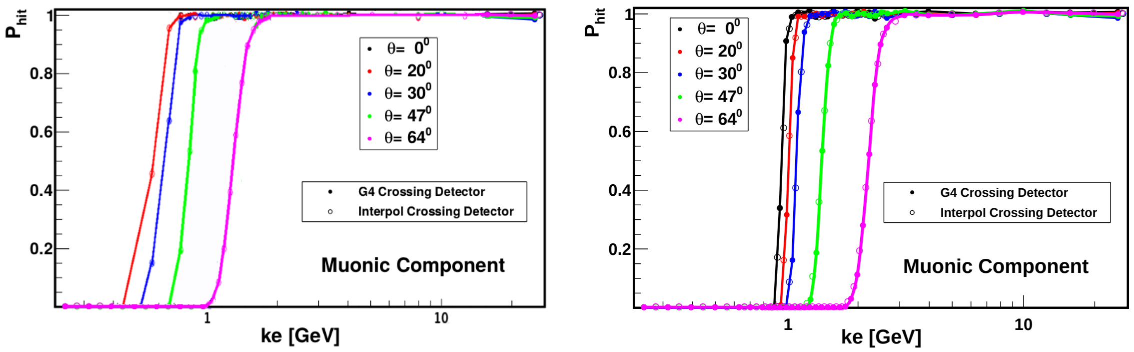

Figure 5.4 Muon-detection probability after traversing two soil shieldings. Different kinetic energies and impinging angles are shown. The shieldings considered are 1.3 m and 2.3 m on the left and right hand side, respectively. The minimum energy of the impinging particle at the detector level to considered as counted is 2 MeV (energy deposit by a vertical muon passing through 1 cm of scintillator).

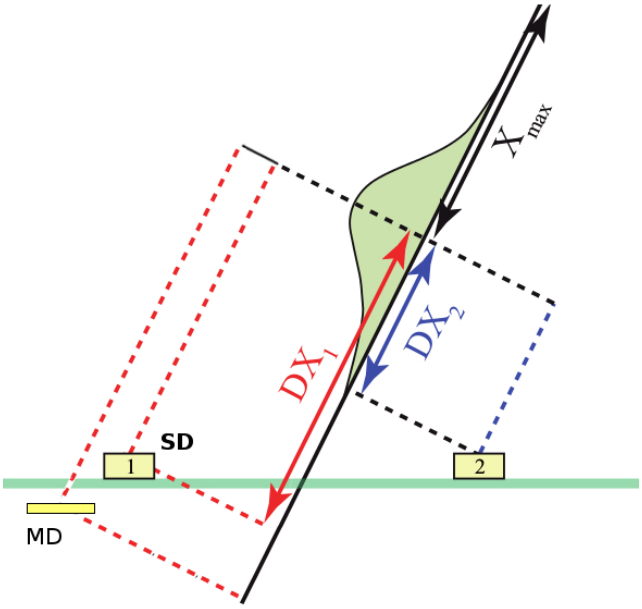

Figure 5.5 DX defined as the integrated density of the atmosphere from X_{max} to the chosen detector position projected onto the shower axis. DX_1 and DX_2 are examples of the definition of DX for two different stations.

depends on E, R_μ, and DX (where DX carries the dependence on X_{max} and the geometry of the EAS).

The universality signal model proposed in this thesis is based on the parametrization detailed in this section.

Parametrized signal for an ideal detector

The density of particles ρ is defined as the number of particles (dN) passing through a differential surface (dS). This surface is perpendicular to p_z, i.e. to the cosine of the angle subtended by the particle direction with the shower axis. Then, the signal in an ideal detector, either on the surface or underground (as in AMIGA), may be written as in Equation 5.3.

$$S_0^t(r,E,DX,\theta,\psi) = \int_{p_z^{cut}(\theta,\psi)}^{1} dp_z \frac{d\rho}{dp_z}(p_z|E,DX,r)T_0(r,DX,p_z)A_V \tag{5.3}$$

A_V entails the projected area which is considered the same for all the impinging particles in the current ideal case (like a spherical detector). T_0 is the detector response calculated for vertical impinging particles. This detector response is described as the integral over all the particle energies of the normalized spectrum.

In Equation 5.3 p_z^{cut} is the value of p_z for which the impinging angle of the particle exceeds ground level. Is the limit that takes into account that no upward particles go into the detector due to the presence of ground, what means that particles coming from below the detector are rejected by cutting p_z range. Ground attenuation makes that these upward particles mainly will not reach the detector. In the following description the definition of this low limit will be clear up. Let us consider $(\hat{x},\hat{y},\hat{z})$ as the versors of the main coordinate directions, $(\hat{x'},\hat{y'},\hat{z'})$ as those of the station (in the shower plane), α as the angle between $\bar{p}$ and $\hat{z'}$, and θ as the angle between $\hat{z}$ and $\hat{z'}$, the zenith angle of the shower. The plane defined by $\hat{x'}$ and $\hat{z'}$ is parallel to the one defined by $\hat{x}$ and $\hat{z}$.

$$\begin{aligned}\hat{p} &= \frac{\bar{p}}{\|p\|} \\ &= -\cos\alpha\,\hat{z}' + \sin\alpha\,\cos\psi\,\hat{x}' + \sin\alpha\,\sin\psi\,\hat{y}'\end{aligned}$$

then also $p_z = \cos\alpha$ and $\sin\alpha = \sqrt{1-p_z^2}$. Thus p_z^{cut} direction may be obtained as the limit when $\theta_p = \frac{\pi}{2}$,

$$\begin{aligned}\cos\theta_p &= -\hat{p}\cdot\hat{z} \\ &= p_z\cos\theta + A_{rad}(r)\sqrt{1-p_z^2}\sin\theta\cos\psi\end{aligned}$$

A plot with the main coordinates definitions is included in Figure 5.6.

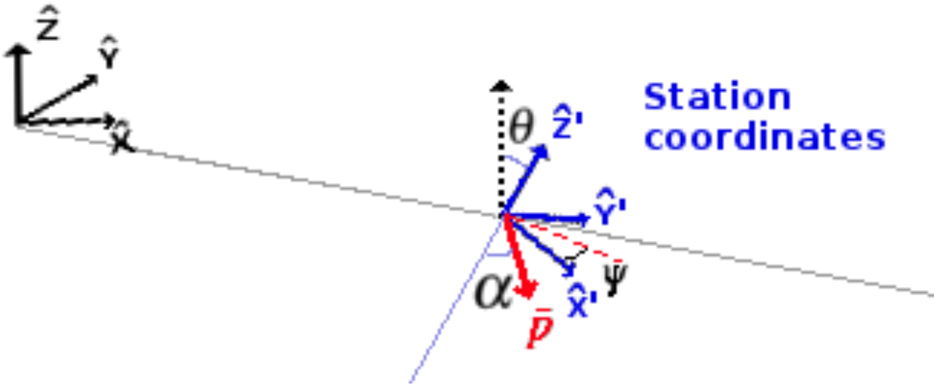

Figure 5.6 Coordinates definition.

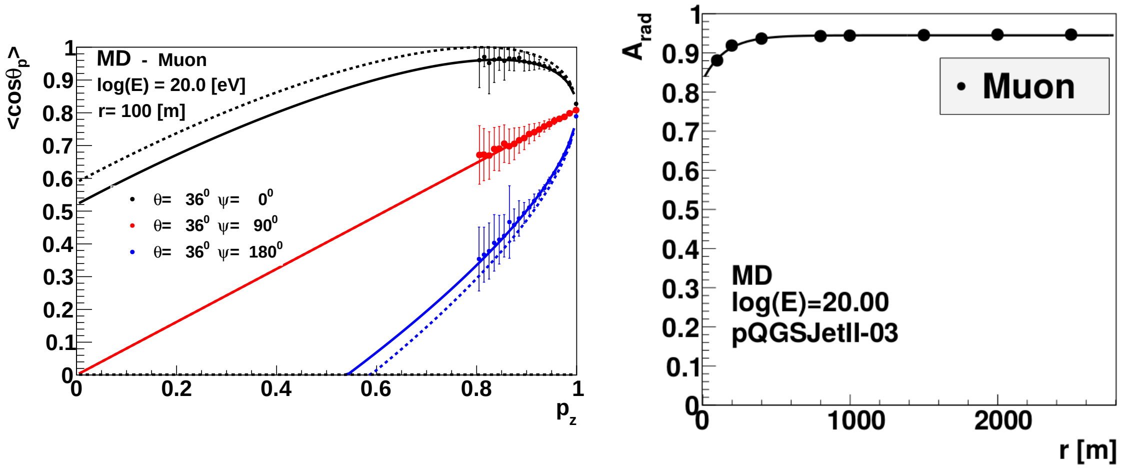

Figure 5.7 Left: mean $\cos\theta_p$ as a function of p_z. The dashed lines correspond to the $A_{rad}(r) = 1$ case. Right: $A_{rad}(r)$ radial dependence for the MD. The differences were observed only very closed to the core. A 100 EeV energy is considered since it would evidence the maximum possible deviation.

If particles diffuse only radially, $A_{rad}(r) = 1$. In this work, this parameter will be obtained as a parametrization from simulations and therefore a radial dependence will be allowed (See Figure 5.7). A pseudo-radial approximation is proposed.

Corrections to S_0^t due to signal dependences on θ and ψ for fixed (r, DX) will be referred to as *Geometrical Asymmetries*, even though there also attenuation effects considered in this description. Failing to consider these effects would lead to a break in the universality concept of the shower shape. These dependences can be grouped by two factors. One of them is related to the low limit of the integral (p_z^{cut}). This dependence becomes apparent in the asymmetry between the young and old part of the shower. By applying a correction, the signal on each station becomes equivalent to that produced by a vertical shower thus suppressing the young-old asymmetry. The second factor will encompass all other effects into a modulation function $f_{mod}(r, DX|\theta\psi)$. Then, Equation 5.3 can be rewritten as Equation 5.4.

$$\begin{aligned} S_0^t(r, E, DX, \theta, \psi) &= S_0(E, r, DX) \cdot f_{mod}(r, DX|\theta\psi) \cdot \int_{p_z^{cut}(\theta,\psi)}^{1} \frac{ds_0}{dp_z}(p_z|DX, r)\, dp_z \\ \text{when} \qquad \mathrm{S_0(E, r, DX)} &= \int_{-1}^{1} \mathrm{dp_z} \frac{\mathrm{d}\rho}{\mathrm{dp_z}}(\mathrm{p_z|E_0, DX, r}) \mathrm{T_0(r, DX, p_z)}\, \mathrm{A}_\nu \end{aligned} \tag{5.4}$$

$\frac{ds_0}{dp_z}$ is depicted by a gamma function (see Equation 5.5).

$$\frac{ds_0}{dp_z}(p_z|DX, r) = \frac{(1-p_z)^\alpha \cdot e^{-(1-p_z)/\beta}}{\Gamma(\alpha)\beta^\alpha} / I_0 \qquad \text{with } \mathrm{I_0} \text{ a normalization factor} \tag{5.5}$$

Following the procedure applied to the surface detector, two magnitudes are defined to characterize $\frac{ds_0}{dp_z}$.

$$\langle p_z \rangle = 1 - \alpha\beta \qquad \sigma_{p_z} = \sqrt{\alpha}\beta \tag{5.6}$$

In the Monte Carlo simulation we only have access to the truncated integral on the right hand side of Equation 5.4. By using the parametrization proposed in Equation 5.5, a description of $\langle p_z \rangle$ and σ_{p_z} as a function of r and DX is obtain. Figure 5.8 shows as an example the parametrization obtained for 1.3 m shielding at the highest energy available in the Monte Carlo simulations (i.e. for maximum possible deviations). Only the muonic component is shown.

Parametrized signal for a real detector

We are now going to consider the case of a real detector instead of a spherical ideal one. Figure 5.9 shows the ratio of ideal to real signals from Monte Carlo simulations. Complete lines are the results from the parametrization obtained after applying the model explained below.

Two corrections are applied to the model in order to take into account the MD geometry. The first one is related to changes in the detector response ($T_{mod}(r, DX, p_z)$) and the second one to changes in the detector area ($A_{mod}(\theta_p)$) away from the spherical shape (see Equation **??** and Equation 5.8). For AMIGA MDs, A_{mod} is the factor needed considering particle flux

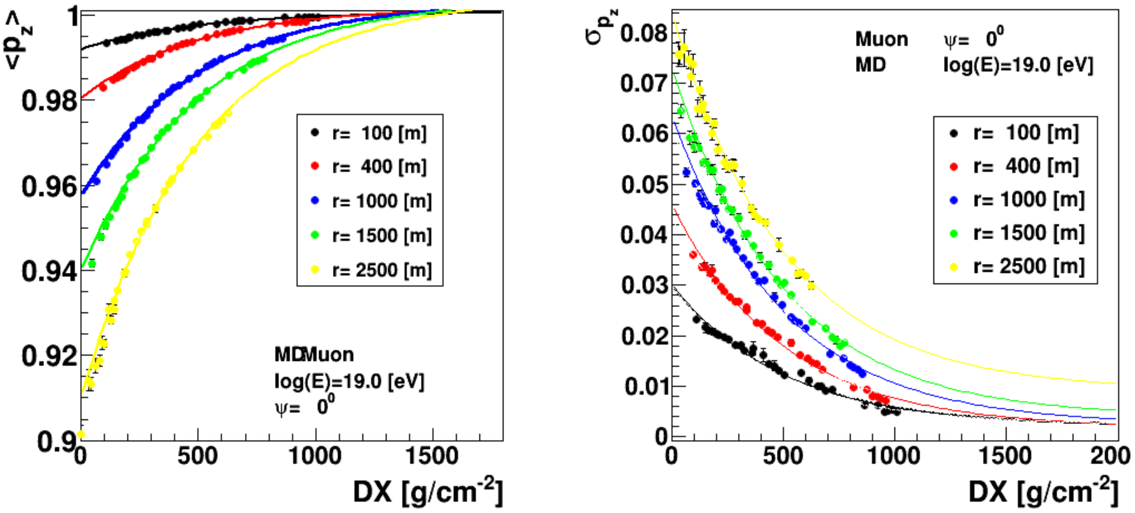

Figure 5.8 Parametrization of $\langle p_z \rangle$ and σ_{p_z} for the particular case of the 1.3 m shielding using proton QGSJetII-03 model. This example corresponds to the pure muonic component. Complete lines are the parameterizations in (r, DX) applied to MD signal model. There are some differences between the parametrization and the simulated data only very close to the core.

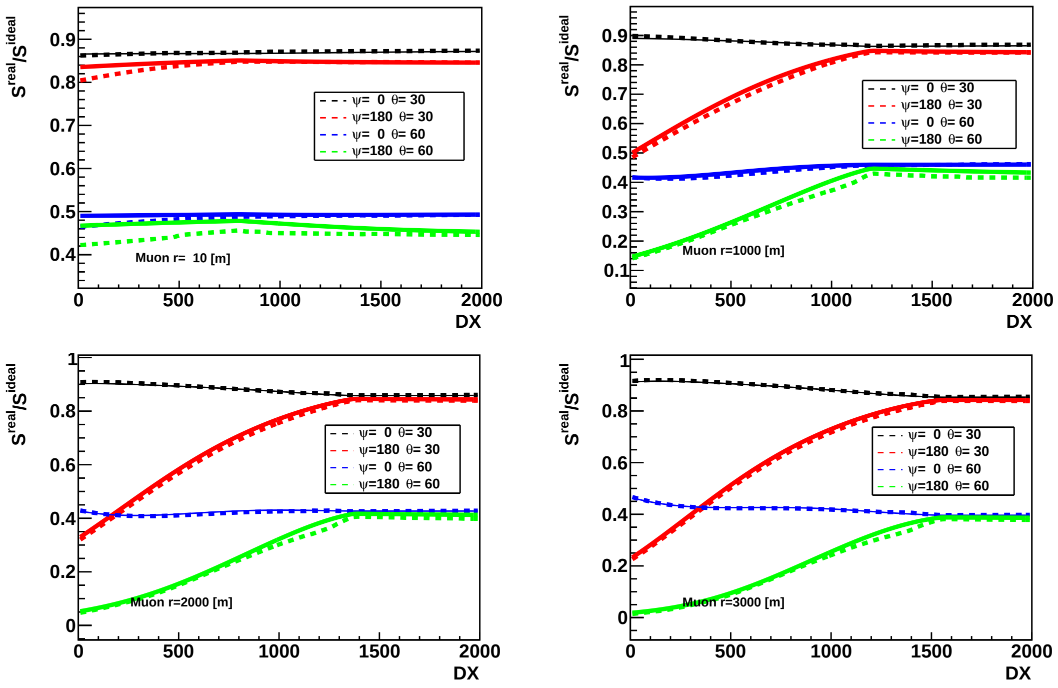

Figure 5.9 Ratio of ideal to real signals obtained from Monte Carlo simulations. Differences for 1.3 m and 2.3 m shielding depths are shown in complete and dashed lines respectively.

to turn A_V into a flat detector and T_{mod} is the ratio of real to ideal detector responses (see Figure 5.9).

$$A_{mod}(\theta_p) = \cos\theta_p \tag{5.7}$$

$$T_{mod}(r, DX, p_z) = \frac{T^{true}(r, DX, p_z)}{T_0(r, DX, p_z)} \tag{5.8}$$

Combining Equation 5.4, Equation 5.7 and Equation 5.8, the signal in a real detector can be in a simplified way written as:

$$S_0^t(r, E, DX, \theta, \psi) = S_0(E, r, DX) \cdot f_{mod}(r, DX|\theta\,\psi) \cdot f_{conv} \tag{5.9}$$

f_{conv} is defined as in Equation 5.10.

$$f_{conv} = \int_{p_z^{cut}(\theta,\psi)}^{1} \frac{dS_0}{dp_z}(p_z|DX, r) \cdot T_{mod}(r, DX, p_z) \cdot A_{mod}(\theta_p)\, dp_z \tag{5.10}$$

The product $A_{mod}T_{mod}$ is parametrized using the Monte Carlo simulations of the previously described shower library. Figure 5.10 shows the results for 1.3 m shielding, the reference primary particle and hadronic model (proton and QGSJetII-03). Two further cases are included in the figure as reference values: $A_{mod}T_{mod} = 1$ and $T_{mod} = 1$. The second one shows that A_{mod} depends linearly with $\cos_{\theta_p}$. Differences between 2.3 m and 1.3 m shielding were lower than 0.5%. This result was expected since this correction is only modified by detector shape and response.

Other effects that depends on the shower geometry and on the position of the station are the atmospheric effects [37]. Since the atmospheric models are the same for both SDs and MDs, these corrections remain unchanged, no further upgrades or new implementations are needed. The relevant parametrization is describe in [37].

Finally, the last parametrization needed before parameterizing $S_0(r, DX, E)$ is the estimation of f_{mod}. To this effect, the predicted signal divided by f_{conv} and the atmospheric effects was compared with the Monte Carlo simulation divided by the same effects. These results are shown in Figure 5.11, left (bottom and top) for $f_{mod} = 1$. The energy selected to show these results is the same energy as the one used in the following section for validation.

It is clearly seen that there is an extra factor missing, the expected f_{mod}. A simple parametrization is proposed in Equation 5.11.

$$f_{mod}(r|\theta, \psi) = M_0(r, \theta)(1 + M_1(r, \theta)\cos\psi) \tag{5.11}$$

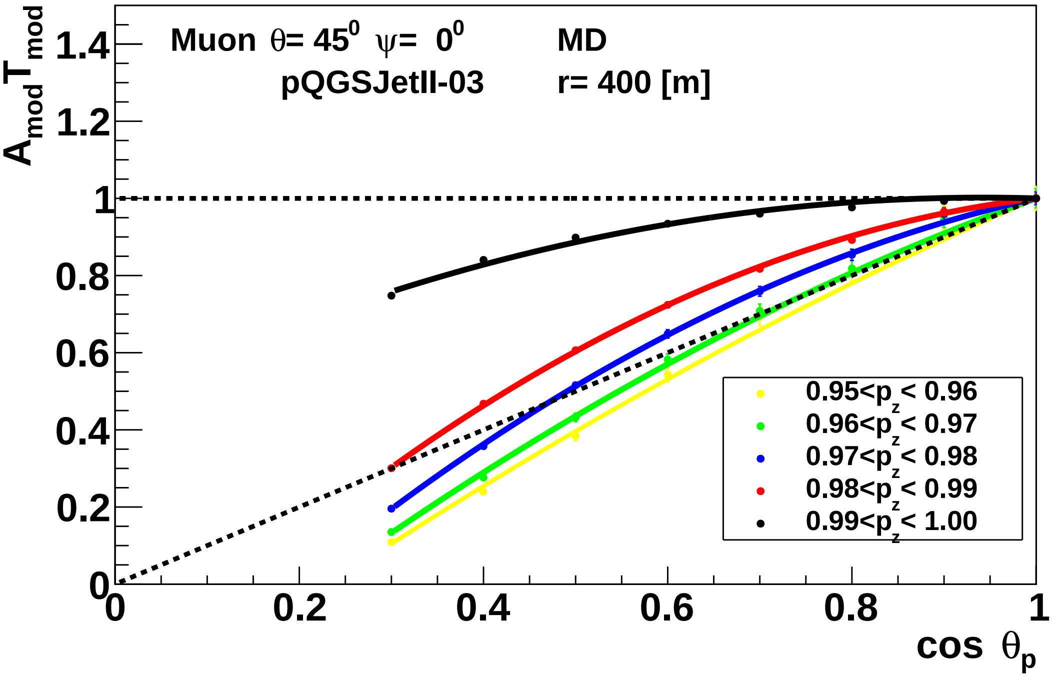

Figure 5.10 $A_{mod}T_{mod}$ is parametrized using the Monte Carlo simulations. Different p_z bins are included with different colours.

Once M_0 and M_1 are obtained, a comparison of the Monte Carlo signals with the new correction is performed and the results shown in Figure 5.11, right (bottom and top). As it can be observed, the differences previously observed in Figure 5.11, left (bottom and top) were corrected with the f_{mod} factor; and now differences with the predicted signal remains below 5%.

5.4 Universality Signal Model - S_0 parametrization

As described at the beginning of this Chapter in Equation 5.1 the method applied in order to parametrize the expected signal consists of, as a first step, to parametrize all possible effects due to both atmosphere and detector response as corrections to the ideal detector response S_0. Equation 5.12 summarizes these effects.

$$S(E,R_\mu,DX) = \sum_{i=1}^{4} S_0^i(DX,E) \cdot f^i_{\text{mod}}(r,\theta,\psi) \cdot f^i_{\text{conv}}(r,DX,\theta,\psi) \cdot f^i_{R_\mu\text{fluct}} \tag{5.12}$$

where

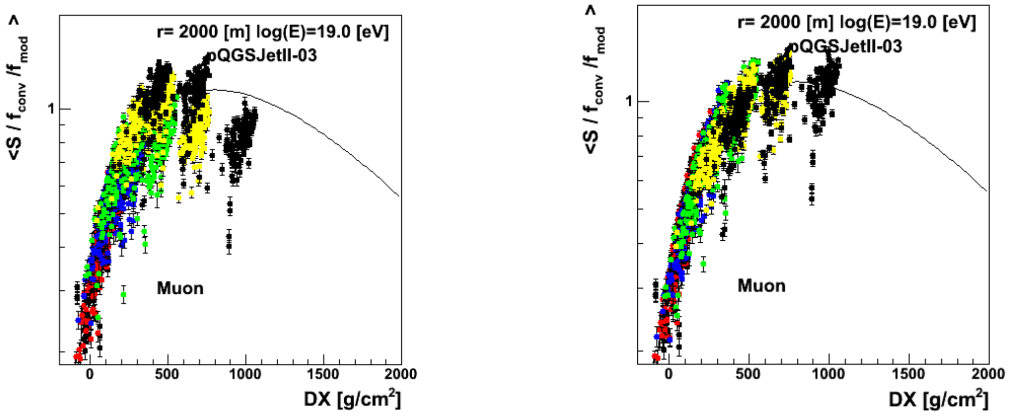

(a) DX dependence. f_{mod} = 1. (b) DX dependence. f_{mod} from parametrization.

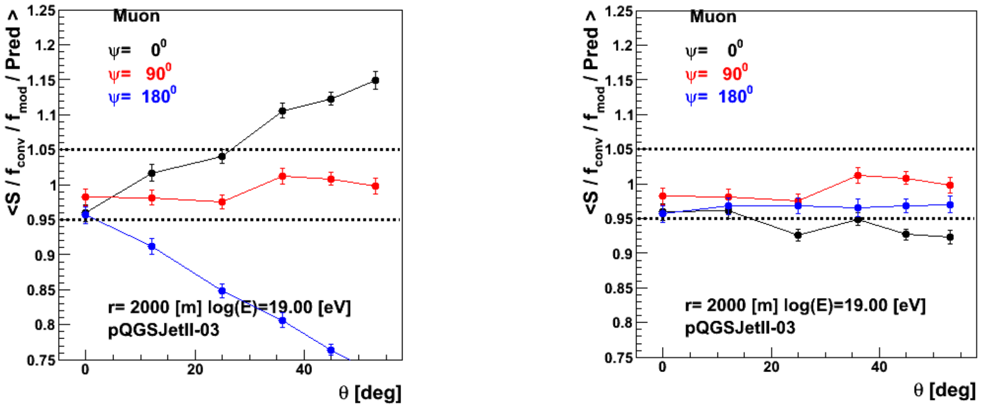

(c) θ dependence. f_{mod} = 1 (d) θ dependence. f_{mod} from parametrization.

Figure 5.11 Results applying and without applying the f_{mod} correction.

- $S_0^i(DX,E)$ is the ideal 10 m^2 detector signal without any detector geometry or atmospheric effects.

- DX carries the dependence on X_{max} and atmospheric development geometry.

- f^i_{mod} is the conversion factor from shower signal into ideal detector signal at (θ,ψ).

- f^i_{conv} is the conversion factor to a real detector.

- $f^i_{R_\mu,\text{fluct}} = \{1, R_\mu, R_\mu, R^\alpha_\mu\}$ is a factor for each shower component that takes into account fluctuations in the shower muon production which explicitly depends on each component as follows: $S = \{S^{\text{ref}}_{\text{em}} + R_\mu\,[S^{\text{ref}}_\mu + S^{\text{ref}}_{\text{em}\mu}] + R^\alpha_\mu\, S^{\text{ref}}_{\text{em Had}}\}$

The muon scale, R$_\mu$, (see Equation 5.13), is a ratio whose denominator is obtained from simulations of proton showers with QGSJetII-03 as a hadron model and at a distance to ground of $DX = 400\,g/cm^2$. The numerator for real data is the shower muonic component at a fixed distance to the ground. R$_\mu$ will be the output parameter of the universality model when applied to muon counters.

$$R_\mu(E) = \frac{S_{0,\mu}(r = 1000m, DX = 400g/cm^2, E)}{S_{0,\mu}^{ref}(r = 1000m, DX = 400g/cm^2, E)} \tag{5.13}$$

Each ideal signal component (S_0^i) detected by the muon detector or by the water-Cherenkov detector is described with the general function shown in Equation 5.14. It was found that both detectors are parametrized by this function with only different parameters values.

$$S_0^i(DX,E) = S_{\mathrm{ref}} \left(\frac{E}{10^{19}\mathrm{eV}}\right)^\gamma \left(\frac{DX - DX_0}{DX_{\mathrm{ref}} - DX_0}\right)^{\left(\frac{DX_{\mathrm{max}} - DX_0}{\lambda(E)}\right)} exp\left(\frac{DX_{\mathrm{ref}} - DX}{\lambda(E)}\right) \tag{5.14}$$

The AMIGA MD's signal detected was parametrized based on this model description for two different shielding: 1.3 m and 2.3 m. In the previous Sections all the corrections applied were explained. The parametrization of the MD signal for an ideal detector, in an ideal atmosphere and without any asymmetry effects, is obtained from Equation 5.14. The special case of the muonic component (including the dependence on R_μ) is shown in Equation 5.15.

$$S_0^\mu(DX,E,R_\mu) = R_\mu \left(\frac{E}{10^{19}eV}\right)^\gamma S_{ref} \left(\frac{DX - DX_0}{DX_{ref} - DX_0}\right)^{\left(\frac{DX_{max} - DX_0}{\lambda}\right)} exp\left(\frac{DX_{ref} - DX}{\lambda}\right) \tag{5.15}$$

$$S_0^\mu(DX,E,R_\mu) = R_\mu E^\gamma f(DX) \tag{5.16}$$

In the case of the muon detector, some assumptions were applied: $\lambda(E) = \lambda$, $DX_0 = 250$ g/cm^2, and $DX_{ref} = 600$ g/cm^2. In Figure 5.12 all the parameters included in Equation 5.15 are plotted as a function of the radial distance to the shower core. The same parameters but for the surface detector are included as reference values. Appendix A includes a description of the functions selected to the parametrization and included in the signal model.

The estimated γ, results in a value of about 1, and hence E and R_μ are strongly correlated. If we only consider the surface detector universality model for the total signal, it would be very difficult to come to an unbiased and precise value for both parameters (total signal and energy). A direct measurement of the muonic component from the addition of muon counters to the reconstruction procedure complements the description and facilitates an independent estimation of both parameters with good resolution. This is further to other advantages of

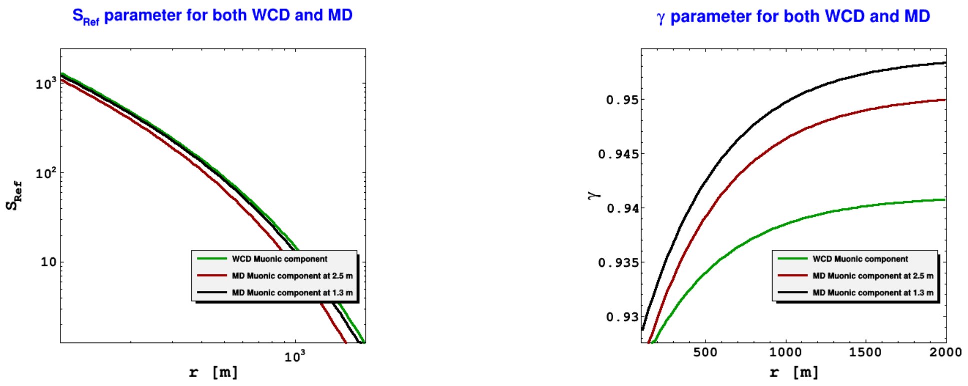

(a) S_{ref} parameter as a function of the radial distance to the shower core.

(b) γ parameter as a function of the radial distance to the shower core.

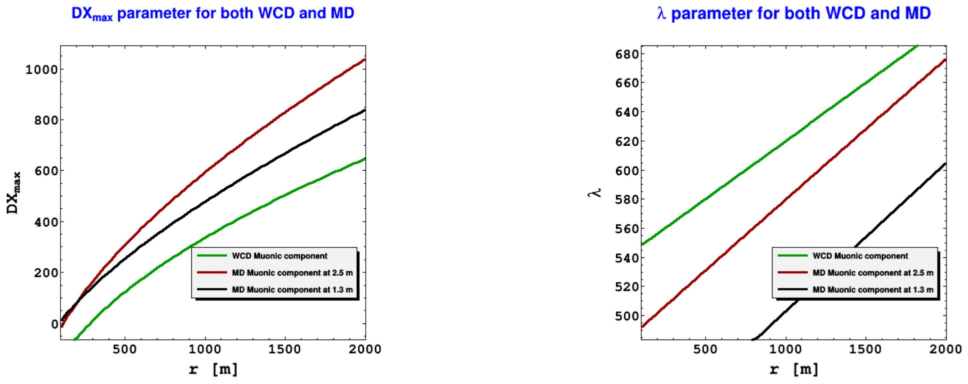

(c) DX_{max} parameter as a function of the radial distance to the shower core.

(d) λ parameter as a function of the radial distance to the shower core.

Figure 5.12 Parameters of Equation 5.15.

experimentally measure the shower muon component rather than exclusively depending on models. In short experiments and models complement and enhance each other.

By following the procedure outlined in Figure 5.1, two independent signal models are now available: one for the surface detector and another for the muon detector. By combining all CORSIKA showers, S_{ref}, γ, DX_{max} and λ were parametrized as a function of the station distance to the core, r, for MD signals special. These parametrizations fully complete the requisites of Equation 5.14. Some examples of the signal of different showers and the model are given in Figure 5.13. The examples included in Figure 5.13 are the results obtained for the MD at the lowest energy included in the model construction.

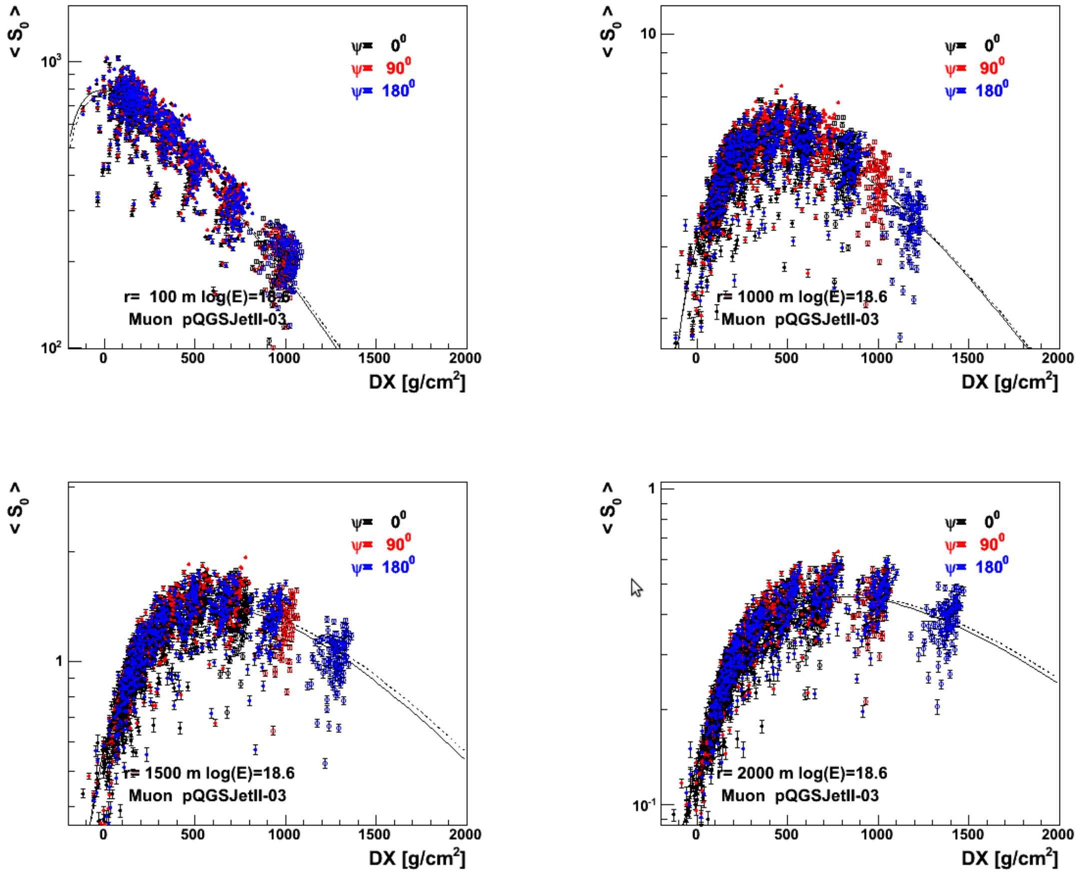

Figure 5.13 Ideal detector signal as a function of DX. Each bunch corresponds to a different zenith angle of the impinging shower. The colors represent different azimuth angles. Dotted and full lines correspond to the respective models for proton and iron. Due to the small differences, the parameters for the proton showers were used as the parameters of the MD final model.

5.5 Conclusions of the chapter

The model described in this chapter [41] extends the universality model to MD signals. The universality shower parameters are E, X_{max}, and R_μ. They could be derived, for instance, from the event SD signals plus known FD calibrations or from a direct measurement. This universality signal model upgrade allows the estimation of the muonic content combined with the other parameters. All the simulations were done successfully obtaining the universal shape parameters that describe the MD signals. Direct muon-shower content measurements, by including the MD signals in universality reconstruction procedure, will significantly reduce systematic uncertainties on these three parameters (see next chapter). Therefore knowledge of these three parameters from a hybrid detection followed by reconstruction within the universality model will permit to pursue a significantly better identification of both hadronic model and primary mass composition. On this identification lies the proposed scientific goals of the Pierre Auger Project.

The strength of the proposed universality MD model is that it does not depend on neither the shower primary particle nor on the hadronic model (see next chapter).

Chapter 6

Validation of the shower universality signal model

A main advantage of the universality model is that the parametrization obtained is quite independent on either the primary particle or the hadronic model upon which it is constructed. This is of uppermost relevance since it allows to safely apply the model to Observatory data to which neither the primary composition nor the hadronic model, without extrapolation, is a priori known. In this Chapter the signal model obtained for MMs will be validated by several tests. To begin with the shower parameters *Energy*, R_μ, X^e_{max} will be taken as input and the detector signal derived from the universality model. Then, the inverse procedure will be undertaken and the *Energy* and R_μ will be obtained (X^e_{max} is related to the time model, outside the scope of this thesis work).

6.1 Accuracy of the proposed MMs signal model

In this chapter, predictions from the universality model are compared to simulated data. As mentioned before, the universality model relies only on three parameters: *Energy*, R_μ, X^e_{max} (or X^μ_{max}). Only these three parameters will be assumed to be known and from them, the signals for each detector (in an ideal detector system) will be predicted by using the model proposed in the previous chapter. These signals were then compared to the simulated signals for those detectors.

As a first step, the signal of the ideal detector (S_0, without considering signal corrections) was compared to the model predicted (Pred, from 5.15) for each station and for all simulated showers. As a result, different energies and geometries were studied in detail to validate the

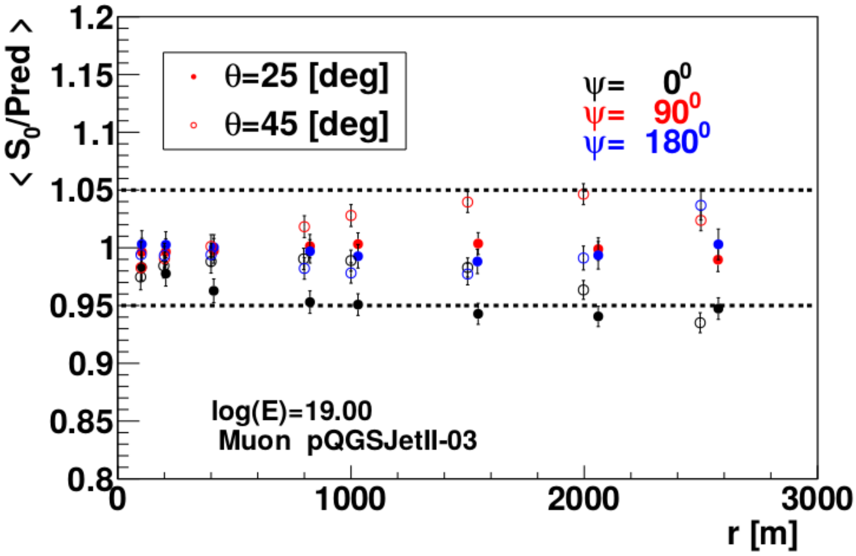

Figure 6.1 Mean ratio between MM ideal signal (S_0) and the model predicted signal (Pred). Predicted signals do not differ from ideal signals by more than $\sim 5\%$.

accuracy of the proposed model. Figure 6.1 depicts a comparison for a given hadronic model and primary particle and different shower geometries.

The comparison exemplified in Figure 6.1 evidences small differences over variations in shower geometry and primary energy. Differences were found to be lower than 5%, for all the energies and geometries. All the energies available in the library were tested in the same core distance range. The hadronic model used was QGSJetII-03. Farther away distances are noisier since the amount of detected muons abruptly decreases. For MMs, only detectors with distances up to 1500 m were taken into account. Signal for larger distances would be dominated by shower to shower fluctuations. Close to the core, the prediction overestimates the muonic signal. This effect can be correlated to saturation effects.

As a second validation step, Figure 6.2 and Figure 6.3 show that in a station-by-station comparison, the predicted signals (now including signal corrections) do not differ from the true signals by more than 10%, and in most cases considerably less. Shown in each figure are different energies, primary particles, distances to the shower core, and zenith angles. The azimuth angle was set to 45 ° and to 135 ° in Figure 6.2 and Figure 6.3, respectively. Larger differences (closer values to 10%) are evidenced close to the shower core, probably due to saturation effects, and very far away, since the muon density is smaller and poissonian uncertainties become relevant. Even more, in the radial distances of interest for these energies, [200,1500] m, differences are lower that 5 %. This last radial range is the selected for the

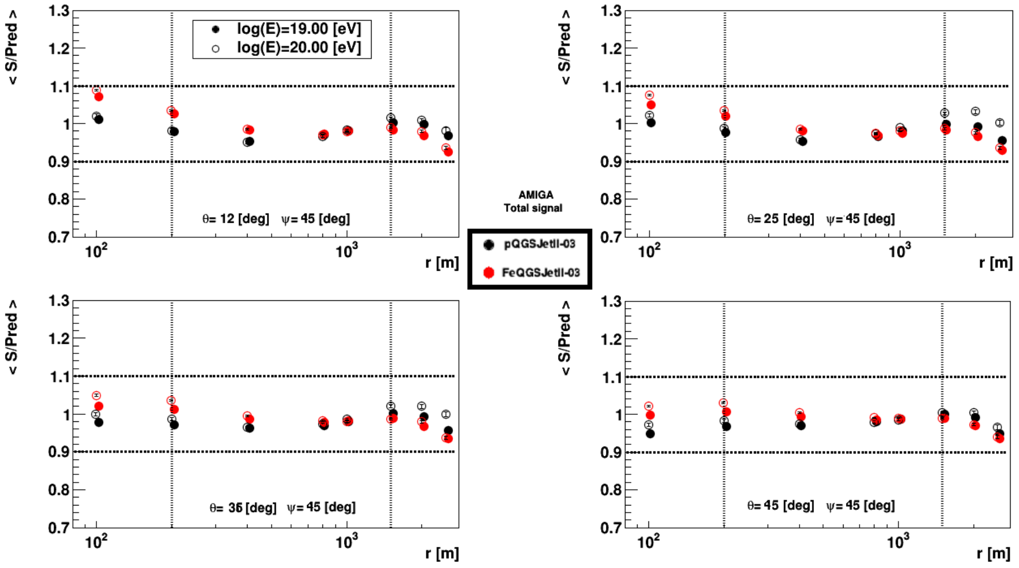

Figure 6.2 Mean ratio between the real detector signal (S) and the model predicted signal(Pred) for stations at an azimuth angle of 45°. All relevant corrections due to atmospheric and geometrical effects are included. In all the examples, the real to predicted signals do not differ, in average, by more than 10%.

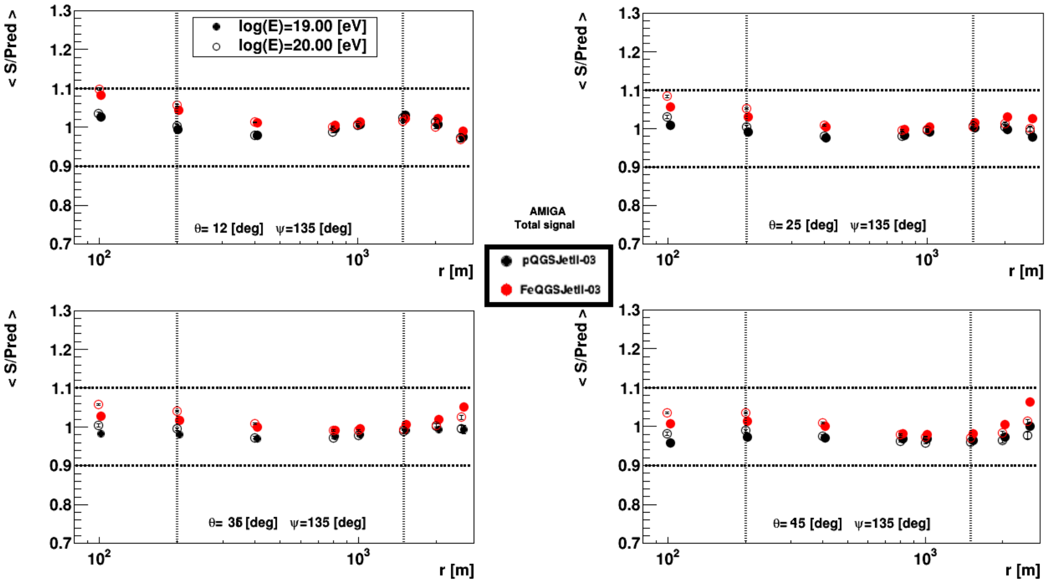

Figure 6.3 Mean ratio between the real detector signal (S) and the signal predicted by the model (Pred) for stations at a azimuth angle of 135°. All relevant corrections due to atmospheric and geometrical effects are included. In all the examples, the real to predicted signals do not differ, in average, by more than 10%.

analysis in the following to reduce possible biases in the reconstruction due to stations outside this selected radial interval.

Similar results to those shown in Figure 6.2 and Figure 6.3 were obtained for different primary energies and shower geometries. The proposed universality signal model appears to correctly yield predictions for different primaries, as claimed by the model. Real to Predicted signal ratios for either proton or iron primaries are esentially independent of the employed input normalization (i.e. QGSJet-03 proton and QGSJet-03 iron give almost identical results)[41]. They only substantially differ in the muon content factor R_μ and others main shower parameters employed in the universal description (i.e. $\mathrm{X}_{\mathrm{max}}$). These signal comparisons do not consider muon detector effects that are going to be included in a full detector simulation in the next section.

6.2 Towards an improvement in the primary cosmic-ray energy estimation

A reconstruction procedure combining different detector data in a multi-parametric analysis would clearly be the best way to proceed. Therefore, a possible aim would be to combine the universality parametrizations of both 100% duty cycle detector types (SD and MD) to obtain shower parameters with a better resolution and less systematics uncertainties. A universality shower reconstruction procedure would involve a global likelihood method that estimates the shower parameters by using the signals measured by both, surface and underground detectors, as an input.

In the previous section, the model-prediction accuracy was shown for individual detector signals. In the following, a full detector simulation is performed and a multiparametric reconstruction is both implemented and tested in order to estimate the primary-particle relevant parameters.

6.2.1 Offline reconstruction-module implementation

The Offline framework [56] is the official software employed by the Pierre Auger Collaboration to both simulate detectors and reconstruct the observatory data. The Offline framework was developed in a modular structure that allows sequential modules to be applied to data in order to reach the desired data reconstruction. Therefore, during this work, the Offline framework was improved by adding a new reconstruction module, included in the reconstruction sequence, that affords universality reconstruction within Auger data. Figure 6.4 depicts the structure of the new implemented module and its main complementary functionalities.

The new implemented module is called UniversalityFitter and it can be configure with its configuration file to different reconstruction options. Along this thesis work, additional

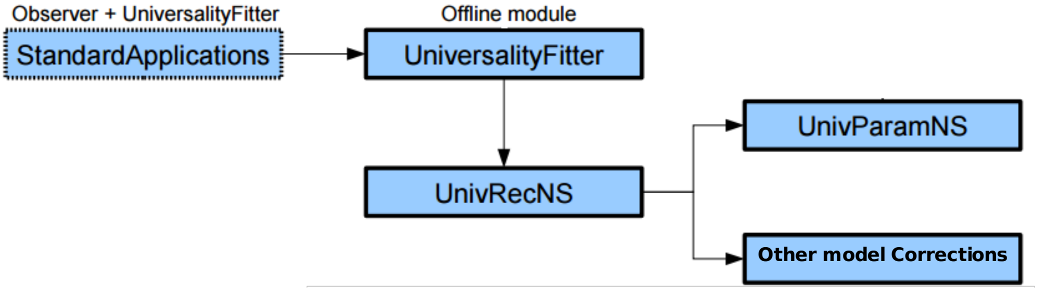

Figure 6.4 [Offline module where MD updates were implemented.]Offline Module improved to include MD muon data in the universality reconstruction. For details on the implementation, see Appendix A.

coding was added to the UniversalityFitter module, and to the complementary UnivRecNS, UnivParam and Other Model Corrections models to include the MD parametrization and to be able to use MD data in the combined hybrid reconstruction. For details on the implementation, see Appendix A.

Data reconstruction is reached by combining the information of the SD and the MD detectors. In the following, it will be shown that the independent measurement of the muonic component performed by the muon counters contributes to improve the Energy and R_μ estimation.

In order to correctly estimate the parameters of interest, some decisions on initial parameter values and which parameters should be left free, fixed or constrained must be made. In the next subsection, tests are applied to reach the best reconstruction procedure.

6.2.2 Full simulation and reconstruction

As described in Chapter 3, AMIGA detector is being installed in the AMIGA Infill area and a complete Unitary Cell is fully operating since 2015. As such, the following simulations are going to be applied to this specific area and array configuration. Though AMIGA is not yet fully installed, simulations can certainly help towards understanding the final accuracy of the model. In this work, the derived universality signal model including MDs, was tested with 10 EeV showers with a fixed zenith angle of 36°, QGSJetII-04 as the hadronic interaction model, and both proton and iron primaries. QGSJetII-04 is an updated hadronic interaction model. The aim is to compare the Monte Carlo parameters of the simulated showers with the reconstructed ones applying the universality model and combining detectors.

An ideal array with 30 m^2 muon counters composed by three 10 m^2 modules and a 750 m spacing between counters was simulated with the Offline framework [56]. Each muon

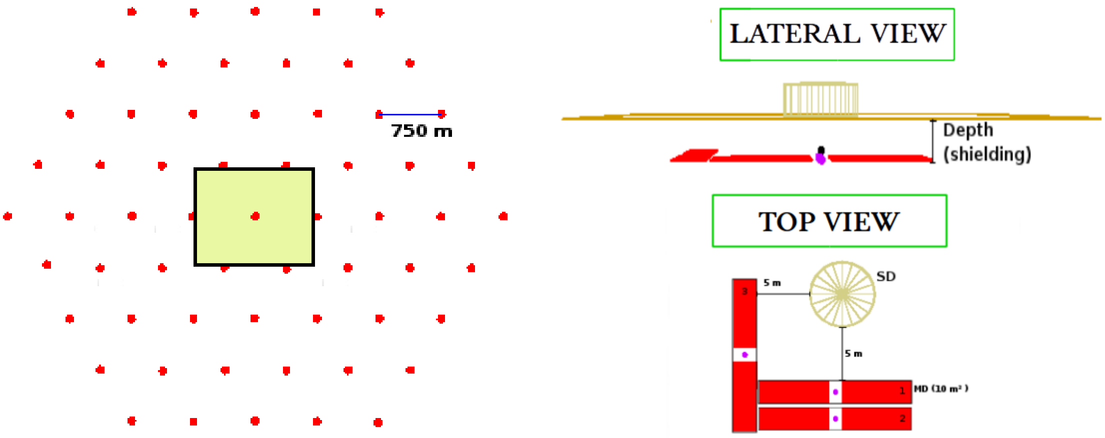

Figure 6.5 [Left] Schematic overview of the selected array for muon-detector response simulation. The coloured area corresponds to the area where the shower cores were allowed to randomly impinge. [Right] Schematic view of simulated detector overview. The red area corresponds to the muon-counter scintillating area.

counter is associated to a surface detector station. Figure 6.5 is an schematic overview of the selected array for muon-detector response simulation.

The showers are forced to impinge in the central coloured area to have all the possible core positions exemplified and also avoid array-border effects. Simulations follow the AMIGA-detectors production design with PMT opto-electronics. Similar results are expected with the current SiPM opto-electronics. The library employed and the simulation parameters are enumerated in detail below.

CORSIKA Showers Library

- Model: QGSJetII-04 and EPOS-LHC. Newest models with larger number of muons.
- Primaries: proton, iron.
- Zenith: $\theta = 36^{\circ}$. Azimuth (ϕ): uniformly distributed.
- log(E): 19.0.
- For each case (Proton - Iron) 120 showers simulated.

$\overline{\text{Off}}\underline{\text{line}}$ Simulation Configuration

- SD @ 40 MHz (SDE).
- AMIGA 30 m^2 @ 2.3 m of depth.
- Three 10 m^2 modules.
- AMIGA PMTs.
- 750 m AMIGA infill.
- Universality reconstruction implemented in $\overline{\text{Off}}\underline{\text{line}}$.
- WCD and MD Signal models.

Once the simulations were performed, different reconstruction procedures were applied to the simulated data to achieve reconstruction performance. As it was shown by the end of previous chapter, the model implies a strong correlation between R_μ and the primary-particle energy which might introduce a bias in the parameters estimation. As a first step in the model testing, the product of both parameters (R_μ and E) are compared to the Monte Carlo primary-particle simulated values. Then, a procedure to separate these two correlated values is proposed. As mentioned before, the information coming from both SD and MD detectors is employed, and the improvement introduced by MD data in the reconstruction is treated in detail. An example of the sequence of modules implemented in this work for the simulation and reconstruction of the cosmic-ray shower is included in Appendix A.

6.3 Reconstructions of the primary-particle muon scale and energy

As a first step, only SD station signals are included in the reconstruction. Since the time model is out of the scope of this work, the $\mathrm{X}_{\mathrm{max}}$ true Monte Carlo value is set as fixed in the reconstruction procedure. The time model may be included afterwards in the reconstruction [10]. $\mathrm{X}_{\mathrm{max}}$ fluctuations are taken into account and tested afterwards in this Chapter.

Figure 6.6 depicts the comparison between simulated primary-particle true parameters, and the relevant reconstructed values obtained by the Universality reconstruction.

Resulted values are biased, even though many stations participate of the reconstruction (high primary-energy event). In this reconstruction stage, the FD energy calibration is not employed. Only Universality model and the SD signal of the stations were included. $\mathrm{X}_{\mathrm{max}}$ is

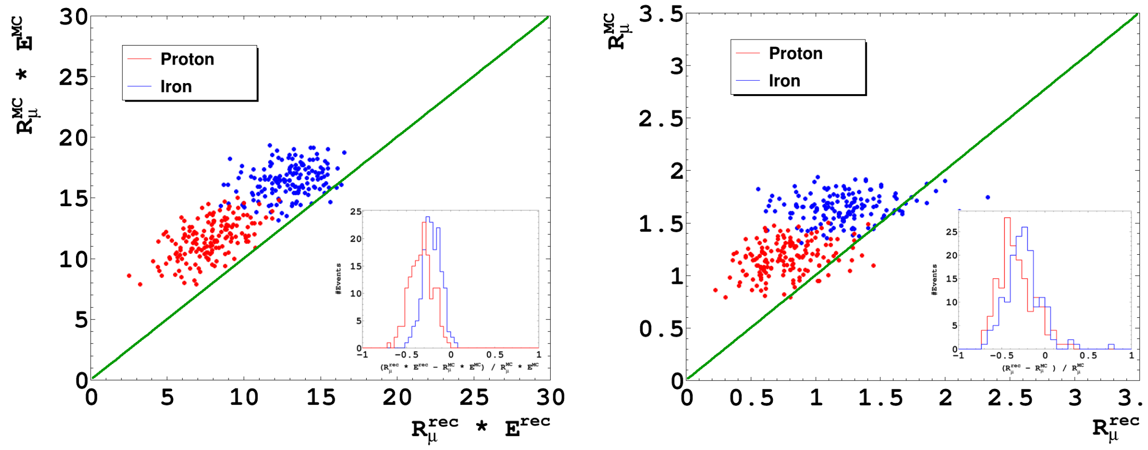

Figure 6.6 Universality reconstruction was applied using only SD signals as input information. X_{max} is set to the true MC value, the other parameters are set free for reconstruction. The high-energy hadronic model employed is QGSJetII-04. Insets evidence the poor resolution and biased parameters obtained in this configuration.

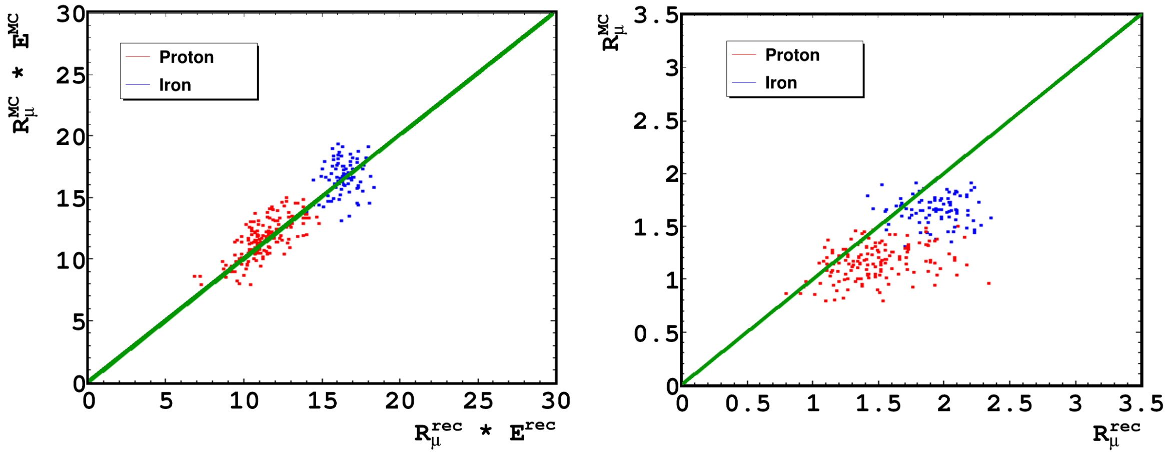

Figure 6.7 Universality reconstruction was applied using both SD and MD signals as input information. X_{max} is set to the true MC value, other parameters are set free for reconstruction. The high energy hadronic model employed is QGSJetII-04.

fixed to the true MC value but the other parameters (geometry, Energy and R_μ) remain free and are reconstructed within the universality model.

After the previous results, the MD signals were included in the reconstruction.

MDs have are capable of detecting the muonic component of the shower with a high resolution thus improving the reconstruction of the primary-particle main parameters. Figure 6.7 shows the comparison between simulated primary-particle true parameters and the reconstructed values obtained by the Universality reconstruction including the MD signals.

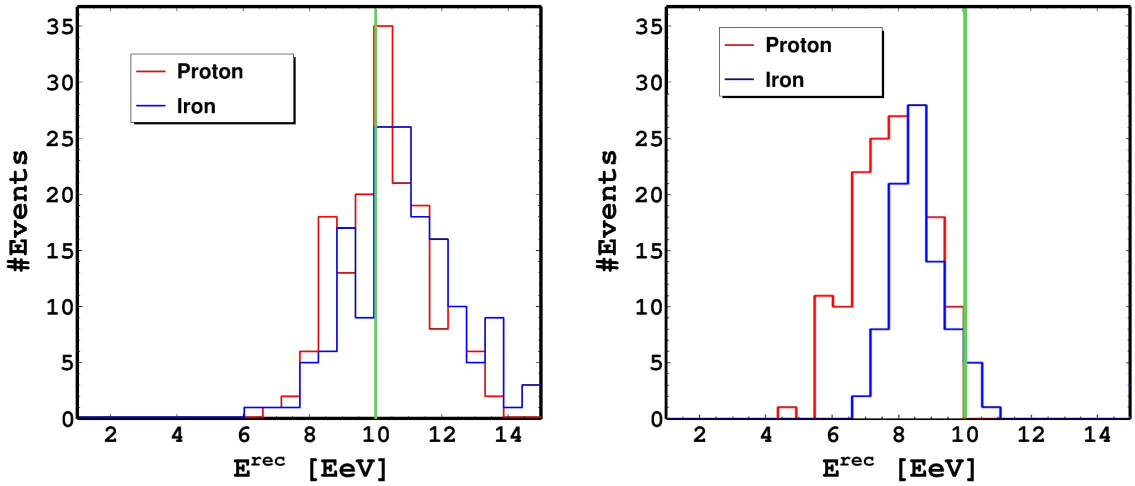

Figure 6.8 [Left] Universality reconstruction was applied using SD signals as input information. X_{max} is set to the true MC value, other parameters are set free for reconstruction. The high energy hadronic model employed is QGSJetII-04. [Right] Universality reconstruction was applied using both SD and MD signals as input information. X_{max} is set to the true MC value, other parameters are set free for reconstruction. The high energy hadronic model employed is QGSJetII-04.

It is seen that product of E and R_μ is now reconstructed unbiased. Furthermore, since the primary energy employed in the simulations is fixed, this product evidences the potentiality of this product as a mass composition estimator. Figure 6.8 evidences that the energy reconstruction is improved as far as fluctuations is concerned but nevertheless remains uncertain and biased.

The question that arises is why if the product is so well reconstructed, the energy and the muonic content are not so well estimated. If we check the universality model.

$$S_0^i(\Delta X, E, R_\mu) = R_\mu E^\gamma f(\Delta X)$$

$$\text{(with } \gamma \sim 1\text{)}$$

So, if we were able to estimate one of both, the other one would be correctly estimated. The procedure pursued was to constrain the energy range to improve the parameters estimation. E was constrained to values within 20% of the initial parameter guess coming from the traditional SD reconstruction. We performed an iterative procedure in order to obtain both MD & SD, constraining the energy to a given range. The results of this procedure are shown in Figure 6.9. The associated merit factor, mean values for both, true Monte Carlo values and reconstructed values are displayed in Table 6.3.

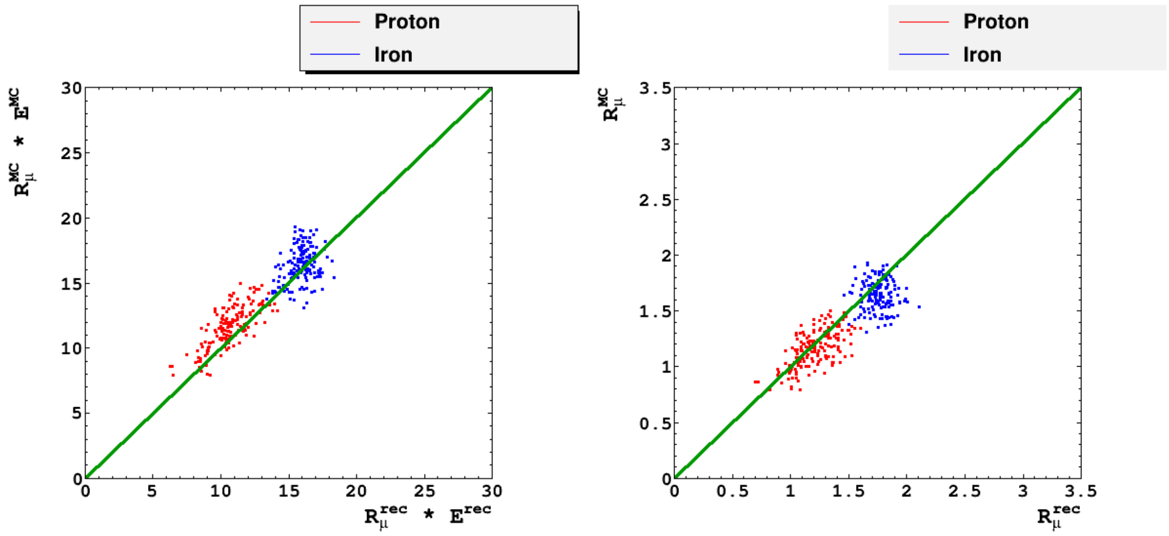

Figure 6.9 Universality reconstruction was applied using both SD and MD signals as input information. X_{max} is set to the true MC value. E was constrained to values within 20% of the initial parameter guess coming from the traditional SD reconstruction. Other parameters are set free for reconstruction. The high energy hadronic model employed is QGSJetII-04.

Primary	$< R_\mu^{MC} >$	$\sigma(R_\mu^{MC})$	$< R_\mu^{Rec} >$	$\sigma(R_\mu^{Rec})$
Proton	1.2	0.15	1.3	0.20
Iron	1.6	0.13	1.8	0.15

	Merit Factor
R_μ^{MC}	2.3
R_μ^{Rec}	2.0

A comparison of energy histograms with signals coming only from SD and form SD combined with MMs is displayed in Figure 6.10.

Primary	$Energy^{MC}$	$< Energy^{Rec} >$	$\sigma(Energy^{Rec})$	BIAS
Proton	10 EeV	8.9 EeV	0.6 EeV	11 %
Iron	10 EeV	9.1 EeV	0.5 EeV	9 %

As mentioned, in the reconstruction procedure the core position, geometry and R_μ were free parameters. E was allowed to change within 20% of the SD reconstructed value. In a similar way, $X_{\max}$ starting value was fixed to the mean value of simulations for the geometry, zenith angle, and hadronic interaction model, it was permitted to fluctuate within 20 g/cm^2.

By using the standard reconstructed energy as a constrained value in the reconstruction, the estimation on the parameters is improved. The energy is estimated as well as the muonic content in a multiparametric analysis that includes both, the MMs signals and the SD ones.

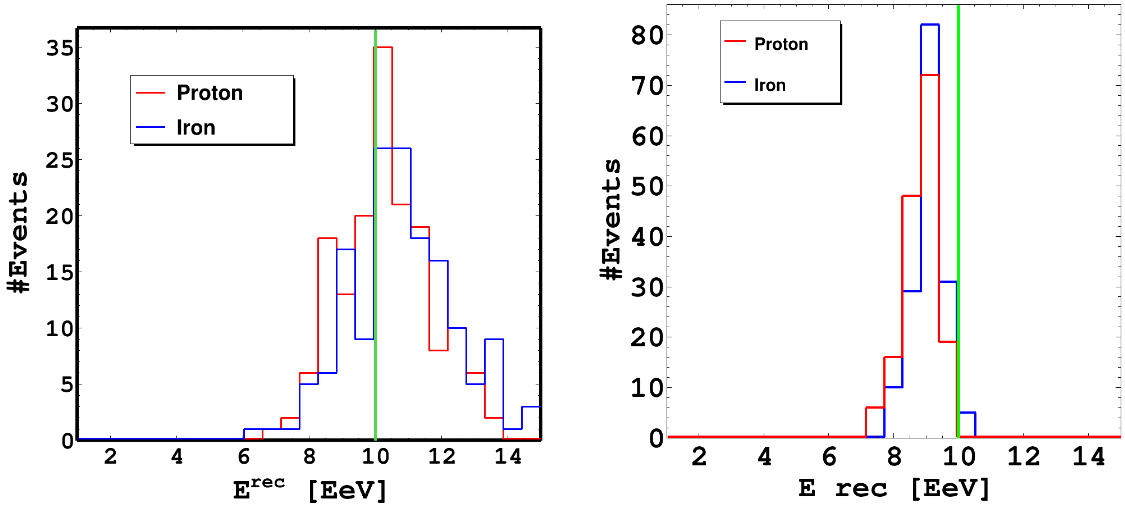

Figure 6.10 [Left] Universality reconstruction was applied using SD signals as input information. X_{max} is set to the true MC value, other parameters are set free for reconstruction. The high energy hadronic model employed is QGSJetII-04. [Right] Universality reconstruction was applied using both SD and MD signals as input information. The energy is constrained around the SD reconstructed value. X_{max} is set to the true MC value, other parameters are set free for reconstruction. The high energy hadronic model employed is QGSJetII-04.

The bias obtained for both parameters is lower than 10%, even in the energy case, where the initial parameters coming from standard reconstruction were biased around 20% from the true value.

These promising results evidences the potentiality of the universality reconstruction combining detectors that measure different shower components. Simulations with different hadronic models and primaries let us trust the results for real measure data, since in that case, we are not sure about hadronic models (at 10 EeV the hadronics models are extrapolations of the accelerators measurements). In the next subsection, the reconstruction procedure described is applied to a real event.

6.3.1 Real event Universality reconstruction

The real event studied in Chapter 4 was reconstructed using this universality reconstruction. The R_μ value obtained was 1.41 ± 0.18 and the energy of $(9.5 \pm 0.6)\ 10^{18}$ eV. The R_μ value is around 10% higher than the mean value corresponding to protons of the hadronic model that predicts the higher muonic content (EPOS-LHC, see [51]), which is also compatible with the FD mass composition analysis developed in Chapter 4 (proton like).

6.4 Conclusions of the chapter

The universality model presented shows that the signal produced by a muon detector can also be described only by a few parameters: E, R_μ and DX (which carries the geometry and $X_{\max}$ of the shower) and $\mathrm{X}_{\max}$.

During this Chapter, different test to evaluate the reliability of the model were explained. First station signals were compared, then the shower parameters were estimated.

An updated $\overline{\mathrm{Off}}\underline{\mathrm{line}}$ implementation was developed to include MMs signals in the universality reconstruction including a new iterative procedure to improve shower parameters estimation by using constrained standard reconstruction parameters as an input to universality reconstruction.

The reconstruction procedure was tested with different hadronic models and primary particles to evidence the robustness of the model.

Preliminary results show that the bias in the reconstructed E and R_μ is $\sim 10\%$. The resolution on R_μ yields large merit factor [1] estimated for mass composition separation of around 2.

A test on a real event that was detected for the energy of interest of the model developed show compatible results with the ones coming from the FD detector.

---

[1] Defined as $(< R_\mu^{Pr} > - < R_\mu^{Fe} >)/\sqrt{(\sigma^2_{R_\mu^{Pr}} + \sigma^2_{R_\mu^{Fe}})}$

Chapter 7

Summary and conclusions

AMIGA (Auger Muons and Infill for the Ground Array) is an upgrade of the Pierre Auger Observatory designed to extend its energy range of detection and to directly measure the muon content of the cosmic ray primary particle showers.

Two main topics were developed during this thesis. The central work was concentrated in developing a new model that can include the MD signals of AMIGA in the universality reconstruction. In parallel, the development of the upgrade of the AMIGA opto-electronics system was complete too.

Regarding the universality reconstruction, a new model that describes a muon detector signal in the core distance range of 100 to 2000 m and the zenith angle range of 0° to 45° was obtained. The combination of two detector types yields a promising improvement to both E and R_μ of the EAS. An independent procedure facilitating the derivation of a new energy scale is of great value and can be directly compared with the energy estimation of the fluorescence detector of the Pierre Auger Observatory. This energy estimation also does not require a calibration curve, and energy can be reconstructed directly with a nearly 100% duty cycle. R_μ is an estimator of particle composition and is also sensitive to hadronic interaction models, which facilitates comparisons of different interaction models with measured data. A good resolution in the estimation of this parameter can aid in understanding differences in the muonic component of different hadronic interaction models and tendencies in the mass composition of measured data. Furthermore, the accurate measurement of R_μ proposed can also aid in the reduction of systematic errors arising from the missing energy estimation (proportional to the muon content) used in the conversion factor needed by fluorescence experiments to convert the measured calorimetric energy into total energy. Within this work, a new method for reconstructing both the energy and R_μ of the EAS was obtained and implemented in $\overline{\text{Off}}\underline{\text{line}}$ [41]. Test with simulations with different hadronic models from the one employed to developed the model show promising results. The implementation in Offline allows also the reconstruction of real data.

Concerning the detector upgrade, previous studies evidence that the design of the Unitary Cell muon counters function successfully within expectations working with an opto-electronics system based on 64 pixel PMT for each module. During the last years a new generation of detectors, replacing the current multi-pixel photomultiplier tube (PMT) with silicon photo sensors (aka. SiPMs), was proposed. The selection of the new device and its front-end electronics was based on the previous PMT design. After several tests the selected SiPM was the S13081-050CS due to its low crosstalk and afterpulsing. The CITIROC ASIC was selected as the electronics front-end. Its fast shaper enables a digital output width of the discriminator similar to the characteristic time width of the light pulses produced by the impinging particles in the detector. The Hamamatsu C11204-01 power supply was chosen for the biasing of the SiPMs.

A method to calibrate the counting system that ensures the performance of the detector was achieved. This method has the advantage of being able to be carried out also in a remote place such as the one where the detectors are deployed. The complete calibration method ensures an uniformity behavior of the 64 channels of each detector, reducing the probability of over-counting particle and increasing detector efficiency. High efficiency results, i.e. 98 % efficiency for the highest tested overvoltage, combined with a low probability of accidental counting ($\sim 2\%$), show a promising performance for this new system. Kathy Turner position has eight modules acquiring calibrated data since December 2016. Preliminary results related to detector performance and twin data analysis are promising. The complete Unitary Cell working with SiPM is planning to be full operating by the end of 2017.

Bibliography

[1] D. Maurel and M. Roth (2014). Update on the composition-enhanced vcv correlations. *Golden Analysis Meeting presentation.*

[2] A. Almela et al. (2013). Design and implementation of an embedded system for particle detectors. *Proceedings of the 33rd International Cosmic Ray Conference, Rio de Janeiro, Brazil*, 1209.

[3] A. Lucero et al. (2015). Analog multiplexer for testing multianode photomultipliers used in amiga project of the pierre auger observatory. *JINST 10*, page T09004.

[4] Abraham et al. (The Pierre Auger Collaboration) (2008). Observation of the suppression of the flux of cosmic rays above 4×10^19 eV. *Physical review letters*, 101(6):1–7.

[5] A.D. Supanitsky, A. Etchegoyen, G. Medina-Tanco, I. Allekotte, M.G. Berisso and M.C. Medina (2008). Underground muon counters as a tool for composition analyses. *Astropart. Phys. 29*, page 461.

[6] Apel et al, W. (2011). Kneelike structure in the spectrum of the heavy component of cosmic rays observed with kascade-grande. *Phys. Rev. Lett.*, 107:171104.

[7] Apel et al, W. (2013). Kascade-grande measurements of energy spectra for elemental groups of cosmic rays. *Astroparticle Physics*, 47:54–66.

[8] Auger, Pierre and Ehrenfest, P. and Maze, R. and Daudin, J. and Robley, A. Freon (1939). Extensive cosmic ray showers. *Rev.Mod.Phys.*, 11:288–291.

[9] Ave et al., M. (2017a). A generalized description of the signal in extensive air shower detectors and its applications. *Astroparticle Physics*, 87:29–39.

[10] Ave et al., M. (2017b). A generalized description of the time dependent signals in extensive air shower detectors and its applications. *Astroparticle Physics*, 88:46–59.

[11] B. Revenu for the Pierre Auger Collaboration (2011). Autonomous detection and analysis of radio emission from air showers at the pierre auger observatory. *Proceedings of the 32nd International Cosmic Ray Conference, Beijing, China*, page 17.

[12] B. Wundheiler et al. (2012). Amiga muon data structure inside cdas. *Pierre Auger Internal Note, GAP-2012-086*, 2012-086.

[13] D. Gora et al. (2006). Universal lateral distribution of energy deposit in air showers and its application to shower reconstruction. *Astroparticle Physics*, 24:484–494.

[14] D. Ivanov et al. (Telescope Array Collaboration) (2015). TA Spectrum Summary. *Proceedings of the 34th International Cosmic Ray Conference, La Hague, The Netherlands*, 349.

[15] D. Ravignani (2013). Observación del espectro de energia de rayos cosmicos con el infill del observatorio pierre auger. *PhD d. Ravignani thesis.*

[16] D. Ravignani and A.D. Supanitsky (2015). A new method for reconstructing the muon lateral distribution with an array of segmented counters. *Astropart. Phys. 65*, 1.

[17] F. D. Kahn, I. Lerche (1966). Radiation from cosmic ray air showers. *Proceedings of the Royal Society of London A: Mathematical, Physical and Engineering Sciences 289*, page 206.

[18] F. Nerling et al. (2006). Universality of electron distributions in high-energy air showers - description of cherenkov light production. *Astroparticle Physics*, 24:421–437.

[19] F. Sánchez et al. (2012). First showers seen by the AMIGA Muon Detector. *Pierre Auger Internal Note, GAP-2012-120.*

[20] F. Sánchez et al. (2016). Efficiency studies for the prototype AMIGA detectors equipped with multi-anode PMTs. *Pierre Auger Internal Note, GAP-2016-051.*

[21] F. Schmidt, M. Ave, L. Cazon and A. Chou (2008). A model-independent method of determining energy scale and muon number in cosmic ray surface detectors. *Astroparticle Phyics 29*, page 355.

[22] F. Suarez for The Pierre Auger Collaboration (2013). The amiga muon detectors of the pierre auger observatory: overview and status. *Proceedings of the 33rd International Cosmic Ray Conference, Rio de Janeiro, Brazil*, 712.

[23] G. Askaryan (1962). Excess negative charge of an electron-photon shower and its coherent radio emission. *Soviet Physics JETP 14*, page 441.

[24] G. Battistoni et al. (2007). The fluka code: description and benchmarking. *AIP Conference Proceeding*, 896:31–49.

[25] Greisen, Kenneth (1966). End to the cosmic ray spectrum? *Phys.Rev.Lett.*, 16:748–750.

[26] H.-J. Mathes (2011). The heat telescopes of the pierre auger observatory. status and first data. *Proceedings of the 32nd International Cosmic Ray Conference (ICRC), Beijing, China.*

[27] Hamamatsu Photonics K.K. (2015). Power supply for mppc. *Datasheet.*

[28] Hamamatsu Photonics K.K.P. (2015a). MPPC multi-pixel photon counter, s12571-25, -50, -100cp specification datasheet. *Datasheet.*

[29] Hamamatsu Photonics K.K.P. (2015b). MPPC multi-pixel photon counter, s12572-25, -50, -100cp specification datasheet. *Datasheet.*

[30] Hamamatsu Photonics K.K.P. (2015c). MPPC multi-pixel photon counter, s13081-050cs, s13081-050pe specification datasheet. *Datasheet.*

[31] Heck et al., D. (1998). Corsika: A monte carlo code to simulate extensive air showers. *Forschungszentrum Karlsruhe report FZKA*, 6019.

[32] I. Allekotte, et al. (2008). The surface detector system of the pierre auger observatory. *NIM A 586*, page 409.

[33] I. Sidelnik et al. (2012). Deployment of $10m^2$ muon counter modules of the amiga pre-unitary cell. *Pierre Auger Internal Note, GAP-2012-079.*

[34] J. Linsley (1963). Evidence for a primary cosmic-ray particle with energy 10e20 ev. *Phys. Rev. Lett.*, 10:146.

[35] John L. Kelley for the Pierre Auger Collaboration (2011). AERA: the auger engineering radio array. *Proceedings of the 32nd International Cosmic Ray Conference, Beijing, China*, page 13.

[36] KASKADE Grande Collaboration (2005). Recent Results. *Proc. 29th ICRC, Pune, India, 2005.*

[37] M. Ave (2012). Ground signal parameterization for water cherenkov and scintillator detectors and performance of ground arrays that combine both techniques. *Pierre Auger Internal Note, GAP-2012-141.*

[38] M. Ave, R. Engel, J. Gonzalez, D. Heck, T. Pierog, M. Roth (2011). Extensive air shower universality of ground particle distributions. *Proceedings of the 32rd International Cosmic Ray Conference, Beijing, China.*

[39] M. D. Healy et al. (2006). Applying the constant intensity cut to determine composition, energy, and muon richness. *Pierre Auger Internal Note, GAP-2006–020.*

[40] M. Giller te al. (2005). Similarity of extensive air showers with respect to the shower age. *Journal of Physics G Nuclear Physics*, 31:947–958.

[41] M. Josebachuili et al. (2015). Improving the universality reconstruction with independent measurements by water-cherenkov detectors and muon counters. *Proceedings of the 34th International Cosmic Ray Conference, La Hague, The Netherlands*, 409.

[42] M. Nagano, A. A. Watson (2000). Observations and implications of the ultrahigh-energy cosmic rays. *Reviews of Modern Physics 72*, page 689.

[43] M. Platino et al. (2011). AMIGA at the auger observatory: the scintillator module testing system. *JINST 6.*

[44] M. Unger for the Telescope Array and the Pierre Auger Observatory Collaborations joint contributions (2015). Report of the working group on the composition of ultra-high energy cosmic rays. *Proceedings of the 34th International Cosmic Ray Conference, La Hague, The Netherlands.*

[45] Nagano, M. and Watson, A. A. (2000). Observations and implications of the ultrahigh-energy cosmic rays. *Rev. Mod. Phys.*, 72:689–732.

[46] Omega Micro CNRS-IN2P3-Ecole Polytechnique (2014). CITIROC front-end chip. *Datasheet.*

[47] Ostapchenko, S. (2011). Monte Carlo treatment of hadronic interactions in enhanced Pomeron scheme: QGSJET-II model. *Physical Review D 83, 2011, 014018.*

[48] P. Billoir (2004). Indirect measurement of xmax with the surface detector. *Pierre Auger Internal Note, GAP-2004–010.*

[49] P. Billoir et al. (2007). Evaluation of the primary energy of uhe photon-induced atmospheric showers from ground array measurements. *ArXiv Astrophysics e-prints*, (0701583).

[50] Pierog, T. (2013). LHC results and High Energy Cosmic Ray Interaction Models. *Journal of physics: Conference Series 409, 2013, 012008.*

[51] Pierog, T. and Heck, D. (2013). Air shower simulation with new interaction models in CORSIKA. *Proc. 33nd ICRC, Rio de Janeiro, Brasil.*

[52] R. A. Millikan, G. Horvey Cameron (1926). High frequency rays of cosmic origin iii. measurements in snow-fed lakes at high altitudes. *Physical Review 5*, 28:851.

[53] R. Abbasi et al. (High Resolution Fly's Eye Collaboration) (2008). First Observation of the Greisen-Zatsepin-Kuzmin Suppression. *Physical review letters*, 100:101101.

[54] R. Conceicão, M. Pimenta, and R. R. Prado (2014). Is it possible to discriminate mass composition scenario from new physics? *Pierre Auger Internal Note, GAP-2014-069.*

[55] Revised by J.J. Beatty, J. Matthews, and S.P. Wakely (2015). Cosmic rays. *Particle Data Group Report*, 28.

[56] S. Argiro et al. (2007). The offline software framework of the pierre auger observatory. *Nucl. Instrum. Meth. A*, 580:1485–1496.

[57] S. Buitink, et al. (2013). Shower xmax determination based on lofar radio. *Proceedings of the 33rd International Cosmic Ray Conference, Rio de Janeiro, Brazil.*

[58] S. Ostapchenko (2011). Monte carlo treatment of hadronic interactions in enhanced pomeron scheme: I. qgsjet-ii model. *Physical review*, D83(014018).

[59] S. Piatek, Hamamatsu Corporation & New Jersey Institute of Technology (2014). Physics and Operation of an MPPC.

[60] Suarez for the Pierre Auger Collaboration, F. (2013). The AMIGA muon detectors of the Pierre Auger Observatory: overview and status. *Proc. 33nd ICRC, Rio de Janeiro, Brasil, arXiv:1307.5059.*

[61] T. Karg, for the IceCube Collaboration, J. Alvarez-Muñiz, D. Kuempel, M. Settimo, for the Pierre Auger Collaboration, G. Rubtsov, S. Troitsky, for the Telescope Array Collaboration (2016). Report from the multi-messenger working group at uhecr-2014 conference. *JPS Conf. Proc. 9, 010021.*

[62] T. Pierog (2013). LHC results and high energy cosmic ray interaction models. *23rd European Cosmic Ray Symposium*, 409:012008.

[63] The pierre Auger Colaboration (2010). Measurement of the energy spectrum of cosmic rays above 10^{18} ev using the pierre auger observatory. *Physics Letters B*, 685:239–246.

[64] The Pierre Auger Colaboration (2014). A search for point sources of eev photons. *The Astrophysical Journal*, 789:160.

[65] The Pierre Auger Colaboration (2016). Testing hadronic interactions at ultrahigh energies with air showers measured by the pierre auger observatory. *Physical review letters*, 117:192001.

[66] The Pierre Auger Collaboration (2007). Test of hadronic interaction models with data from the pierre auger observatory. *Proceedings of the 30th International Cosmic Ray Conference (ICRC), Merida, Mexico*.

[67] The Pierre Auger Collaboration (2008). The fluorescence detector of the pierre auger observatory. *NIM A 620*, page 227.

[68] The Pierre Auger Collaboration (2010). Trigger and aperture of the surface detector array of the pierre auger observatory. *NIM A 613*, page 29.

[69] The Pierre Auger Collaboration (2012). Results of a self-triggered prototype system for radio-detection of extensive air showers at the pierre auger observatory. *Journal of Instrumentation 7*, page P11023.

[70] The Pierre Auger Collaboration (2014). Depth of maximum of air-shower profiles at the pierre auger observatory: Composition implications. *High Energy Astrophysical Phenomena (astro-ph.HE)*.

[71] The Pierre Auger Collaboration (2015). The pierre auger observatory: Contributions to the 34th international cosmic ray conference. *Proceedings of the 34th International Cosmic Ray Conference, La Hague, The Netherlands*.

[72] The Pierre Auger Collaboration (2016a). Prototype muon detectors for the amiga component of the pierre auger observatory. *JINST 11*, page P02012.

[73] The Pierre Auger Collaboration (2016b). The pierre auger observatory upgrade "auger-prime" preliminary design report. *Arxiv*.

[74] The Pierre Auger Collaboration (2017). Muon counting using silicon photomultipliers in the AMIGA detector of the Pierre Auger Observatory. *JINST 12*, page P03002.

[75] The Pierre Auger Collabration (2016). The pierre auger cosmic ray observatory. *NIM A 798*, page 172.

[76] Ulrich et all, H. (2004). Energy spectrum and elemental composition of cosmic rays in the pev region. *The European Physical Journal C - Particles and Fields*, 33(1):944–946.

[77] V. F. Hess (1912). Über beobachtungen der durchdringenden strahlung bei sieben freiballonfahrt. *Phys. Zeitschr. 13*, page 1084.

[78] Zatsepin, Z. and Kuz'min V. (1966). Upper Limit of the Spectrum of Cosmic Rays. *Zh. Eksp. Teor. Fiz. Pis'ma Red*, 4:114–117.

Appendix A

MD signal model and its Offline implementation

A.1 MD signal model parametrization

As it was described in Chapter 5, the signal model implemented to described each detector signal can be described as follows.

$$S(E,\mathrm{X_{max}},\mathrm{R}_{\mu},\theta,\rho_{\mathrm{air}})|_{\mathrm{r},\psi}=\sum_{\mathrm{i}=1}^{4}\mathrm{S_0^i}(\mathrm{DX},\mathrm{E})\cdot\mathrm{f^i_{mod}}(\mathrm{r},\theta,\psi)\cdot\mathrm{f^i_{conv}}(\mathrm{r},\mathrm{DX},\theta,\psi)\cdot\mathrm{f^i_{atm}}(\mathrm{r},\rho_{\mathrm{air}})\cdot\mathrm{f^i_{R_{\mu},fluct}} \tag{A.1}$$

where

- $S_0^i \cdot f^i_{\mathrm{mod}}$ is the signal deposited by an air shower simulated in an ideal detector, i. e. a detector with the same projected area regardless the impinging particle direction and considering a detector response signal equivalent to a vertical particle.

- DX carries the dependence on X_{max} and geometry and will be described later in the text.

- f^i_{conv} is the conversion factor to a real detector. This correction considered changes in the detector signal due to the change in the projected area and detector response when particles impinges the detector with a different angle from the normal one.

- f^i_{atm} evidences changes in the signal due to seasonal changes in the atmospheric profiles.

- $f^i_{R_{\mu},\mathrm{fluct}}$ is a factor that takes into account fluctuations in the shower muon production with an explicit dependence with air shower components.

For the particular case of the MD, only the muonic component is considered, since other components are shield by the ground above the underground detector, contamination is expected to be less than 5 %.

The ideal signal component (S_0^i) detected by the muon detector or by the water-Cherenkov detector is described with a general function (Already mentioned in Chapter 5 and shown in Equation A.2 again). It was found that both detectors are parametrized by this function with only different parameters values.

$$S_0^i(DX,E) = S_{\mathrm{ref}} \left(\frac{E}{10^{19}\mathrm{eV}}\right)^{\gamma} \left(\frac{DX - DX_0}{DX_{\mathrm{ref}} - DX_0}\right)^{\left(\frac{DX_{\mathrm{max}} - DX_0}{\lambda(E)}\right)} exp\left(\frac{DX_{\mathrm{ref}} - DX}{\lambda(E)}\right) \tag{A.2}$$

The parametrization of the MD signal for an ideal detector, in an ideal atmosphere and without any asymmetry effects, is obtained from Equation A.2.

The special case of the muonic component (including the dependence on R_μ) is shown in Equation A.3.

$$S_0^{\mu}(DX,E,R_\mu) = R_\mu \left(\frac{E}{10^{19}eV}\right)^{\gamma} S_{ref} \left(\frac{DX - DX_0}{DX_{ref} - DX_0}\right)^{\left(\frac{DX_{max} - DX_0}{\lambda}\right)} exp\left(\frac{DX_{ref} - DX}{\lambda}\right) \tag{A.3}$$

In the case of the muon detector, some assumptions were applied: $\lambda(E) = \lambda$, $DX_0 = 250$ g/cm^2, and $DX_{ref} = 600$ g/cm^2.

In the signal model procedure, each parameter is obtained as a function of the radial distance to the core. In the following, the functional relations between variables selected for this work are described.

A.1.1 Parameters

Four parameters are parametrized as a function of radial distance to obtain the total signal of each detector. These parameters are: S_{ref}, DX_{max}, γ and λ and their expression are listed in Equation A.4.

$$\begin{aligned}
S_{ref} &= A_{Sref} * \left(\frac{x}{1000}\right)^{B_{Sref}} * \left(\frac{D_{Sref}+x}{D_{Sref}+1000}\right)^{-C_{Sref}}, \\
\gamma &= A_{\gamma} + B_{\gamma} * \exp\left(\frac{-x}{500}\right), \\
\lambda &= A_{\lambda} + B_{\lambda} * \exp\left(\frac{x * C_{\lambda}}{1000}\right), \\
DX_{max} &= A_{DXmax} + B_{DXmax} * \left(\frac{x}{1000}\right)^{C_{DXmax}}.
\end{aligned} \tag{A.4}$$

These results were included in Offline complementary modules to reconstruct the main parameters of the shower, by knowing the signals in the detectors.

A.2 Offline implementation

Offline is the official code employed by the Pierre Auger Collaboration. The module developed to implement Universality reconstruction within Auger data, was updated to include MD data in the reconstruction procedure.

A.2.1 Module Sequence

The following Module Sequence was applied in Offline in order to get the parameters of the standard reconstruction and the new implemented one.

The Offline Module implemented and modified was the **UniversalityFitter** to include the MD data in the reconstruction and also to allow an iterative reconstruction including initial parameters coming from the standard Pierre Auger Collaboration reconstruction.

```
<!-- A sequence for a hybrid (SD+MD+FD) reconstruction -->
<!-- Universality reconstruction is included -->

<sequenceFile xmlns:xsi="http://www.w3.org/2001/XMLSchema-instance"
              xsi:noNamespaceSchemaLocation='@SCHEMALOCATION@/
   ModuleSequence.xsd'>

  <enableTiming/>
  <moduleControl>
    <loop numTimes="unbounded" pushEventToStack="yes">


  <module> EventFileReaderOG </module>
```

```

 <module> EventCheckerOG </module>
 <module> SdPMTQualityCheckerKG </module>
 <module> TriggerTimeCorrection </module>
 <module> SdCalibratorOG </module>
 <module> SdStationPositionCorrection </module>
 <module> SdBadStationRejectorKG </module>
 <module> SdSignalRecoveryKLT </module>
 <module> SdEventSelectorOG </module>
 <module> SdPlaneFitOG </module>
 <module> LDFFinderKG </module>
 <module> SdEventPosteriorSelectorOG </module>

 <!-- Md Recostruction: count muons (irrespective of RecShower) -->
 <try>
    <module> MdMuonCounterAG              </module>
    <module> MdModuleRejectorAG           </module>
    <module> MdEventSelectorAG            </module>
    <module> MdLDFFinderAG                </module>
 </try>

         <!-- Hybrid reconstruction -->
 <try>
           <module> FdCalibratorOG             </module>
           <module> FdEyeMergerKG         </module>
           <module> FdPulseFinderOG            </module>
           <module> PixelSelectorOG            </module>
           <module> FdSDPFinderOG              </module>
           <module> FdAxisFinderOG             </module>
           <module> HybridGeometryFinderOG     </module>
           <module> FdApertureLightKG          </module>
           <module> FdProfileReconstructorKG   </module>
           <module> FdEnergyDepositFinderKG    </module>
 </try>

 <module> UniversalityFitter </module>

 <module> RecDataWriterNG </module>

   </loop>

 </moduleControl>

</sequenceFile>
```

The **UniversalityFitter** Module is the module updated to read signals coming from MMs. In that module only the MMs signals are read and included in the analysis, as well as with the other detectors. There is a configuration flag that indicates if AMIGA signals must be included in the reconstruction.

A complementary function was included to deal with the reconstruction. **UnivRecNS** that manages the details on the reconstruction procedure. This function was updated to include MMs signals in the multiparametric reconstruction and to include the possibility of performing th reconstruction in an iterative mode, including the standard reconstruction parameters as constrained inputs. Also some complementary files were modified (as **UnivParamNS** for example) to include all the new AMIGA parametrization.